Doctorate Dissertation
博士論文

Optical physics

with

topological lightwaves

(トポロジカル光波による光物性)

A Dissertation Submitted for Degree of Doctor of Philosophy
December 2018
平成30年12月博士（理学）申請

Department of Physics, Graduate School of Science,
The University of Tokyo
東京大学理学系研究科物理学専攻

Hiroyuki Fujita
藤田 浩之

Abstract

Optical physics is a study of light-matter interaction. In the past decades, controlling electric and magnetic properties of matter by laser beams has been actively explored in the broad region of condensed-matter physics, including spintronics and magneto-optics, supported by the development of laser technologies. In this thesis, we discuss how optical physics and the emerging field of ultrafast magnetism can be even more promising with the help of the new types of lights, topological lightwaves, which possess topologically nontrivial spatial profiles.

We take optical vortices, lightwaves carrying non-vanishing orbital angular momentum, and cylindrical vector beams, lasers with unconventional vortical polarization profiles, and theoretically discuss how they could be useful for optical physics. We demonstrate that (i) optical vortices can propel ultrafast magnetism through their orbital angular momentum and the peculiar spatial profile, (ii) the unique focusing property and spatial profile of cylindrical vector beams enable us to see and control matters in a way difficult or totally impossible before, thus having substantial impacts on condensed-matter physics and chemistry/biology.

We establish a connection between singular optics, a study of topological lightwaves, and optical physics. The new research field of *singular light optics* will extend our ability to study and control electromagnetic properties of matters.

Contents

Acknowledgement

I thank my PhD supervisor and a collaborator, Prof. Masaki Oshikawa and our group secretary Mrs. Tsuji for supporting me during the PhD course. I thank my collaborators, Masahiro Sato, Yasuhiro Tada, Shunsuke Furukawa, Sho Sugiura, Masahiro Nozaki, Yuya O. Nakagawa, Masataka Watanabe, Yuto Ashida, Masahiko G. Yamada, and again Masaki Oshikawa. I also thank (former) members and visitors of our group for the fruitful discussions with them. I particularly thank Masahiro Sato as the primary collaborator of this project.

I thank Japan Society for the Promotion of Science for supporting me financially through Advanced Leading Graduate Course for Photon Science (ALPS) and Research Fellowship for Young Scientists.

Last, but not least, I would like to thank my parents and sister for their patience and encouragement.

List of abbreviations

OV	optical vortex
CVB	cylindrical vector beam
LG	Laguerre-Gaussian
OAM	orbital angular momentum
FM	ferromagnet
AFM	antiferromagnet
DM	Dzyaloshinsky-Moriya
LLG	Landau-Lifshitz-Gilbert
ME	magneto-electric
SOC	spin orbit coupling
ESR	electron spin resonance
EDSR	electron dipole spin resonance
EPR	electron paramagnetic resonance

Chapter 1

Introduction

In this Introduction, we present the background of our study. We review the two growing fields: optical physics and singular (or structured light) optics. We first look back on the rapid advances of the laser technologies in the past decades such as the realization of ultrashort laser pulses and strong terahertz (THz) light sources. We then discuss how they have contributed to deepening our understanding of static and dynamical properties of matter. We review the developing field of the laser manipulation of magnetism, namely ultrafast magnetism and why it is important both from scientific and industrial viewpoints. We then introduce the notion of the topological lightwaves which plays the central role in our study. We explain the basic properties of those lasers comparing with those of conventional Gaussian lasers and discuss how they could be potentially exploited for optical physics.

1.1 Ultrafast physics with lasers

In this section, we review the recent developments of experimental and theoretical optical physics, in particular, in the growing field of ultrafast magnetism; a study of laser-driven magnets.

1.1.1 Lasers in modern physics

The history of the laser goes back to the study of A. Einstein in 1917 [1] on the quantum theory of radiation and stimulated emission. Using the stimulated emission, we can coherently amplify the incident lightwave and turn it into lasers. Today, lasers have become indispensable tools in modern society, and those in the wide range of frequencies (from infrared to X-ray) are utilized for various purposes, such as sensors, information processing, ablation, welding, structural analyses, surgeries, and so on.

Lasers also keep their unique position in scientific researches. Using lasers, we can characterize the structural and electrical properties of molecules and solids accurately. The obtained knowledge has been the baseline of modern physics, chemistry, and life-science. In physics, our knowledge of the atomic and molecular energy structures allows us to control the properties of atoms and molecules in the single particle level [2, 3]. The laser-trapped gases or ions nowadays offer unique playgrounds to build quantum simulators, with which we could study the physics of strongly correlated many-body systems [4], the origin of thermodynamics [5], and even black-holes [6].

Lasers are becoming even more important due to the rapid developments of the laser-related technologies in the past decades. The new lights shine new lights on nature, and the realization of intense, ultra-short light pulses [7] now allows us to measure the light-atom (light-matter) interactions in a way impossible before. The electric-field intensity of lasers now exceeds the intra-molecular field and the pulse width reaches to the order of ten attoseconds. The former results in the strong ionization of molecules and results in new ultrafast phenomena like Coulomb explosion of highly-excited molecules [8]. The attosecond temporal resolution shines a light on the *intra-molecular* dynamics of electrons [9, 10][1].

In the context of condensed-matter physics, the development of the intense THz lasers is also important [11, 12]. Since THz is at the energy scale of various collective physics in solid-state materials, such as phonons,

[1]The period of the electron circulation around the nucleus in the Bohr model is of the order of 100 attoseconds.

magnons, and superconductivity, THz lasers gather attention in the context of materials manipulations. Indeed, various interesting experiments like the ultrafast THz control of antiferromagnetism [13, 14, 15, 16] and the THz resonant excitation of Higgs modes in superconductors were reported [17, 18]. The intense ultra-short pulses are again important for the developments as they provide a way of generating intense THz pulses through nonlinear optical effects.

Those experimental developments casted questions on the properties of highly nonequilibrium states of matters which go beyond the applicability of conventional linear-response treatments [19]. Since the faithful treatment of the time-evolution of many-body systems is possible only for limited cases such as classical spins only with short-ranged interactions, new theoretical frameworks have been desired. Examples of such frameworks include the Floquet-theory for periodically driven systems [20, 21, 22] and time-dependent density-matrix renormalization-group (tDMRG) [23]. In particular, the approaches based on the Floquet theory have been succeeding in describing the driven system quite well. In the past few years, a new phase of matter called the *Floquet topological phase [24, 25]* has been established.

1.1.2 Ultrafast magnetism

Among various subjects in optical physics, in this thesis, we mainly focus on the interplay of lightwaves and magnetic properties of solid-state materials. Here we explain why magnetism and its optical control is a vital subject.

The study of interactions between magnetic materials and lightwaves has a long history. Various magneto-optical phenomena, such as optical Kerr effect, Faraday effect, and the Cotton-Mouton effect, have been known and utilized for materials characterizations [26]. Nevertheless, the primary usage of lasers in condensed-matter physics before 90' was for spectroscopies of electronic properties of matter.

The change in the paradigm of optical physics was brought about by the paper *"Ultrafast Spin Dynamics in Ferromagnetic Nickel"* [27]. In their epoch-making experiment in 1996, Beaurepaire et al. demonstrated the ultrafast demagnetization of ferromagnetic nickel. The possibility of controlling and observing dynamical properties of magnets using laser pulses turned the eyes of condensed-matter physicists to rich physics of light-matter interactions, in particular, to light-magnet interactions.

The study of light-magnet interactions, namely ultrafast magnetism [28] (or ultrafast spintronics) is getting important from the industrial and envi-

ronmental viewpoints. The modern semiconductor-based information processing consumes a vast amount of energy. For example, the dynamic random-access memory (DRAM) is a major source of the consumption because DRAMs are essentially an array of capacitors, and they require continual refreshing of the electric charge to avoid errors.

A possible improvement in the energy consumption will be achieved by replacing DRAMs by non-volatile memories which can keep the recorded information without energy-consuming operations like refreshing. This is precisely what the spintronics is pursuing. Using magnetic materials for information storage is advantageous in its non-volatility and the high-recording density. The developing magnetic random-access memory (MRAM) utilizes the non-volatile nature of a spin texture in magnets to suppress the energy consumption.

Regarding their operating speed, however, MRAMs today do not compete with DRAMs. The ultrafast magnetization dynamics indued with laser beams could be the key to overcome this problem. Writing and reading of magnetically encoded information using lasers would be a strong candidate of the replacement of semiconductor-based memories. Stimulated by Beaurepaire et al. [27] there appeared a number of researches on the all-optical switching of magnetic orders, namely the magnetization reversal induced with laser pulses [29, 30, 31]. Although the background mechanism of the ultrafast change of magnetizations under laser pulses is still under debate, the phenomenon itself has been well established, and the study of the laser-based magnetic memory is ongoing.

Studies of light-matter interaction in the past decades also revealed the other rich physics of laser-driven magnets. In addition to the traditional semiclassical transport theories, nowadays the Floquet theory of driven matters [20, 21, 22] offers a powerful way of theoretically studying the laser-driven matters. The fruits of the recent theoretical works like laser-induced magnetization [32, 33] and optically induced spin currents [34, 35, 36] provide milestones of ultrafast magnetism.

The importance of intense THz lasers is worth mentioning again. Firstly, from the viewpoint of the Floquet theory (which is essentially a high-frequency expansion), they are the most natural frequency to work with. Secondly, they expand the range of ultrafast magnetism to novel targets like multiferroics magnets [36, 37, 38, 39] and antiferromagnets [13, 14, 15, 16]. Because these materials often have their characteristic energy scale in the (sub-) THz region, intense THz lasers and coherent control of these magnets with them are propelling the discovery of new optical phenomena.

1.1.3 A new direction of optical physics

As we have seen, optical physics, particularly ultrafast magnetism, in the past decades has been supported by the intense ultra-short pulse lasers. What comes in the next ten or twenty years? A possible research direction is to apply established methods to new materials while keeping the light sources improved. Ultrafast magnetism has been, so far, mostly focused on ferromagnetic materials, but we could extend that to antiferromagnets, ferrimagnets, or other exotic magnetic materials. There would also be plenty rooms for topological things to play roles. Optical control of topological insulators [24], topological superconductors [40], and spin liquids [41] may lead to novel applications.

This naive approach seems to be reasonable and would indeed work. However, if we recall that all the past developments were brought about by new light sources in the first place, it would be natural to pay more attention to lasers themselves. Unfortunately, today we encounter a large separation between optics and optical physics, presumably because of the "too much" success in optical physics made with conventional laser techniques. In the past twenty years, researches in optics realized a variety of novel lightwaves. However, optical physics community has been happy with conventional lasers and those "structured" lasers have been virtually ignored by the community. In this thesis, we would like to build a missing bridge between optical physics and optics of such novel lasers, pushing optical physics foward. In particular, we consider so-called topological lightwaves and discuss how their unique properties provide novel tools for optical physics.

1.2 Topological lightwaves

In the previous section, we reviewed the developments in optical physics, especially ultrafast magnetism. In this section, we introduce the notion of topological lightwaves, which play the central role in this thesis. In the first subsection, we introduce the notion of optical vortex, a lightwave carrying orbital angular momentum. In the second subsection, we review cylindrical vector beam, a laser with vortical polarization.

1.2.1 Optical vortices

An optical vortex (OV) is a structured lightwave characterized by its topologically nontrivial phase profile. OVs have spiral-shaped phase structure [42] originating from their non-vanishing orbital angular momentum (OAM). In this subsection, we give a brief review of OVs: their profiles, mathematical descriptions, the way of their generation, and some applications.

The study of OVs was initiated by the paper *"Orbital angular momentum of light and the transformation of Laguerre-Gaussian laser modes"* by Allen et al. in 1992 published in Physical Review A [43]. There, the light carrying orbital, not spin, angular momentum was established [44, 45]. OVs are quite often confused with circularly polarized lasers, but these two are different since the angular momentum carried by circularly polarized lasers has its origin in the photon's spin angular momentum. An intuitive description of the OAM of OVs is that it refers to the circulating motion of photons around their propagation axis (below we take that in the z direction).

When electromagnetic fields of a laser have an azimuthal angular dependence of the form $\exp(im\phi)$, such a laser becomes an eigenstate of the angular momentum operator $L_z = -i\hbar\partial/\partial\phi$ with the angular momentum $\hbar m$. This twist in the phase structure of the propagating beams characterizes the OVs. The twisted phase structure forces the beams to have a *topological singularity* along the propagation axis, a line with vanishing beam intensity[2]. As a result, the spatial profile of the (time-averaged) intensity of OVs becomes ring-shaped.

Let us give a mathematical description of OVs, or the Laguerre-Gaussian (LG) modes, to make contrast with conventional Gaussian beams better. The derivation is simple. The LG modes are derived from the Maxwell

[2]This is similar to the atomic wave function of p, d, f, ... orbitals or the cores of vortices in liquids. Without the singularity, the electromagnetic fields are not single-valued at the center.

equations in a vacuum. If we assume electromagnetic waves with fixed frequency ω, their propagation in a vacuum is governed by the following wave equations directly derived from the Maxwell equations:

$$\left(\Delta + \frac{\omega^2}{c^2}\right) \boldsymbol{E} = 0, \tag{1.1}$$

$$\left(\Delta + \frac{\omega^2}{c^2}\right) \boldsymbol{B} = 0, \tag{1.2}$$

where Δ is the three-dimensional Laplacian and c is the speed of light in a vacuum. These equations are equivalent to Helmholz-type differential equations. Since the wave equation for the electric field $\boldsymbol{E}$ and the magnetic field $\boldsymbol{B}$ takes the same form in a vacuum, below we focus on the electric field part. In the cylindrical coordinate (ρ, ϕ, z), where ρ is the radial coordinate, ϕ the azimuthal angle, and z the coordinate along the cylindrical axis, the three-dimensional Laplacian is written as $\Delta = \frac{\partial^2}{\partial \rho^2} + \frac{1}{\rho}\frac{\partial}{\partial \rho} + \frac{1}{\rho^2}\frac{\partial^2}{\partial \phi^2} + \frac{\partial^2}{\partial z^2}$.

We define the homogeneous polarization vector $\hat{e}$ and write the electric field in the form $\boldsymbol{E} = \hat{e}\psi(\boldsymbol{r})$. Using the wave vector $k = \omega/c$, we write the scalar part of the electric field as $\psi(\boldsymbol{r}) = u(\boldsymbol{r})e^{ikz}$. Then, the wave equation Eq. (1.2) reduces to

$$\left(\Delta_T + 2ik\frac{\partial}{\partial z} + \frac{\partial^2}{\partial z^2}\right) u(\boldsymbol{r}) = 0, \tag{1.3}$$

where $\Delta_T = \frac{\partial^2}{\partial r^2} + \frac{1}{\rho}\frac{\partial}{\partial \rho} + \frac{1}{\rho^2}\frac{\partial^2}{\partial \phi^2}$ is the transverse component of the Laplacian.

Let us employ the paraxial approximation to Eq. (1.3). We consider the case in which the function $u(\boldsymbol{r})$ is a slowly varying one along the z axis, and thus the overall z dependence of the electric field $\boldsymbol{E}(\boldsymbol{r})$ is divided into the fast part captured by e^{ikz} and the rest, slow part in $u(\boldsymbol{r})$. Keeping this assumption in mind, we impose $|\frac{\partial^2 u}{\partial z^2}| \ll |\frac{\partial^2 u}{\partial x^2}|, |\frac{\partial^2 u}{\partial y^2}|$ and $|\frac{\partial^2 u}{\partial z^2}| \ll 2k|\frac{\partial u}{\partial z}|$. Then we can drop the second-order derivative in Eq. (1.3) and have

$$\left(\Delta_T + 2ik\frac{\partial}{\partial z}\right) u(\boldsymbol{r}) = 0. \tag{1.4}$$

The LG modes, forming a complete set of solutions for Eq. (1.4), are given

by

$$u^{LG}(\boldsymbol{r}) = \frac{1}{\sqrt{|w(z)|}} \left(\frac{\rho}{w(z)}\right)^{|m|} L_p^{|m|}\left(\frac{2\rho^2}{w(z)^2}\right) \times e^{-\frac{ik\rho^2 z}{z^2+Z^2}} e^{-i\chi(z)(|m|+2p+1)} e^{im\phi} e^{-\frac{\rho^2}{w(z)^2}}, \tag{1.5}$$

where the integers p and m label the mode, and $L_p^{|m|}$ is the associated Laguerre polynomials. We note that by setting $p = m = 0$, Eq. (1.5) falls into the usual Gaussian beam. The beam width $w(z) = w\sqrt{1 + \frac{|z|}{Z}}$ takes its minimum w, called the beam waist, at $z = 0$. The Rayleigh range Z, determined by the optical system, is the distance from the focal plane along the propagation axis at which the cross-section of the beam becomes twice the minimum value. The phase factor determined by $\chi(z) = \tan^{-1}\left(\frac{z}{Z}\right)$ is called the Gouy phase. As we have already mentioned, the twisted phase factor $e^{im\phi}$ in Eq. (1.5) yields OAM $\hbar m$ and the topological singularity $u^{LG}(0, \phi, z) = 0$ at $\rho = 0$. We again emphasize that the OAM is a property of $u(\boldsymbol{r})$ or $\psi(\boldsymbol{r})$ and nothing to do with the polarization vector $\hat{e}$.

In this thesis, we mostly consider two-dimensional (2D) systems and only need the fields at the focal plane ($z = 0$). Then the LG modes are simplified to be

$$u^{LG}(\rho, \phi, 0) = \frac{1}{\sqrt{w}} \left(\frac{\rho}{w}\right)^{|m|} L_p^{|m|}\left(\frac{2\rho^2}{w^2}\right) e^{im\phi} e^{-\frac{\rho^2}{w^2}}. \tag{1.6}$$

In addition to the topological singularity at $\rho = 0$, when the radial index p is non-vanishing, the associated Laguerre polynomial bears p different nodes along the radial coordinate. As a whole, the field intensity (averaged over the temporal period) takes the form of $(p + 1)$-fold rings. In Fig. 1.1 we show the time-averaged intensity profiles of Gaussian beams and OVs.

The generation of OVs is simple and has been already established [42]. We can use artificial dislocations to induce the singularity in the propagating beams and transforms them to OVs. Spiral phase plates are the common way of realizing that and are commercially available. Holograms are convenient as well for that purpose. In addition to them, today a number of different methods like synchrotrons [46] and metamaterials [47] are known.

Applications of OVs are actively explored. We can transfer their OAM to classical particle or excitons to induce rotational motion of them [48, 49] or use their phase structure to realize super-resolution microscope [50] and chiral laser ablation [51, 52, 53, 53] to name a few. The most important one

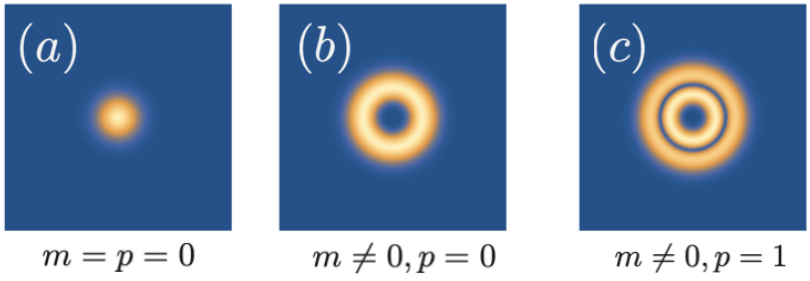

Figure 1.1: In-plane field intensity distribution averaged over the period of the beam. (a) Gaussian beam ($m = p = 0$). (b) OVs with $p = 0$ and $m \neq 0$ (c) OV with $p = 1$ and $m \neq 0$. The value of the OAM m is not essential for the topology of the averaged intensity unless nonzero. The radial index p determines the number of nodes of the associated Laguerre polynomials, thus of the rings.

is the stimulated emission depletion (STED) microscope [50] which allows us to observe objectives with resolution beyond the diffraction limit. Using STED microscopes, we can now perform high-resolution and non-invasive measurement of living cells. OVs are playing the central role in realizing this groundbreaking technology and in 2014, three researchers, E. Betzig, S. W. Hell, and W. E. Moerner won the Nobel Prize in chemistry for their contributions to developing the STED microscope [54]. Recently, OVs are also becoming important for the telecommunication. The OAM degrees of freedom could be a new information carrier inside optical fibers [55]. Since there is no upper limit in the OAM carried by OVs, using OVs for the multimode information transfer could result in the drastic speedup of the telecommunication in the future.

In the field of optics, as we saw above, OVs have been already a central subject and studied intensively under the name of *singular optics* or *structured light optics*. However, applications of OVs in the context of optical physics have been unexplored. One of our goals in this thesis is to develop a field we may call **singular optical physics**. We are to find applications of OVs (more generically of topological lightwaves) in probing and controlling microscopic degrees of freedom in solid-state systems.

Among various applications of OVs developed in optics, the work by Toyoda et al. [53, 56] is particularly a stimulating one for us. In the work, they apply OVs for the laser ablation of (laser engraving to) a metal. In the laser ablation, an intense light pulse is shone on a surface of a target to evaporate atoms and form a pattern. They found that the processing

with OVs leaves after three-dimensional structures, which they call chiral nano-needles. The spiral phase structure of the incident OVs results in the different strength of the ablation at each point, making the processed surface to have such a unique profile (see Fig. 1.2).

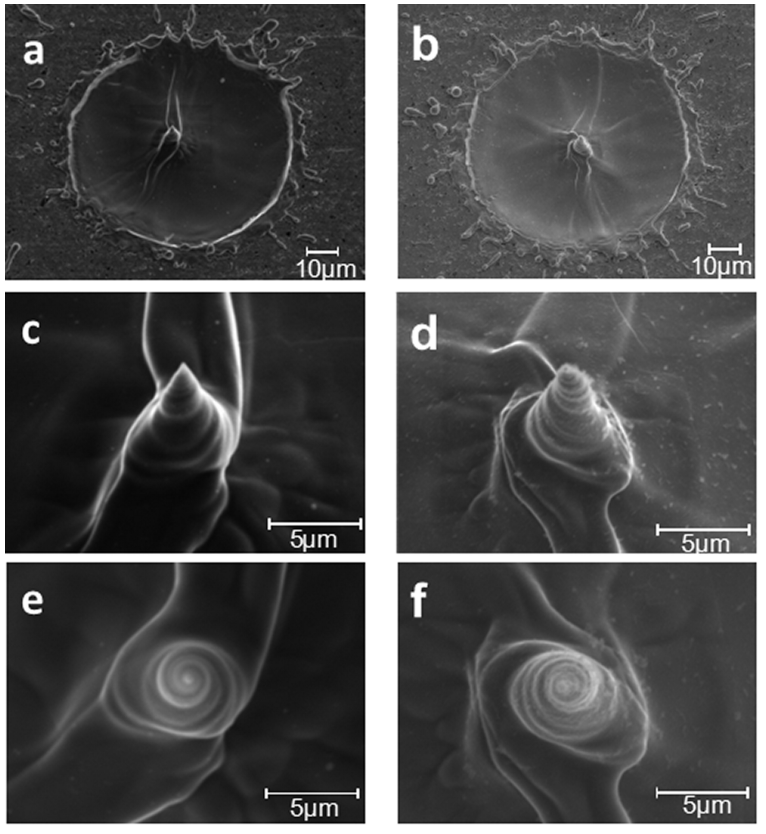

Figure 1.2: Chiral nano-needles created by the laser ablation with OVs. The left panels are for an OV with a total angular momentum of -2, and the right ones are for that of $+2$. *Note: the figure is taken from Ref. [56] with a permission from ACS (the direct link to the article: https://pubs.acs.org/doi/10.1021/nl301347j). Further reuse of this material requires another permission from ACS.*

Regarding the generation of the chiral nano-needle structures as "printing" of the spatial profile (phase or intensity) of OVs to a physical system, as a natural extension of that, we hit on the possibility of their microscopic analogue, i.e. encoding of the spatial profile of OVs into solids by using electronic or magnetic degrees of freedoms. This would be the main content of the second chapter.

1.2.2 Cylindrical vector beams

Next, we move onto another type of the topological lightwaves: cylindrical vector beams (CVBs) [57]. Unlike OVs, CVBs do not carry orbital angular momentum and the phase structure of CVBs is in that sense, topologically trivial. However, CVBs are still topological in that they have "vortical" polarizations.

There are two types of CVBs, namely radial and azimuthal CVBs. If we denote the in-plane component of the polarization vector of CVBs as $\boldsymbol{e}_p$, the former has $\boldsymbol{e}_p^r = \hat{\rho} = (\cos\phi, \sin\phi)$ and the latter does $\boldsymbol{e}_p^a = \hat{\phi} = (-\sin\phi, \cos\phi)$. That is, the polarization vectors are coordinate dependent (dependent on the azimuthal coordinate ϕ) and have a vortical profile. These are in contrast to the Gaussian lasers and OVs as both of them have spatially homogeneous polarization vectors. Nevertheless, as we will see below, CVBs are mathematically described as a superposition of OVs (and generated as such).

Let us take two circularly polarized OVs with OAMs $= \pm 1$. Aside from the radial (scalar) part, their electric fields are written as

$$\boldsymbol{e}_1 = (\hat{x} - i\hat{y})e^{i\phi}, \tag{1.7}$$

$$\boldsymbol{e}_{-1} = (\hat{x} + i\hat{y})e^{-i\phi}. \tag{1.8}$$

By superimposing them, we can construct both the radial and azimuthal polarizations as:

$$\boldsymbol{e}_p^r = \frac{1}{2}\Re\left(\boldsymbol{e}_1 + \boldsymbol{e}_{-1}\right), \tag{1.9}$$

$$\boldsymbol{e}_p^a = \frac{1}{2}\Re\left(i\boldsymbol{e}_1 - i\boldsymbol{e}_{-1}\right). \tag{1.10}$$

By construction, these CVBs do not carry OAMs unlike OVs. Since CVBs are characterized as their polarization profile, they can carry OAMs in general. Namely, being OVs and CVBs are not exclusive. However, in this thesis, to simplify the argument, we take into account either OAMs or vortical polarization, and we only deal with the simplest radial and azimuthal CVBs.

In Fig. 1.3, we compare the conventional Gaussian beam with topological lightwaves (OVs and CVBs). The arrows in the figure correspond to the in-plane electric field of these beams propagating perpendicularly to the x-y plane. The field configuration of the Gaussian beam is simple [see Fig. 1.3(a)]. The polarization is spatially homogeneous, and its amplitude is the strongest at the center, having Gaussian tails. Figure 1.3(b) is of a

linearly polarized OV with OAM of unity. The field direction is inhomogeneous owing to the spiral phase structure, and the field amplitude vanishes at the center due to the topological singularity. The field configuration of azimuthal and radial CVBs are shown in Fig. 1.3(c, d). There, we see vanishing intensity as well as the radially anisotropic field configurations due to the vortical polarization vectors.

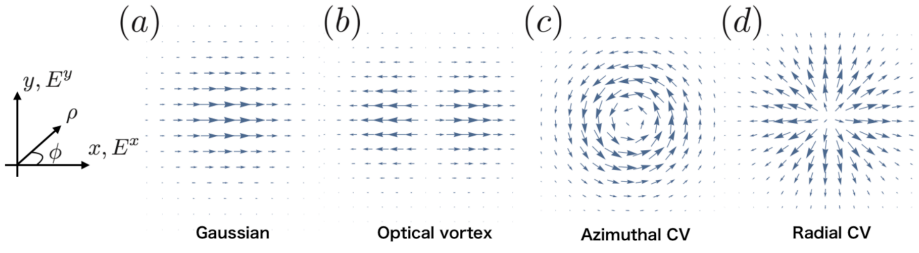

Figure 1.3: Snapshots of the in-plane (x and y) components of the electric field of (a) linearly polarized Gaussian beam, (b) linearly polarized Optical vortex with unit orbital angular momentum, (c) azimuthal CVB, and (d) radial CVB. The field amplitude of the Gaussian beam is the strongest at the center while beams (b)-(d) have vanishing in-plane components at the center due to their topological nature. The size of the arrows in the figure corresponds to the laser amplitude at each point. We show the definition of (ρ, ϕ) in the cylindrical coordinate for later use.

The most important feature of CVBs manifests itself when they are tightly focused by a lens [58, 59]. To make the argument concrete, below we give more precise mathematical description of CVBs on the occasion of focusing. The following argument follows Ref. [58]. As we mentioned, the radial and azimuthal polarizations themselves can be constructed from OVs, but in discussing the focusing properties of CVBs, we have to take into account the longitudinal component of the polarization vector in addition to the vortical in-plane polarization.

The geometry of focusing is shown in Fig. 1.4. We assume that the incident beam is propagating along the vector $\boldsymbol{k} = \hat{z}$ and that the polarization vector $\boldsymbol{e}_p$ of the incident beam is purely in-plane. We take a radial unit vector $\boldsymbol{g}_0 = \cos\phi\hat{x} + \sin\phi\hat{y}$. The azimuthal component is then denoted as $\boldsymbol{g}_0 \times \boldsymbol{k}$. Using $\boldsymbol{g}_0$ and $\boldsymbol{g}_0 \times \boldsymbol{k}$ we can write the electric field of the incident beam as

$$\boldsymbol{e}_0 = l_0(\rho)\left[e_r \boldsymbol{g}_0 + e_a \boldsymbol{g}_0 \times \boldsymbol{k}\right], \tag{1.11}$$

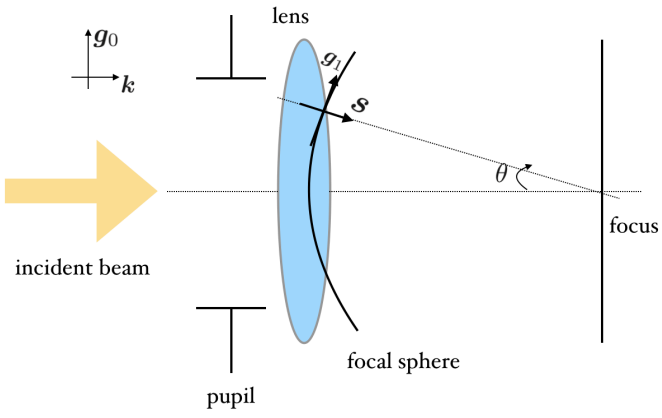

Figure 1.4: Setup of the focusing of the incident CVBs by the lens. The lens transforms the incident beam in the coordinate subscripted with zero into that in the coordinate subscribted with one on the focal sphere. The angle θ specifies the position on the focal sphere whose maximum value α is determined by the property of the optical system. The pupil-apodization function encodes the beam profile at the pupil.

where the constants e_r and e_a specify the field amplitudes of the radial and azimuthal components respectively. Here $l_0(\rho)$ specifies the field amplitude of the incident beam and thus is dependent on the radial coordinate of the incident beam ρ but preserves the cylindrical symmetry.

An aplanatic lens placed after the entrance pupil generates spherical waves in response to the incident beam. The beam distribution at the pupil is then mapped onto the wavefront determined the ray projection function $g(\theta)$ as

$$\rho/f_1 = g(\theta), \tag{1.12}$$

where f_1 is the focal length. With the ray projection function, we can calculate the field distribution on the wavefront $l_1(\theta)$ based on the energy conservation of the propagating beam:

$$l_0(\rho)^2 2\pi\rho d\rho = l_1(\theta)^2 2\pi f_1^2 \sin\theta d\theta. \tag{1.13}$$

For typical objective lenses, the sine condition is designed to be satisfied. That is, the ray projection function is given by

$$g(\theta) = \sin\theta. \tag{1.14}$$

As a result, the wavefront becomes spherical, defining the focal sphere with radius f_1. The field distribution is, in this case, obtained as

$$l_1(\theta) = l_0(f_1 \sin\theta)\sqrt{\cos\theta}. \tag{1.15}$$

The lens also transform the polarization vector through the refraction. We represent the "radial" unit vector of the beam on the focal sphere at the point specified by θ as $\boldsymbol{g}_1$ (see Fig. 1.4). In the original coordinate, it is written as

$$\boldsymbol{g}_1 = \cos\theta\,(\cos\phi\hat{x} + \sin\phi\hat{y}) + \sin\theta\boldsymbol{k}. \tag{1.16}$$

The propagation direction on the focal sphere is written as $\boldsymbol{s} = \sin\theta\cos\phi\hat{x} + \sin\theta\sin\phi\hat{y} + \cos\theta\hat{z} = \cos\theta\boldsymbol{k} + \sin\theta\boldsymbol{g}_0$.

The Richard-Wolf theory [60] tells us that the field near the focus is given by the diffraction integral of the field strength factor $\boldsymbol{a}_1$ over the focal sphere:

$$\boldsymbol{e}^s = \frac{-ik}{2\pi}\int d\Omega \boldsymbol{a}_1(\theta,\phi)e^{ik\boldsymbol{r}\cdot\boldsymbol{s}}, \tag{1.17}$$

where $\boldsymbol{r}$ specifies the point near the focus at which we measure the focused electric field, and $d\Omega$ is an integral over the solid angle. The factor $\boldsymbol{a}_1(\theta,\phi)$ is associated to the electric field on the focal sphere as $\boldsymbol{a}_1 = f_1\boldsymbol{e}_1$ [60].

The field on the focal sphere is written as $\boldsymbol{e}_1 = l_1(\theta)\hat{e}_1$. Here $\hat{e}_1$ is the vector in the direction of the field $\hat{e}_1 = [e_r\boldsymbol{g}_1 + e_a\boldsymbol{g}_1 \times \boldsymbol{s}]$. Comparing $\hat{e}_1$ with the incident field Eq. (1.11) helps us to understand the effect of focusing. That is, $l_0(\rho)$, $\boldsymbol{g}_0$, and $\boldsymbol{k}$ are mapped to $l_1(\theta)$, $\boldsymbol{g}_1$, and $\boldsymbol{s}$ respectively. The pupil-apodization function $l_0(\rho)$ is somewhat arbitrary since we can control it by using various filters at the pupil. As we see in a later chapter, the details of the apodization function is not essential for our arguments in this thesis. In the following, we redefine $l_0(f_1\sin\theta)$ as $l_0(\theta)$ to simplify the expression.

Summarizing above, the electric field near the focus is represented in the following form (see also Fig. 1.4):

$$\begin{aligned}\boldsymbol{e}^s = -\frac{ikf_1}{2\pi}\int_0^{\alpha}\int_0^{2\pi} & d\Omega \sin\theta\sqrt{\cos\theta}l_0(\theta)e^{ik\boldsymbol{r}\cdot\boldsymbol{s}} \\ & \times\left[e_r\begin{pmatrix}\cos\theta\cos\phi\\ \cos\theta\sin\phi\\ \sin\theta\end{pmatrix} + e_a\begin{pmatrix}-\sin\phi\\ \cos\phi\\ 0\end{pmatrix}\right].\end{aligned} \tag{1.18}$$

This is the general form of the focused CVBs. More specifically, let us consider the case in which the incident beam is purely azimuthal: $e_r = 0$. The corresponding magnetic field components of the focused beam are obtained by solving Faraday's equation, and the electromagnetic fields are obtained to be:

$$\begin{aligned} E^{\rho}(\rho,\phi,z) &= E^{z}(\rho,\phi,z) = B^{\phi}(\rho,\phi,z) = 0, \\ E^{\phi}(\rho,\phi,z) &= 2A\int_0^{\alpha} \sin\theta f(\rho,\theta,z,1)d\theta, \\ B^{\rho}(\rho,\phi,z) &= -\frac{2}{c}A\int_0^{\alpha} \sin\theta\cos\theta f(\rho,\theta,z,1)d\theta, \\ B^{z}(\rho,\phi,z) &= \frac{2}{c}A\int_0^{\alpha} \sin^2\theta f(\rho,\theta,z,0)d\theta, \\ f(\rho,\theta,z,n) &= \cos^{\frac{1}{2}}(\theta)\ell_0(\theta)J_n(k\rho\sin\theta)e^{ikz\cos\theta}, \end{aligned} \tag{1.19}$$

where c is the speed of light in a vacuum. Here the field amplitude A is defined to be $A = kf_1e_a/2$. The radial profile of the beams is governed by the Bessel function $J_n(x)$. Due to the property of the Bessel functions, all field components vanish at the center $\rho = 0$ **except the z component of the magnetic field**. The longitudinal component of the magnetic field is, on the other hand, strongest at the center.

As a whole, the field distribution of the tightly focused azimuthally polarized CVB is given as Fig. 1.5. Here, we take the pupil-apodization function [58] as

$$\ell_0(\theta) = \exp\left[-\beta^2\left(\frac{\sin\theta}{\sin\alpha}\right)^2\right] J_1\left(2\beta\frac{\sin\theta}{\sin\alpha}\right), \tag{1.20}$$

where β is the ratio of the radius of the pupil and the beam waist and the maximum angle α is determined as $\alpha = \sin^{-1}(\mathrm{NA}/n)$ with NA being the numerical aperture of the lens. This figure also gives an intuitive understanding of the mechanism bearing the longitudinal magnetic field.

Figure 1.5 (b) shows that near the center the longitudinal magnetic field is the only non-vanishing component. Therefore, if a sample with its size sufficiently smaller than the wavelength is placed at the focus, we can virtually apply a "pure magnetic field at the optical frequency" without accompanied by any electric fields (and other components of the magnetic fields). We note that if we focus a radial CVB, there appears a longitudinal electric field in the same way.

The longitudinal magnetic field at the optical frequency is unique to

the azimuthal CVBs. The use of equipment like coils/solenoids is limited to frequencies lower than gigahertz (GHz). From the condensed-matter viewpoint, the purely longitudinal field at high (e.g. THz) frequency will provide a new, powerful tool for studying various (collective) physics in solids. This would be the main content of Chapter 3. There, we also discuss an application of the electric field component of the azimuthal CVBs to study and control circulating currents at the edges of topological insulators. Moreover, we discuss applications of radial and azimuthal CVBs for Floquet engineering [20, 21, 22].

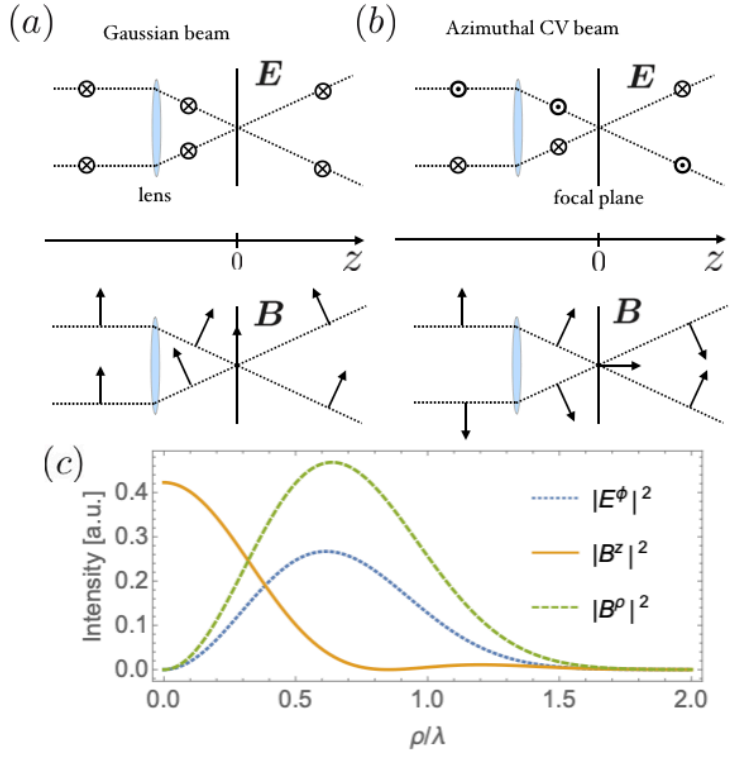

Figure 1.5: (a), (b): Focusing of the Gaussian beam and the azimuthal CVB. The characteristic spatial profile of the polarization vector of the azimuthal beam results in the vanishing electric field and the growth of the longitudinal magnetic field near the focus. (c) The intensity distribution of the azimuthal beam in the focal plane at $z = 0$. The horizontal axis is the distance from the center of the focal plane. We take $\beta = 3/2$, $n = 1.0$, and NA $= 0.95$ in the panel (c). As the focusing becomes tighter, this longitudinal field becomes more prominent.

1.3 About this thesis

This thesis theoretically deals with potential applications of topological lightwaves to condensed-matter physics (and chemistry in part). The rest of this thesis is organized as follows. In this chapter, we introduced topological lightwaves, the main players of our study. In the second chapter, we discuss how to utilize OVs for ultrafast magnetism. In particular, we discuss how OVs could be useful in controlling the magnetic texture of chiral magnets. This part will be based mainly on Refs. [61, 62]. In the third chapter, we consider applications of CVBs for physics and (bio-) chemistry. We propose a novel scheme of measuring electronic properties of magnets and show how CVBs can be useful for spectroscopic uses, control of circulating currents, and Floquet engineering. This chapter will be based on Refs. [63, 64]. The final chapter will be devoted to concluding remarks and outlook, followed by the publication list and references.

Chapter 2

Optical vortices (OVs)

In this chapter, we discuss applications of optical vortices (OV) to ultrafast magnetism. We argue how to exploit the characteristic spatial profile of OVs for controlling the spin texture of solids. We first give a brief review of chiral magnets and topological defects, skyrmions and their generalizations. We discuss why OVs are potentially useful for generating topological defects in chiral magnets and give concrete examples of applications. We show that with OVs we can shape the wavefront of spin waves in magnets, transfer their OAM as topological defects in chiral magnets, and generate a family of topological defects in both ferromagnetic and antiferromagnetic chiral magnets. This chapter is based on Refs. [61, 62].

2.1 Optical vortices for magnetism

In this section, we review chiral (ferro) magnets and skyrmionic defects in them. We introduce static properties of chiral magnets and the nature of the topological magnetic defects in them. We discuss an important issue to be resolved in developing applications of OVs for ultrafast magnetism: namely, a discrepancy in the spatio-tempral scales between lights and magnets.

2.1.1 Chiral magnets and their topological defects

In this part, we shortly review basic properties of chiral ferromagnets (FMs) [65, 66]. We show their ground-state phase diagram and introduce the magnetic defects, skyrmions in them.

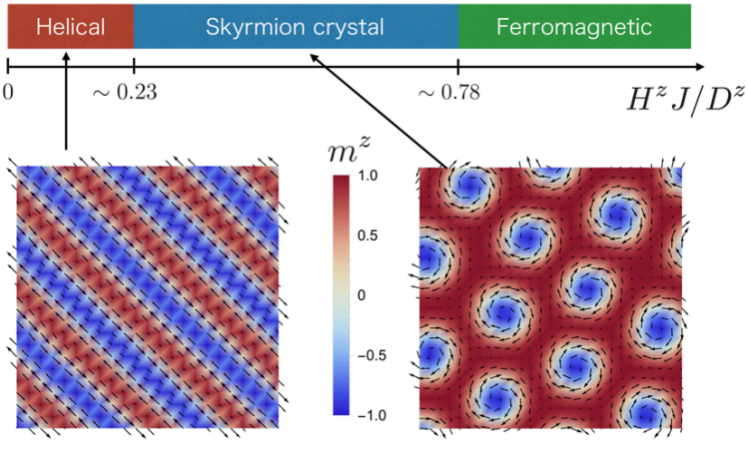

Figure 2.1: Ground-state phase diagram of a model of chiral ferromagnets (2.1) (reproduced from Ref. [67]). There are three distinct phases depending on the external magnetic field in the out-of-plane direction (taken to be the z direction). We draw the spin textures in the helically ordered and the skyrmion crystal phases obtained by numerical simulations based on the Landau-Lifshitz-Gilberg equation, using arrows and colors. We also show the critical values of the phase boundaries.

Phase diagram and skyrmions

Chiral FMs such as MnSi [68, 69, 70, 71], $Fe_{1-x}Co_xSi$ [72, 73], or FeGe [74, 75, 76], are characterized by their noncentrosymmetric lattice structures. The symmetry breaking induces the Dzyaloshinsky-Moriya (DM) interaction, which adds a twist to the spin texture in these materials. As a canoni-

cal model of chiral FMs, the following two-dimensional square-lattice model is well accepted:

$$H = -J \sum_{\boldsymbol{r}} \boldsymbol{m}_{\boldsymbol{r}} \cdot \left(\boldsymbol{m}_{\boldsymbol{r}+a\boldsymbol{e}_x} + \boldsymbol{m}_{\boldsymbol{r}+a\boldsymbol{e}_y} \right) + \sum_{\boldsymbol{r}} \boldsymbol{D}_i \cdot (\boldsymbol{m}_{\boldsymbol{r}} \times \boldsymbol{m}_{\boldsymbol{r}+a\boldsymbol{e}_i}) - H^z \sum_{\boldsymbol{r}} m^z_{\boldsymbol{r}}, \tag{2.1}$$

where a is the lattice constant and $\boldsymbol{e}_i$ is the unit vector along the i-axis ($i = x, y$). The vector $\boldsymbol{m}_{\boldsymbol{r}}$ represents the magnetic moment at the site $\boldsymbol{r}$[1]. In the following, we take $\boldsymbol{m}$ to be a vector with a unit length. This model contains two inter-spin interactions; the ferromagnetic Heisenberg interaction $J > 0$ and the DM interaction. The DM vector $\boldsymbol{D}_i$ is defined on the bonds $(\boldsymbol{r}, \boldsymbol{r} + a\boldsymbol{e}_i)$. The last term is the Zeeman coupling with an external magnetic field applied in the z-direction.

The model Eq. (2.1) is a fairly simple one, but is known to reproduce many experimental results in thin-film chiral magnets [77]. As long as we are interested in the long-wavelength physics like spin waves or magnetic defects much larger than the lattice constant, the model (2.1) would work as a standard model.

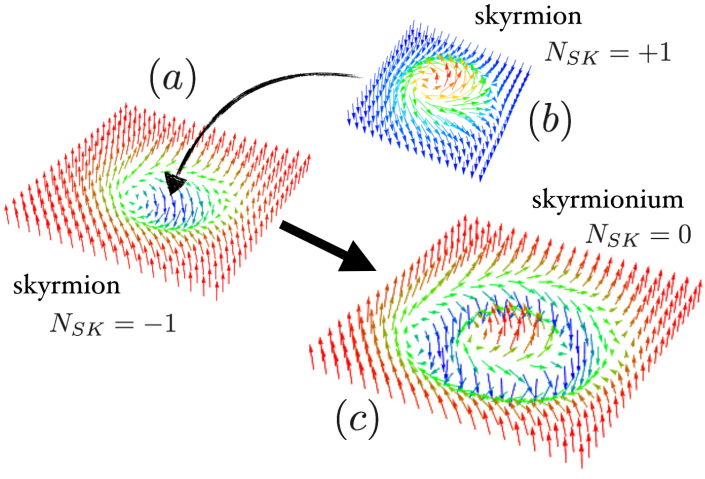

Figure 2.2: (a, b) skyrmions with negative and positive topological numbers. (c) skyrmionium as a bound state of these two defects. Arrows represent spins in chiral magnets [see Eq. (2.1)] and the colors represent their z-component (red for $+1$, blue for -1, and green for 0). We take the DM vector to be $\boldsymbol{D}_i = D\boldsymbol{e}_i$ ($D > 0$) and the external magnetic field to be in z-direction $\boldsymbol{H} = \pm H^z \boldsymbol{e}_z$.

[1]By using the electron spin $\boldsymbol{s}$ the magnetic moment $\boldsymbol{m}$ is defined as $\boldsymbol{m} = -\boldsymbol{s}$

Let us see the ground-state phase diagram of the model (2.1) [78]. As shown in Fig. 2.1, depending on the external magnetic field, there appear three distinct phases in the ground state. When the external field is weak enough, the competition between the exchange coupling and the DM interaction results in the helically ordered spin texture. When the external field is strong enough to dominate over the other terms, the ground state is turned into a forced ferromagnetic state in the out-of-plane direction. In between these weak and strong magnetic-field regions, there appears a peculiar phase called the skyrmion crystal phase.

The spin texture of the skyrmion crystal phase is a triangular lattice of point-like magnetic defects called skyrmions [72]. A skyrmion is a highly-stable magnetic defect in chiral magnets with a spin texture shown in Fig. 2.2(a, b). The former is a skyrmion as an isolated defect in the up-spin background while the latter is one in the down-spin background. Skyrmions are characterized by their topological property quantified by the non-vanishing skyrmion number:

$$N_{\mathrm{SK}} = \frac{1}{4\pi} \int \boldsymbol{m_r} \cdot \left(\frac{\partial \boldsymbol{m_r}}{\partial x} \times \frac{\partial \boldsymbol{m_r}}{\partial y} \right) d^2 r. \tag{2.2}$$

In a continuous space, this skyrmion number is quantized to be an integer and take a non-vanishing number for the spin configuration with skyrmions. Since the trivial state, namely the homogeneous ferromagnetic state, has $N_{\mathrm{SK}} = 0$, a spin texture with skyrmions is topologically different from the trivial state. That is, any continuous deformations to the spin texture of skyrmions cannot remove them. This topological nature ensures the stability of skyrmions as magnetic defects. In lattice systems, this topological protection works only imperfectly, but skyrmions are known to be highly stable if their size is much larger than the lattice constant.

Skyrmionium

In chiral FMs, a family of topological magnetic defects exists in addition to skyrmions. An example of such defects is the one shown in Fig. 2.2(c), called a 2π vortex [79] or a skyrmionium [80, 81, 82, 83]. To see the topological nature of the skyrmionium, we present, in Fig. 2.3, the "cumulative" skyrmion number for it :

$$N_{\mathrm{SK}}(R) = \frac{1}{4\pi} \int_{r<R} \boldsymbol{m_r} \cdot \left(\frac{\partial \boldsymbol{m_r}}{\partial x} \times \frac{\partial \boldsymbol{m}}{\partial y} \right) d^2 r. \tag{2.3}$$

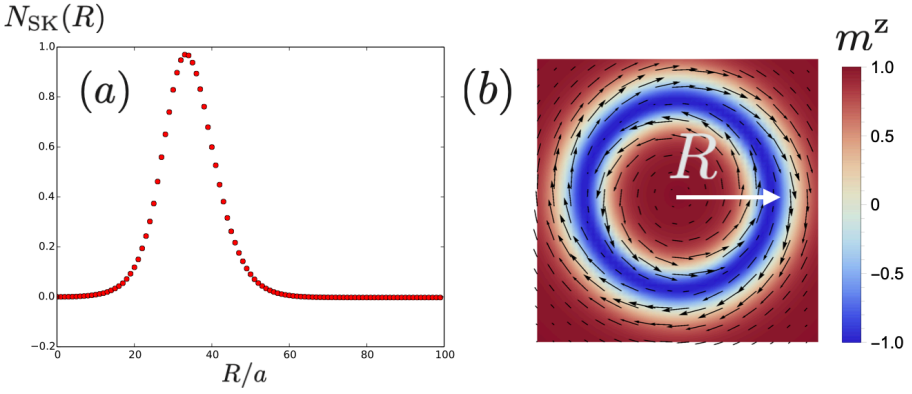

Figure 2.3: (a) Cumulative skyrmion number $N_{\mathrm{SK}}(R)$ of a skyrmionium as a function of R/a, where a is the lattice constant. We take $J = 1$, $D = 0.15$, and $H^{\mathrm{z}} = 0.014$. (b) Definition of R for a skyrmionium. The arrows represent the in-plane components of spins.

The integration is performed within the circle of radius R measured from the center of the defect [see Fig. 2.3(b)]. As Fig. 2.3(a) shows, there appears a bump structure characteristic to a skyrmionium. As a function of the radius of the integration region R, the cumulative skyrmion number grows to approach the saturation value $+1$ of a skyrmion in Fig. 2.2(b) and then drops to zero.

A skyrmionium is a bound state of two skyrmions with the opposite background spins as schematically shown in Fig. 2.2. Since skyrmions in Fig. 2.2(a, b) have the opposite skyrmion number $N_{\mathrm{SK}} = \mp 1$ respectively, as their bound state, the skyrmion number of a skyrmionium is zero [see 2.3(a)]. In this sense, skyrmioniums are topologically trivial. Nevertheless, their local spin configurations are nothing but those of skyrmions as is reflected to the bump structure of the cumulative skyrmion number. Therefore, the topological protection works to stabilize skyrmioniums as well.

More generically, we can consider a general $n\pi$ vortex (see Fig. 2.4). For example, the spin texture of a 4π vortex is shown in Fig. 2.4(b). Although $n\pi$-vortices are excited states of chiral FMs, they are predicted to be long-lived [79] once formed. As for a skyrmionium, it has been already discovered experimentally [80, 83] and confirmed to be stable.

Both OVs and skyrmioniums have topological properties. Both have a ring-shaped spatial profile in the (time-averaged) intensity and the spin

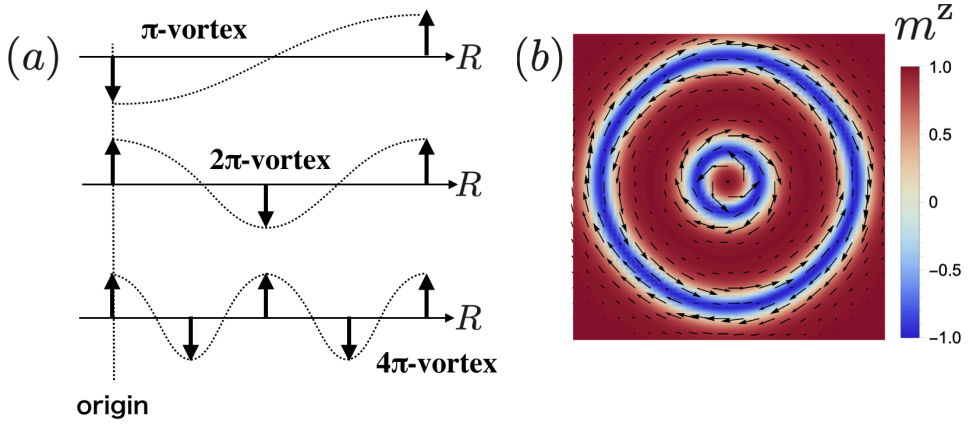

Figure 2.4: (a) Schematic illustration of the definition of an $n\pi$ vortex. The arrows represent the out-of-plane component of spins. For example, 2π vortex, or a skyrmionium has a spin texture whose spin orientation at the center has the relative angle of 2π with respect to the surrounding environment. (b) Spin texture of a 4π vortex defect.

texture. OVs have spiral phase structure inducing a chiral perturbation to the target system (remember the ablation experiment shown in Fig. 1.2), and skyrmioniums have twisted, chiral spin textures. The apparent similarity between them sets our expectations to a novel spin dynamics induced under OVs in chiral FMs. The aim of this Chapter 2 is to explore the interplay of the topology and chirality of OVs and chiral magnets.

Multiferroics

Here we comment on multiferroics [37, 38], a subject closely related to chiral magnets. In a class of matter called multiferroics, there co-exist multiple orders like ferroelectricity, a ferromagnetic order, an orbital ferromagnetic order, and so on. In particular, the coexistence of ferroelectricity and ferromagnetism has been well studied in the context of spintronics. In the presence of both ferromagnetic and ferroelectric orders, so-called the magneto-electric (ME) coupling between the ferroelectric moment $\boldsymbol{P}$ and ferromagnetic moments $\boldsymbol{M}$: $H_{\mathrm{ME}} = \alpha \boldsymbol{P} \cdot \boldsymbol{M}$ [84, 85, 86, 87, 88] appears. This allows us to control the electric polarization with the magnetization and vice versa.

In order for them to coexist, the following conditions have to be met; 1) the system is insulating, 2) the spatial-inversion symmetry should be broken, 3) the time-reversal symmetry should be broken. The former two

are for the existence of the electric polarization and the last one is for that of the magnetization. Chiral magnets are a natural example meeting these conditions. They have magnetic orders breaking the time-reversal symmetry and their lattice structures break the inversion symmetry, inducing the DM interaction. Therefore, in insulating chiral magnets, we can use the electric field component of the incident OVs as well as the magnetic one to affect the magnetic properties of the target. In the later section, we will come back to this point.

2.1.2 Scales of lights and magnets

Our goal of this chapter is to propose applications of OVs for ultrafast magnetism of (chiral) magnets. As we explained in the previous chapter, OVs are characteristic in their spiral phase structure and the intensity profile. It is a natural expectation that the competition between the chiral nature of OVs and that of chiral magnets would result in characteristic ultrafast dynamics. The ring-shaped profile of the (time-averaged) intensity of OVs also seems to be compatible with the spin texture of $n\pi$ vortices.

In developing applications of OVs to controlling magnetic properties of matter, however, we have to be serious about the difference of the spatio-temporal scales of lights and magnets. As long as we are working on the long-wavelength physics in magnets, i.e. spin waves, there is no problem. The length scale of the incident light and the target system are automatically matched to induce characteristic dynamics. This will be the content of Sec. 2.2. However, if we want to use OVs to generate topological defects, a problem arises.

In chiral FMs, the length scale determining the size of a skyrmion is governed by the competition among exchange coupling, the DM interaction, and the external field. Our naive expectation is that in order for the OVs to offer a way of generating magnetic defects, the beam waist should be comparable with the stable size of magnetic defects in the target material. Since the stable size of skyrmions (and other topological defects) in chiral FMs is typically O(10) to O(1,000) nanometers, the beam waist should be in this region. If there is no way of breaking the diffraction limit (this will be discussed in Sec. 2.3), this means that the wavelength of the applied OVs should be around this value. Hence, we have to work on visible lights to extreme ultraviolet (EUV) lights.

Having OVs of this frequency is not at all problematic [89, 90]. The problem is the timescale. The frequency of a laser with the wavelength of 10 nm is about 30 petaherz (PHz). This is much faster than the dynamics

of spins in magnetic materials. The typical timescale of magnetization dynamics in solids is GHz to THz, so that OVs with the beam waist of the order of the size of magnetic defects is too fast for spins to follow. Hence, they will not be able to induce any coherent dynamics of spins as they are. Nevertheless, we can consider an incoherent coupling and use the effect of heating to develop a way of ultrafast, systematic generation of a family of topological defects in chiral magnets. This will be the content of Sec. 2.4.

We note that formally it is possible to discuss, for example, the change of the selection rule of the optical transitions due to the non-vanishing OAMs carried by OVs. However, we have to be careful about the result. Neglecting the large deviation in the spatio-temporal scales between lights and matters will lead to neither reliable nor meaningful arguments.

2.2 Shaping spin waves with OVs

As we discussed in the previous section, the problem of the deviation in spatio-temporal scales does not take place for spin waves with the wavelength around $\boldsymbol{k} = \boldsymbol{0}$. The spatial scale of the spin wave physics [91, 92] induced by the external (long-wavelength) perturbation is automatically matched with that of the perturbation. Hence, we only have to pay attention to the timescale. In this section, we study spin waves excited by (sub-) THz OVs. In particular, when the frequency of OVs and the excitation energy of the spin wave coincide with each other, a magnetic resonance occurs and a large number of magnons are excited, resulting in spin waves of large amplitude. In this part, we consider a Zeeman coupling between magnetic moments and the magnetic field component of OVs.

We consider a simple ferromagnet on a square lattice:

$$H = -J \sum_{\langle \boldsymbol{r}\boldsymbol{r}' \rangle} \boldsymbol{m}_{\boldsymbol{r}} \cdot \boldsymbol{m}_{\boldsymbol{r}'} - H^z \sum_{\boldsymbol{r}} m^z_{\boldsymbol{r}} - \sum_{\boldsymbol{r}} \boldsymbol{B}_{\boldsymbol{r}}(t) \cdot \boldsymbol{m}_{\boldsymbol{r}}. \tag{2.4}$$

As we mentioned, though the microscopic spin Hamiltonian of real materials is far more complex, concerning macroscopic phenomena like long-wavelength spin wave, a simplified model like (2.4) well describes the system. We can regard Eq. (2.4) as discretization of a coarse-grained continuous model at long wavelength.

There is no DM interaction and no characteristic length scale other than the lattice constant in this model. The last term of Eq. (2.4) is the Zeeman coupling between the magnetic field of an OV $\boldsymbol{B}_{\boldsymbol{r}}(t)$ and the magnetic moment at site $\boldsymbol{r}$. We assume that the system is placed at the focal plane of the OV and take the magnetic field $\boldsymbol{B}_{\boldsymbol{r}}(t)$ as an LG mode with $p = 0$;

$$\boldsymbol{B}_{\boldsymbol{r}}(t) = \mathrm{Re}\left[B_0 \boldsymbol{e}_p \frac{\left(\frac{\rho}{w}\right)^{|m|} L_p^{|m|}\left(\frac{2\rho^2}{w^2}\right) e^{-\frac{\rho^2}{w^2}} e^{im\phi - i\omega t - \frac{t^2}{\sigma^2}}}{\max_{\boldsymbol{r}}\left[\left| \left(\frac{\rho}{w}\right)^{|m|} L_p^{|m|}\left(\frac{2\rho^2}{w^2}\right) e^{-\frac{\rho^2}{w^2}} \right| \right]} \right]. \tag{2.5}$$

Here we take the peak value of the magnetic field within the focal plane as B_0 and assume a pulse-like temporal profile with the pulse width determined by the constant σ. The in-plane field distribution of OVs is presented in Fig. 2.5. Depending on the sign of m, these magnetic field distributions rotate in either clockwise or counter-clockwise way. We emphasize that the polarization vector $\boldsymbol{e}_p$ can be complex.

In this and the next sections, we ignore the effect of heating caused

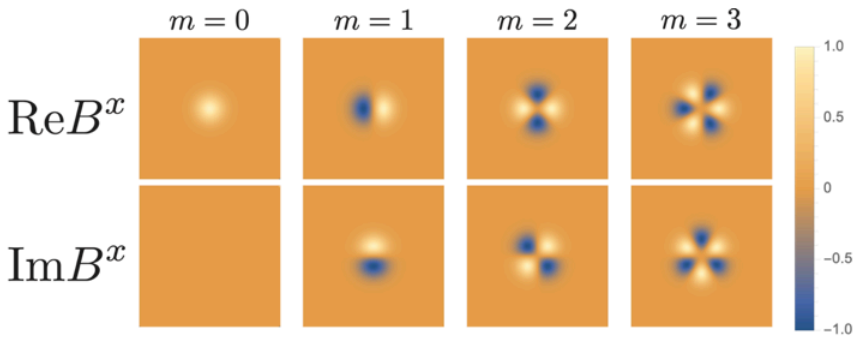

Figure 2.5: Snapshots of the spatial profile of the x-component of magnetic fields Eq. (2.5). For a beam with OAM $\neq 0$, if we go around the topological singularity at $\rho = 0$, the magnetic field changes its sign $2m$ times. The peak values of the fields are normalized to unity.

by the laser application as it is known to be small in the THz region. Indeed, magnetic resonance experiments for THz light can be well explained by theories without taking the heating effect into account (for example, Refs [14, 87]).

The time evolution of classical spins under the drive can be directly studied with the Landau-Lifshitz-Gilbert (LLG) equation [77]. In the framework of the LLG equation, the dissipation of the angular momentum to, for example, a phonon system is taken into account in the form of a phenomenological damping term. The LLG equation is written as

$$\frac{d\boldsymbol{M_r}}{dt} = -\gamma \boldsymbol{M_r} \times \left(-\frac{\partial H}{\partial \boldsymbol{M_r}} \right) + \alpha \frac{\boldsymbol{M_r}}{|\boldsymbol{M_r}|} \times \frac{d\boldsymbol{M_r}}{dt}, \tag{2.6}$$

where α in the second term is a dimensionless parameter characterizing the damping strength. Here $\boldsymbol{M_r} = \hbar\gamma \boldsymbol{m_r}$ and γ is the gyromagnetic ratio $\gamma = g\mu_B/\hbar$. The LLG equation describes the precession of the magnetic moment $\boldsymbol{M_r}$ around the effective magnetic field $(-\partial H/\partial \boldsymbol{M_r})$ which is determined by external fields, magnetic anisotropies, and interactions with other spins. Since the spin configuration around a particular $\boldsymbol{M_r}$ varies in time, the effective field is time-dependent in general. By solving Eq. (2.6) numerically, we obtain the magnetization dynamics. In all the calculations of this section, we assume the initial state to be the uniform FM state in the $+z$ direction.

If we take the radial index of the OV to be zero, the beam is parametrized by the frequency ω, pulse width σ, beam waist w, and OAM m. In the fol-

lowing, we measure ω in the unit of the exchange coupling J and the time t in the unit of $\hbar/J$. Typically the energy scale of the exchange coupling of magnets is at O(1-10) meV, so that $\hbar/J$ is of the order of 0.1 ps.

Although it is rather difficult to directly simulate the model (2.4) in the scale of THz OV ($> 100\mu$m), because of the scale-free nature of the spin wave in the long-wavelength regime, as long as the beam waist is sufficiently longer than the lattice constant, qualitatively its value does not matter, and we can take an artificially small value of w (for example $w = 7.5a$) to study the qualitative aspects of the spin wave physics induced with the OV [62]。

2.2.1 At the magnetic resonance

First, we consider the excitation of spins by linearly polarized, resonant lasers ($\omega = H^z$) with the polarization vector $\boldsymbol{e}_p = \hat{x}$. If the applied beam is a Gaussian one without OAM, both the external drive and the model are radially isotropic in the scale of the wavelength. As a result, the wavefront of the excited spin waves becomes rotationally symmetric.

In contrast, if we use OVs to excite spin waves, we obtain a qualitatively different outcome as shown in Fig. 2.6(a, b). We see that the wavefronts of the spin waves become spiral shaped for OVs. In the Fig. 2.6(c) we show the temporal profile of the incident OV. The spin texture is modulated from the collinear ferromagnetic state in a radially anisotropic way. As a result, if (and only if) the laser beam carries OAM, we can dynamically induce net scalar spin chirality $\chi_{i,j,k} = \boldsymbol{S}_i \cdot (\boldsymbol{S}_j \times \boldsymbol{S}_k)$ [70, 93, 94] (j, k are neighboring sites of the site i) as shown in Fig. 2.6(d).

2.2.2 Off resonance: fast drive

Next we consider the case in which the frequency of the applied field is larger than both the exchange coupling and the resonance frequency $\omega_0 = H^z$. For Gaussian beams, the result is qualitatively the same as the resonance case; isotropic propagation of spin waves (but with much smaller amplitude). However for OVs as we show in Fig. 2.7 the wavefronts in this case have multipolar shapes. Depending on the absolute value of the OAM carried by the OV, we obtain spin waves with a shape of dipolar, quadrupolar, octapolar, and so on.

We have seen that by using OVs we can excite spiral-shaped or multipolar spin waves in magnets. The results above do not depend on the details of the model and would hold also for ferrimagnets and antiferromag-

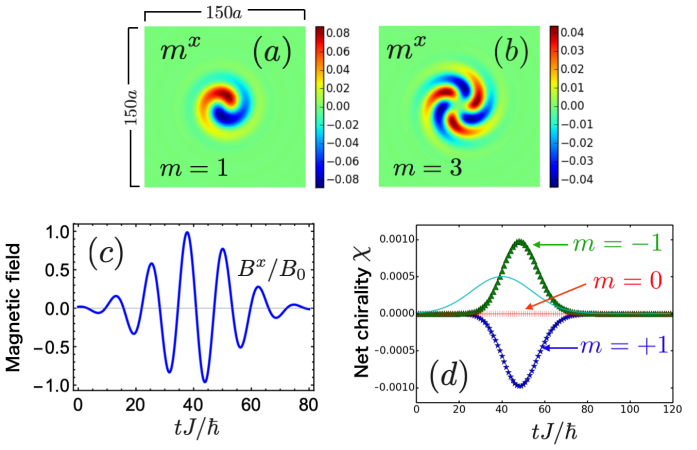

Figure 2.6: Spiral spin waves induced by linearly polarized optical vortices (a, b) at the magnetic resonance $H_z = \omega = 0.3$ (other parameters are the same as Fig. 2.7) and the dynamically induced total scalar spin chirality for $m = 0, \pm 1$ (d). Due to the anisotropic spin wave structure, we observe non-vanishing, OAM dependent net scalar spin chirality for $m \neq 0$. We also present the temporal profile of the field (c) for $m = 1$ at $\rho = w/\sqrt{2}$ and $\phi = 0$. For $J = 5$ meV, the case $\omega = H_z = 0.3$ corresponds to 0.4 THz and 26 Tesla. The solid line in (d) is the envelope of the incident field.

nets. By using the ultrashort laser pulses, nowadays we can observe the propagation of spin waves in the space-time resolved way [95, 96] as shown in Fig. 2.8. Hence, the observation of the anisotropically propagating spin waves is feasible.

Optical excitation and control of spin waves is a developing field. With various optics and electronics techniques, we can control the spatio-temporal profile of electromagnetic fields in details. On the other hand, controlling the propagation of spin waves is by far difficult. Today, using lasers with a nontrivial spatial profile is considered to be a route toward it [95] (see Fig. 2.8). The use of OVs is, therefore, a new option to achieve the detailed control of spin waves, which could lead to new functionalities of magnetic materials.

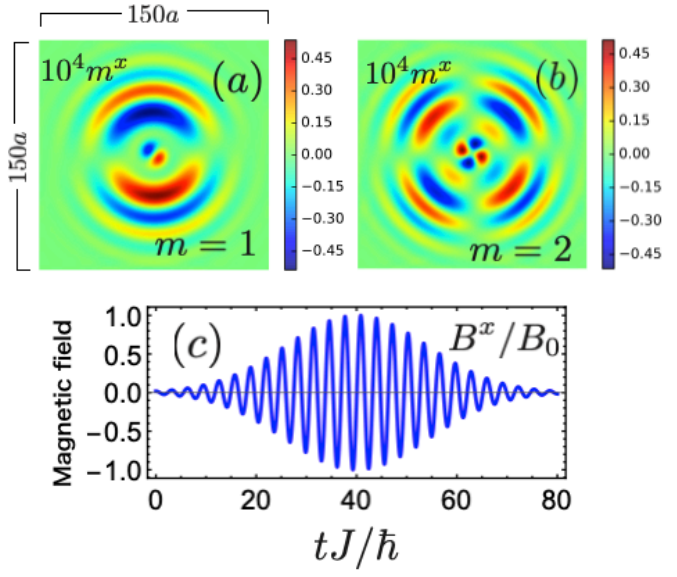

Figure 2.7: Multipolar spin wave radiation (a, b) induced by linearly polarized optical vortices with $\boldsymbol{e}_p = \hat{x}$ for $D = 0$, $H_z = 0.015$, $W = 7.5a$, $\omega = 2$, $\sigma = 20$, $t_0 = 40$, $B_0 = 0.05$, and $\alpha = 0.1$. We show the x-component of spins ($\times 10^4$) at $t = 80$ and the temporal profile of the magnetic field (c) for $m = 1$ at $\rho = w/\sqrt{2}$ and $\phi = 0$. The initial state at $t = 0$ is the ferromagnetic state ($m^z_{\boldsymbol{r}} = 1$ for all sites $\boldsymbol{r}$). For $J = 5$ meV, $\omega = 2$ corresponds to 2.4 THz and the beam amplitude $B_0 = 0.05$ does 4.3 Tesla.

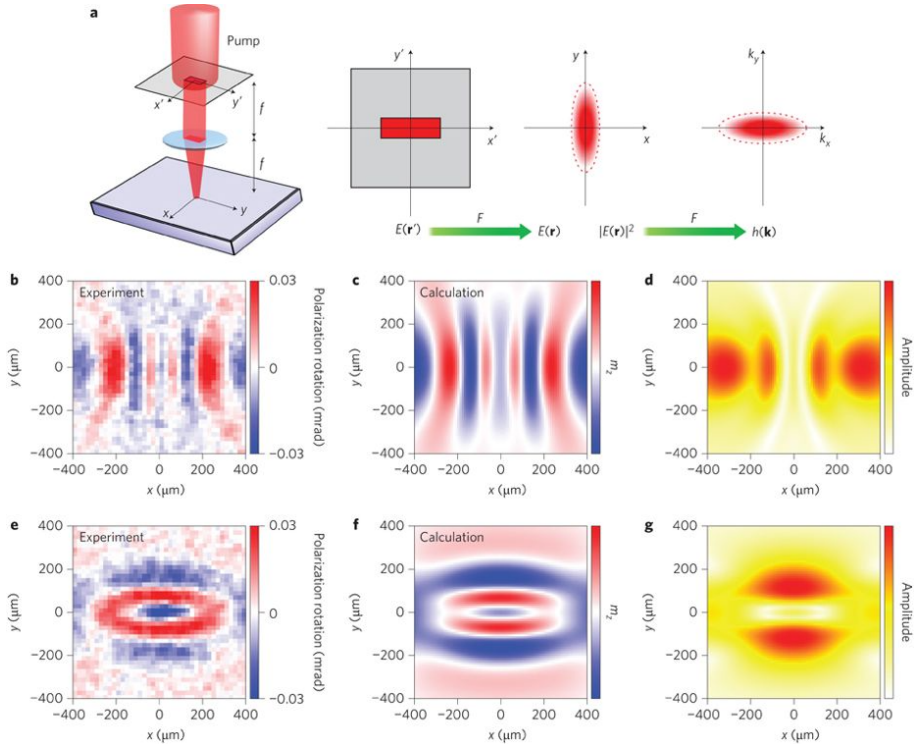

Figure 2.8: Optical excitation of anisotropic spin waves and their space-time resolved observation. A rectangular aperture is placed in front of the lens to generate an anisotropic beam spot for the excitation. *Note: Reprinted by permission from Springer Nature: Nature, "Directional control of spin-wave emission by spatially shaped light", T. Saitoh et al., Nature photonics,* **6**, *662 (2012) [95], copyright (2012).*

2.3 OAM selective generation of magnetic defects with OVs

As we repeatedly mention, the spatio-temporal scale of lights and matter differs very much in general. In the previous part, by focusing on the scale-free physics of magnets, i.e. spin waves, we avoided this problem. However, in order to exploit OVs for the control of chiral magnets, the discrepancy becomes essential.

2.3.1 Subwavelength focusing

Here we restate the problem which we are facing to. Our goal is to find a novel way of controlling magnetic properties of (chiral) magnets with OVs. In particular, we are to exploit the characteristic spatial profile of OVs for the optical generation of topological defects in chiral magnets such as skyrmions, skyrmioniums, and so on. However, while the size of (meta-) stable magnetic defects in chiral magnets is within the range of 10-1000 nm, the possible size of the beam spot of OVs is far larger since it is limited to the order of the wavelength because of the diffraction limit. In this subsection, we consider the direct coherent coupling of OVs and magnets so that the frequency should be around the typical timescale of the physics of magnets, i.e. GHz to THz. Even if the incident light is at THz, the possible beam waist will be around 100 μm. That is, there exists a large gap in the spatial scale of lights and topological defects, and we have to find a way to fill the gap. The key idea is provided by the emerging technology of the *subwavelength focusing* in the field of plasmonics [97].

Plasmonics is a field studying localized modes of lights on the surface of metals [98]. Due to the coupling between photons and conduction electrons, lights can be localized at the surface of metals. These localized lights provide a way of controlling lights in the scale much smaller than its wavelength. Plasmonics has been explored in a wide range of frequencies. In the visible and infrared regions, plasmonics plays an essential role for developing near-field microscopes and the tip-enhanced Raman scattering method used for the imaging and analysis of (biological) molecules [99]. In the microwave region, it plays the central role in the design of various metamaterials with unusual properties like negative refractive index [100].

Even in the THz region, it is becoming possible to achieve the control of lights in the subwavelength scale. In 2017, the subwavelength focusing of a THz OV [97] is experimentally demonstrated [101]. Although the plasmonics technology in the THz frequency is still very primitive, and the focusing

is not very tight at present (in the paper by Arikawa et al. the reduction of the beam size is limited to a factor of 3.4), the rapid developments in the THz optics impart the future realization of tight subwavelength focusing resolving the discrepancy in the spatial scale of lights and matter.

In this part, as a possible outcome of the tight subwavelength focusing of THz OVs, we consider the optical generation of topological defects in chiral magnets. In contrast to the simple ferromagnets treated in the previous subsection, chiral magnets have intrinsic chirality determined by the DM interaction coming from their noncentrosymmetric crystal structure. We will see that the competition between the chirality of the incident light and the intrinsic chirality of the material results in the OAM-dependent response which leads to the optical creation of topological defects in an OAM-dependent way. As chiral magnets are a prototypical system supporting multiferroicity, below we will consider both the Zeeman and multiferroic couplings as a way to couple OVs with spins.

2.3.2 Zeeman coupling

First we consider the Zeeman coupling between chiral magnets and the magnetic field component of the OVs. As we noted, here we assume a tight focusing of OVs beyond the diffraction limit and take the beam waist much smaller than the diffraction limit by hand. The model that we consider is the following one:

$$H = H_{\rm chi} - \sum_{\boldsymbol{r}} \boldsymbol{B}_{\boldsymbol{r}}(t) \cdot \boldsymbol{m}_{\boldsymbol{r}}. \tag{2.7}$$

Here $H_{\rm chi}$ is the model of a square-lattice chiral magnet (2.1). We use parameters corresponding to the skyrmion crystal phase: $D/J = 0.15, H^z/J = 0.015$ and take the initial state to be the meta-stable ferromagnetic one in the $+z$-direction. Since the phase transition between the ferromagnetic and skyrmion crystal phases is the first-order one, it is easy to prepare such a meta-stable state. As the ground state is a skyrmion crystal, this initial state is prone to form topological defects in response to the external perturbations. Our goal is to generate topological defects with OVs so that this meta-stable initial state seems to be a natural choice.

Gaussian beam

As a reference, we first consider Gaussian beams. We take a left-handed $\boldsymbol{e}_p = \hat{x} + i\hat{y}$. Gaussian beam of a frequency $\omega = 0.075J$. In Fig. 2.9,

we show the z-component of the magnetic moments driven by a half-cycle Gaussian beam pulse. Although the spin texture is partially inverted in the intermediate period, this transient magnetic defect vanishes eventually. In order for topological defects like skyrmions to be stabilized, the incident beam has to change the topological number of the spin texture. However, since the in-plane field configuration of the incident beam is spatially homogeneous for a half-cycle Gaussian beam pulse, it only induces a collective rotation of spins which is just a continuous deformation of the spin texture. Therefore, with the present beam parameters we cannot create topological defects through the Zeeman coupling with Gaussian beams.

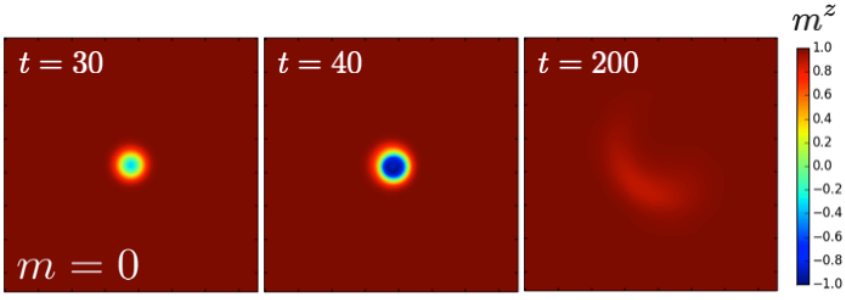

Figure 2.9: Application of Gaussian beam on the meta-stable ferromagnetic state of a 150×150 sites chiral magnets with parameters $D/J = 0.15$, $H^z/J = 0.015$, and $\alpha = 0.1$ with beam parameters ($\omega/J = 0.075$, $B_0/J = 0.15$, $w = 10a$, $\sigma = 10$, and $t_0 = 30$).

Optical vortices

We next switch to OVs. The temporal profile and the polarization of the beam are the same as the Gaussian beam. As Fig. 2.10 shows, in contrast to the Gaussian beam, the transient magnetic defects do not vanish, and we obtain different topological defects depending on the OAM of the OVs. The point-like defects (blue-colored region) are skyrmions and the ring-shaped one is a skyrmionium. We see that different OAMs result in the different number of created skyrmions. Since each skyrmion has a topological number of -1, the net topological number of the final state is found to be $\mathrm{sgn}(m)(m+1)$. Only when $m = -1$ we obtain a skyrmionium whose topological number is zero.

The OAM-dependent creation of topological defects could be phrased as an encoding of the OAM in the chiral magnets in the form of their

topological number. The explicit dependence on the sign of the OAM is a manifestation of the competition of the chiralities of the light and matter. Just as the spiral-shaped spin waves discussed in the previous part, the OAM-dependent in-plane field configuration of OVs induces a twist to the spin texture. In the presence of a DM interaction, the laser-induced twist competes with the intrinsic chirality of the target material. Therefore, the sign of OAM, which determines the direction of the induced twist, qualitatively changes the resulting topological defects.

After a sufficiently long period, the defects created by OVs in Fig. 2.10 relax to their equilibrium shape. Because of the repulsive interaction among defects, skyrmions in the cluster-like states in, for example, the panels of $m = \pm 5$ drift apart to form a collection of ordinary skyrmions.

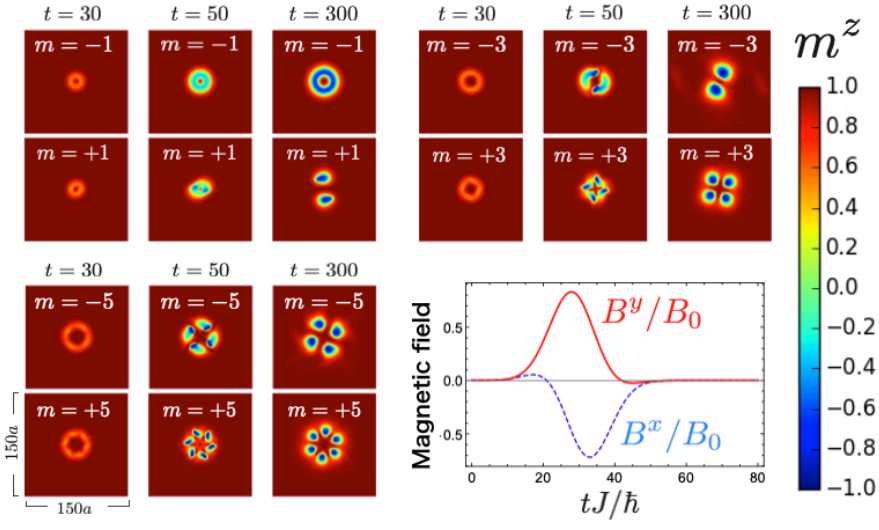

Figure 2.10: Generation of topological defects on the meta-stable ferromagnetic state of a 150×150 sites chiral magnets with parameters $D/J = 0.15$, $H^z/J = 0.015$, and $\alpha = 0.1$ by a half-cycle OV pulse ($\omega/J = 0.075$, $B_0/J = 0.15$, and $w = 10a$). Depending on the OAM of the beam m, we see different outcomes. The OV is assumed to be left-handed $\boldsymbol{e}_p = \hat{x} + i\hat{y}$, and its temporal profile is shown in the right-bottom panel. The color corresponds to the z-component of the magnetic moment at each site.

Contrary to the left-handed case, when the field polarization is right-handed $\boldsymbol{e}_p = \hat{x} - i\hat{y}$, OVs with the same parameters cannot generate any magnetic defects as shown in Fig. 2.11. The apparent difference between the right-handed and the left-handed OVs can be easily understood by moving into the rotating frame with the frequency ω where the incident beam looks static. In this frame, the magnetic field of OVs can be written

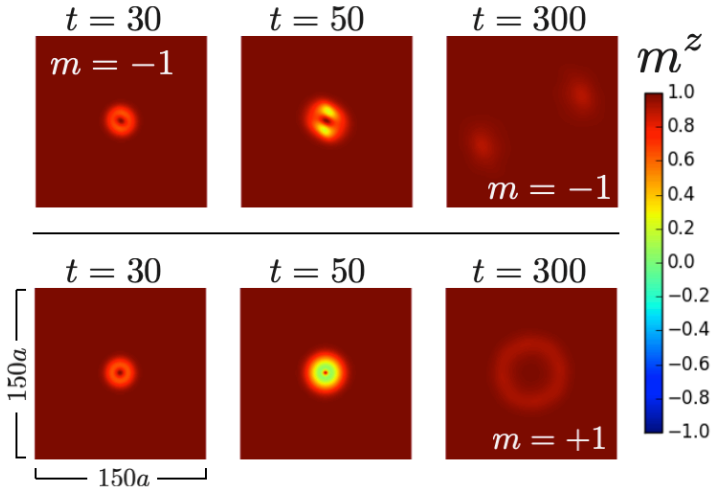

Figure 2.11: Irradiation of a right-handed magnetic field with $\boldsymbol{e}_p = \hat{x} - i\hat{y}$ and orbital angular momentum $m = \pm 1$. Time evolutions of the z component of spins for $H_z = 0.015$, $W = 10a$, $p = 0$, $\omega = 0.075$, $\sigma = 10$, $t_0 = 30$, $B_0 = 0.15$, $D = 0.15$, and $\alpha = 0.1$ are presented.

as a sum of the static in-plane field (with the spatial profile shown in Fig. 1.3) and the static field in the z-direction coming from the rotation. Depending on the polarization (either left-handed or right-handed), the rotation-induced field changes its sign. In the left-handed case, the field is in the $(-z)$-direction, and this works to lower the external field, making the initial state to be unstable to the formation of defects. On the other hand, the corresponding rotation-induced field for a right-handed field stabilizes the ferromagnetic initial state.

Timescale of the process

Let us examine the timescale of the process above. As we see in Fig. 2.10, the formation of defects complete within the time 300 $\hbar/J$, which corresponds to 10-100 ps for typical values of the exchange coupling. This short timescale could be important for skyrmionics. However, we have to remember that we are assuming an artificially strong sub-wavelength focusing in the present calculation.

As we mentioned previously, the beam waist should be comparable with the stable size of magnetic defects in the target. In reality, the sub-wavelength focusing cannot be so strong (at least near future) and therefore, we would work on materials hosting large skyrmions. The large stable size of skyrmions means that the DM interaction in such materials

is smaller than that assumed in Fig. 2.10. Because the stabilization of the twisted spin texture is due to the DM interaction, the smaller it is, the longer the timescale it takes for defects to relax to their stable shape. Therefore, to really address the timescale in the realistic situation, we have to study how the timescale depends on the magnitude of the DM interaction.

We calculate the time evolution of the cumulative skyrmion number (2.3) to study its dependence on the value of the DM interaction. The result is summarized in Fig. 2.12. We take the temporal profile of the beams to be the same as Fig. 2.10. We fix $JH_z/D^2 = 0.6$. For several values of the beam waist $W = 10a$, $30a$, $50a$ we calculated the cumulative skyrmion number for $m = \pm 1$. For each value of the beam waist, we change the strength of the DM interaction accordingly to match the beam waist and the stable size of defects.

We see that for the OAM of $m = +1$, which corresponds to the formation of a pair of skyrmions (see Fig. 2.10), as we make the beam waist (or the stable size of skyrmions) larger, it takes longer time for line-shape of the cumulative skyrmion number to reach the equilibrium one. In the intermediate time domain, the cumulative skyrmion number shows qualitatively different dependence on the distance from the center of the beam spot, depending on the value of the DM interaction. This indicates that the formation of skyrmions in this case is primarily driven by the DM interaction, and the timescale becomes longer for the a smaller DM interaction.

On the other hand, for $m = -1$ (corresponding to the formation of a skyrmionium), we see that even for a large beam waist, formation of the characteristic bump structure in the cumulative skyrmion number completes immediately after the irradiation. That is, the timescale of generating skyrmioniums with $m = -1$ OVs is essentially the same for OVs with the different beam waist.

For our choice of the DM vector, the optically induced perturbation by the $m = -1$ OVs is consistent with the spin texture of a skyrmionium: direction of the spin twist and the existence of the topological singularity. Hence, the DM interaction in this case only works to relax the "ready-made" spin texture. Therefore, even if we consider models with smaller DM interaction and use OVs with a larger (more realistic) beam waist, the advantage in the timescale would remain in this case.

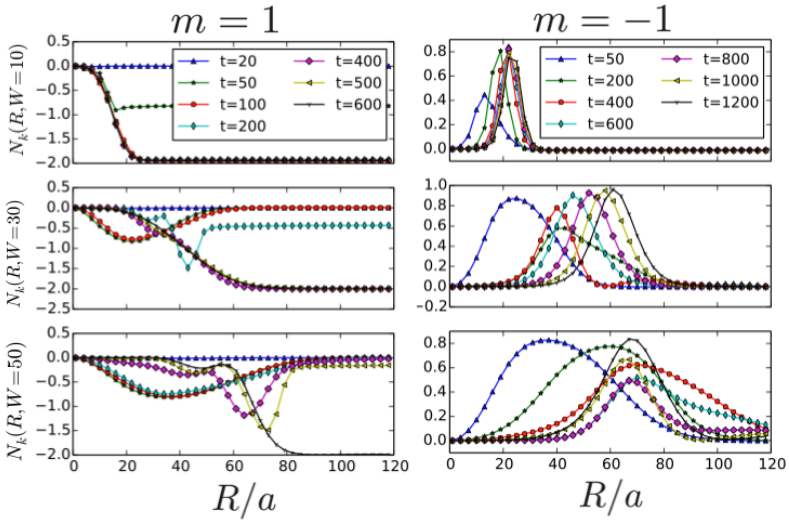

Figure 2.12: Time evolution of the cumulative skyrmion number for $m = \pm 1$ and $W = 10a$, $30a$, and $50a$. We fix $JH_z/D^2 = 0.6$ and take $D = 0.08\frac{50a}{W}$. For small D (large W), it takes longer time for the induced defects to relax to their equilibrium states. However, when $m = -1$, the characteristic bump structure of skyrmioniums is formed even right after the pulse is injected, regardless of the beam waist W (or the magnitude of D equivalently).

2.3.3 Magneto-electric coupling

So far, we have worked on the laser control of magnets with the magnetic field component of the OVs. In multiferroic materials, there exists a local electric polarization $\boldsymbol{p}$ written as a function of magnetic moments. Therefore, there is a possibility that we can do similar control of chiral magnets using electric field components of the beam through the ME coupling:

$$H_{\mathrm{ME}} = -\sum_{\boldsymbol{r}} \boldsymbol{p}_{\boldsymbol{r}} \cdot \boldsymbol{E}(\boldsymbol{r}), \tag{2.8}$$

where $\boldsymbol{p}_{\boldsymbol{r}}$ is the electric polarization which is a function of the magnetic moments $\{\boldsymbol{m}_{\boldsymbol{r}'}\}$ in multiferroics.

There are several different mechanisms of ME coupling. Here we discuss two of them: spin-current mechanism [85] and p-d hybridization [84, 88]. The former gives the electric polarization: $\boldsymbol{p}(\boldsymbol{r}_{i,i+1}) \propto \boldsymbol{e}_{i,i+1} \times (\boldsymbol{m}_{\boldsymbol{r}_i} \times \boldsymbol{m}_{\boldsymbol{r}_{i+1}})$, where $\boldsymbol{e}_{i,i+1}$ is the unit vector pointing from site $\boldsymbol{r}_i$ to site $\boldsymbol{r}_{i+1}$. A non-vanishing electric polarization from this mechanism needs a canted magnetic structure. Hence, even if the coupling between spins and the electric field is large, as long as we are considering of smooth magnetic structures (e.g. spin waves and skyrmions), the ME coupling is effectively weakened, and we could ignore that. On the other hand, ME coupling from the p-d hybridization mechanism could be important. In Cu_2OSeO_3, for example, the electric polarization comes from this mechanism and is written as $\boldsymbol{p}(\boldsymbol{r}) = \lambda(m^y_{\boldsymbol{r}} m^z_{\boldsymbol{r}}, m^z_{\boldsymbol{r}} m^x_{\boldsymbol{r}}, m^x_{\boldsymbol{r}} m^y_{\boldsymbol{r}})$ with $\lambda = 5.64 \times 10^{-33}$ Cm [88, 102], if we take the c-axis to be the z-axis.

Substituting the polarization vector $\boldsymbol{p}(\boldsymbol{r}) = \lambda(m^y_{\boldsymbol{r}} m^z_{\boldsymbol{r}}, m^z_{\boldsymbol{r}} m^x_{\boldsymbol{r}}, m^x_{\boldsymbol{r}} m^y_{\boldsymbol{r}})$ into the Hamiltonian H_{ME} and differentiate it by $-\boldsymbol{m}_{\boldsymbol{r}}$, we can obtain the effective magnetic field which enters in the LLG equation;

$$\boldsymbol{H}^{\mathrm{ME}}_{\mathrm{eff}} = \lambda \left(E^y m^z_{\boldsymbol{r}}, E^x m^z_{\boldsymbol{r}}, E^x m^y_{\boldsymbol{r}} + E^y m^x_{\boldsymbol{r}} \right). \tag{2.9}$$

If we consider a ferromagnetic initial state with $\boldsymbol{m}_{\boldsymbol{r}} = \hat{z}$, Eq. (2.9) is equivalent to the Zeeman coupling with a magnetic field $\boldsymbol{B} = \lambda(E^y, E^x, 0)$. Therefore, we can expect that even for the ME coupling, we will observe qualitatively the same results as those obtained for the Zeeman coupling.

The model that we consider is as follows:

$$H = H_{\mathrm{chi}} + H_{\mathrm{ME}}. \tag{2.10}$$

We consider the right-handed OVs with $\boldsymbol{e}_p = \hat{x} - i\hat{y}$. The ME coupling is taken to be of the p-d hybridization [Eq. (2.9)]. Figure 2.13 shows the

time evolution of the model (2.10) for $D = 0.15$, $H_z = 0.015$, and $\alpha = 0.1$ under the electric field of an OV with $W = 10a$, $p = 0$, $\omega = 0.075$, $\sigma = 10$, $t_0 = 30$, and $E_0\lambda = 0.25$. We note that the functional form of the electric field of OVs is the same as that of the magnetic field. If we take $J \sim 1$ meV and $\lambda \sim 10^{-32}$ Cm, the electric field strength we assumed corresponds to 40 MV/ cm.

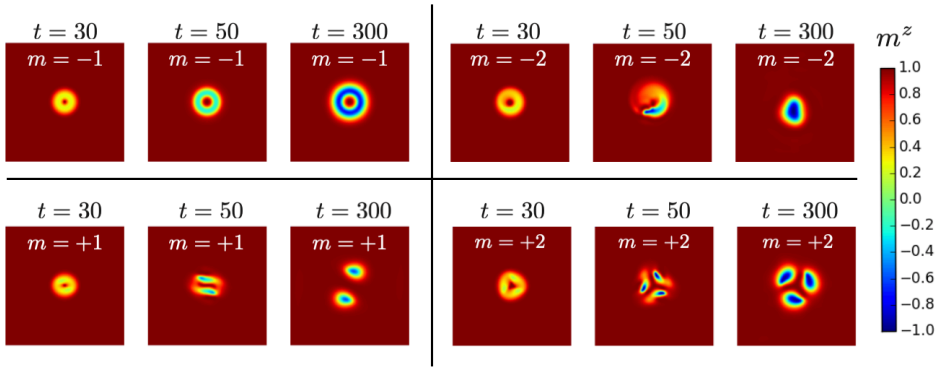

Figure 2.13: Orbital angular momentum dependence of the creation of topological defects with the electric field component of optical vortices through the magneto-electric coupling. The fields are assumed to be right-handed $\boldsymbol{e}_p = \hat{x} - i\hat{y}$. We show the time evolution of magnetic moments of the model (2.10) with $D = 0.15$, $H_z = 0.015$, $W = 10a$, $p = 0$, $\omega = 0.075$, $\sigma = 10$, $t_0 = 30$, $E_0\lambda = 0.25$, and $\alpha = 0.1$. The system is periodic in both x and y directions, and its size is 150 sites in both directions.

As is shown in Fig. 2.13, the outcome is qualitatively the same as the Zeeman coupling. We obtain topological defects depending on the OAM of the incident OVs. The main difference between the Zeeman and ME couplings is the polarization of the incident beams. In the former case left-handed beams were advisable for the creation while in the latter, right-handed ones are better. As we discussed, the ME coupling in the present case is, at least for the initial state, equivalent to the Zeeman coupling with a magnetic field $\boldsymbol{B} = \lambda(E^y, E^x, 0)$. Therefore, right-handed electric fields work as left-handed (effective) Zeeman fields, being suitable for creating defects.

Electric-field control through the ME coupling also applies to the spin wave shaping discussed in the previous section. We can show that qualitatively the same phenomena (multipolar and spiral spin waves) can be realized with the ME coupling between OVs and magnetic moments in (non-chiral) magnets [62].

2.4 Thermal generation of magnetic defects with OVs

In this section, we consider an incoherent coupling between spins and lights. As we noted, in order to adapt the wavelength of OVs to the typical size of magnetic defects in chiral magnets, the corresponding frequency reaches to (sub-) PHz region and is too high to induce any coherent dynamics of spins. Instead, OVs create hot electrons and excite high-energy lattice vibrations which (locally) equilibrate within 100 fs to 1 ps [28].

In this section, we consider OVs as a source of heating whose intensity determines the local temperature profile. We assume that OVs simply induce a temperature distribution proportional to the local beam intensity: $T(\boldsymbol{r}) \propto |u^{LG}(\rho, \phi, 0)|^2$ and see whether the heating can generate magnetic defects in chiral magnets.

As is theoretically shown by Koshibae and Nagaosa [103], for chiral FMs, local heating with a disk-shaped profile can generate skyrmions. What we expect is, therefore, that we can extend their result to the annular temperature profile realized with OVs and examine whether we can use OVs for nucleating general $n\pi$-vortices in chiral magnets.

2.4.1 Laser control of local temperature

Firstly, let us be sure that we can indeed control the temperature profile using lasers. Although we are to model the temperature profile as $T(\boldsymbol{r}) \propto |u^{LG}(\rho, \phi, 0)|^2$, the actual temperature profile should be obtained by solving the heat equation.

In order to validate the assumption on the temperature profile, below we examine the spatio-tempral profile of a laser-heated system. For simplicity, we consider the following one-dimensional heat equation:

$$\frac{\partial T(x,t)}{\partial t} - \alpha \frac{\partial^2 T(x,t)}{\partial x^2} = -\frac{T(x,t) - T^0(x,t)}{\tau}, \tag{2.11}$$

where α is the diffusion rate of the system and τ is the relaxation rate to the equilibrium. In metals, α is around 10^{-4} and in insulators around 10^{-6} [104]. The timescale of the cooling τ is determined by the energy scale of the coupling between the electron and phonon systems, so that it should be shorter than 10 ps. At each time, the temperature approaches the enviroment temperature $T^0(x,t)$ determined by the applied laser and the background cooling.

We assume that the overall system is in contact with a thermal bath

at the liquid Helium temperature $T_{\mathrm{He}} = 4.2$ K. On top of this background cooling, there exists the heating induced by the laser. As a whole, the instantaneous temperature of the environment $T^0(x,t)$ is set to be

$$T^0(x,t) = T_{\mathrm{He}} + T_b \frac{x^2}{w^2} e^{-\frac{x^2}{w^2}} \left(1 - \frac{t}{100}\right), \tag{2.12}$$

where T_b is a constant determined by the intensity of the laser. Here, we assume that incident OV is gradually weaken down to zero. We measure the time in the unit of ps.

We take the following parameters for the simulation: $\alpha = 10^{-5}$, $\tau = 5$ ps, $T_b = 50$ K. We discretize the system into a lattice with the lattice constant of 1 nm and take $w = 50$ nm. In Fig. 2.14, we show that the temperature profile follows that of the heating. We see that after switching on the heating, the system starts to follow the environment temperature $T^0(x,t)$ shortly after the initial time-domain. Therefore, as long as the timescale of the process we are interested in is sufficiently longer than the period of this initial time-domain determined by τ, assuming the spatio-temporal profile proportional to the laser profile is acceptable.

2.4.2 Stochastic LLG equation

We numerically calculate the time-evolution of laser-heated spin systems. In order to do that, we have to take into account the effect of thermal fluctuation. Among various possible ways, here we introduce the fluctuation as a random noise $\boldsymbol{\xi}_{\boldsymbol{r}}(t)$ in the effective magnetic field $\boldsymbol{H}_{\mathrm{eff}}$:

$$\frac{d\boldsymbol{M}_{\boldsymbol{r}}}{dt} = -\gamma \boldsymbol{M}_{\boldsymbol{r}} \times \left(-\frac{\partial H(\boldsymbol{M}_{\boldsymbol{r}_1}, ..., \boldsymbol{M}_{\boldsymbol{r}_N})}{\partial \boldsymbol{M}_{\boldsymbol{r}}} + \boldsymbol{\xi}_{\boldsymbol{r}}(t) \right) + \alpha \frac{\boldsymbol{M}_{\boldsymbol{r}}}{|\boldsymbol{M}_{\boldsymbol{r}}|} \times \frac{d\boldsymbol{M}_{\boldsymbol{r}}}{dt}, \tag{2.13}$$

where $\xi^{\mu}_{\boldsymbol{r}}(t)$ is the μ ($\mu = x, y$) component of a Gaussian white noise on the site $\boldsymbol{r}$ satisfying

$$\begin{aligned} \langle \xi^{\mu}_{\boldsymbol{r}}(t) \rangle &= 0, \\ \langle \xi^{\mu}_{\boldsymbol{r}}(t) \xi^{\nu}_{\boldsymbol{r'}}(t') \rangle &= 2D_{\boldsymbol{r}} \delta^{\mu,\nu} \delta(\boldsymbol{r} - \boldsymbol{r'}) \delta(t - t'). \end{aligned} \tag{2.14}$$

This formulation is called the stochastic LLG (sLLG) equation [103, 105, 106]. The sLLG equation is a powerful tool for studying thermally induced dynamics of spin systems as it allows us to calculate the real-time dynamics of many-body system at finite temperature. For example, by using this

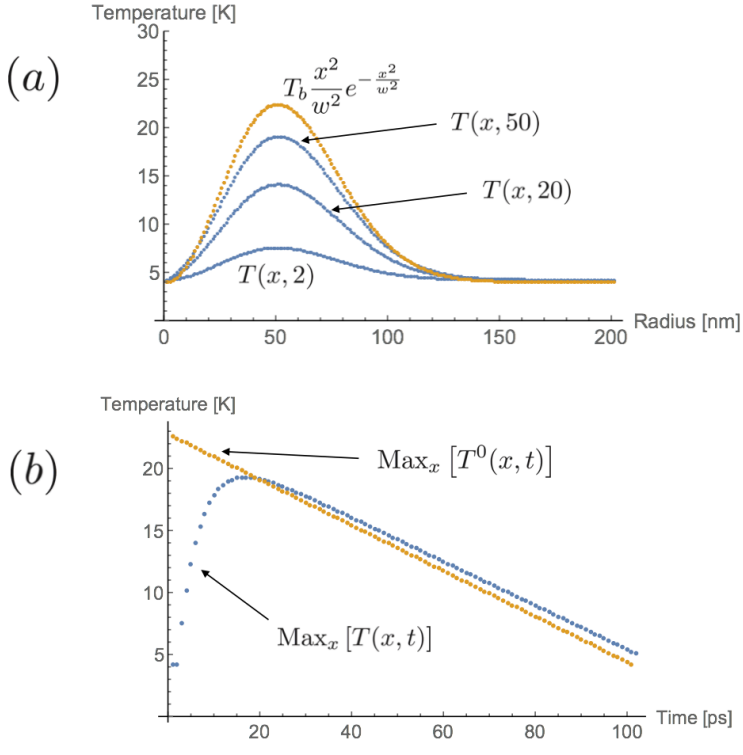

Figure 2.14: (a) Spatio-temporal profile of the temperature in the laser heated system obtained by solving the heat equation (2.11) assuming (2.12). (b) Maximum values of $T(x,t)$ and $T^0(x,t)$ at each time.

sLLG equation, Mochizuki et al. [107] have shown that the experimentally observed ratchet motion of a skyrmion lattice is due to the thermal gradient.

The random field $\boldsymbol{\xi}_{\boldsymbol{r}}(t)$ is tied to the local temperature distribution $T(\boldsymbol{r})$ through the fluctuation-dissipation theorem. In order for the random field to mimic the thermal fluctuation at temperature T, the distribution function $P(\boldsymbol{M}_{\boldsymbol{r}_1}, ..., \boldsymbol{M}_{\boldsymbol{r}_N}, \boldsymbol{r}, t)$ obtained by the Focker-Plank equation corresponding to the sLLG equation must satisfy the condition [106]

$$\begin{aligned} &P(\boldsymbol{M}_{\boldsymbol{r}_1}, ..., \boldsymbol{M}_{\boldsymbol{r}_N}, \boldsymbol{r})_{\mathrm{eq}} \\ &= P(\boldsymbol{M}_{\boldsymbol{r}_1}, ..., \boldsymbol{M}_{\boldsymbol{r}_N}, \boldsymbol{r}, t \to \infty) \propto \exp\left[-\beta(\boldsymbol{r}) H(\boldsymbol{M}_{\boldsymbol{r}_1}, ..., \boldsymbol{M}_{\boldsymbol{r}_N})\right]. \end{aligned} \tag{2.15}$$

Namely, the asymptotic distribution should locally coincide with the canonical distribution at the inverse temperature $\beta(\boldsymbol{r}) = 1/[k_B T(\boldsymbol{r})]$. We can confirm that, to meet this condition, we have to set

$$D_{\boldsymbol{r}} = k_B T(\boldsymbol{r}) \alpha / (\gamma^2 \hbar). \tag{2.16}$$

2.4.3 Chiral ferromagnets

By using this sLLG equation for the temperature profile determined by OVs $T(\boldsymbol{r}) \propto |u^{LG}(\rho, \phi, 0)|^2$, we calculate the dynamics of a chiral FM (3.1). We mostly use the following parameters: $J = 1$, $D = 0.15$, and $\alpha = 0.1$. For these values of J and D, the phase boundary between the helical order phase and the skyrmion crystal phase is $H^z = 0.0052$ and that between the skyrmion crystal and the ferromagnetic phase is $H^z = 0.018$. The value of the static field H^z is chosen as the ground state is in the skyrmion crystal phase. Same as the previous case, we consider the meta-stable ferromagnetic state as the initial state of our calculation. For the numerical integration of the sLLG equation in terms of the Stratonovich stochastic differential equation, below we use the stochastic generalization of the Heun method [105] with a numerical time step of $\Delta t = 0.02$.

As the temporal profile of the temperature, we use the following "annealing" like one $T(t) = T_0 \left(1 - \frac{t}{t_0}\right) \Theta(t)\Theta(t_0 - t)$. Here $\Theta(x)$ is the Heaviside theta function. That is, we assume that the temperature is instantaneously raised to its maximum (T_0) and gradually cooled down (see also Fig. 2.14). This can be achieved by gradually lowering the laser intensity as discussed in Sec. 2.4.1. Since the spatial profile is set to be of the beam-induced one, the spatio-tempral profile of the temperature is given as $T(t, \boldsymbol{r}) = T(t) \left[|u^{LG}(\rho, \phi, 0)|^2 / \max_{\boldsymbol{r}}(|u^{LG}(\rho, \phi, 0)|^2) \right]$.

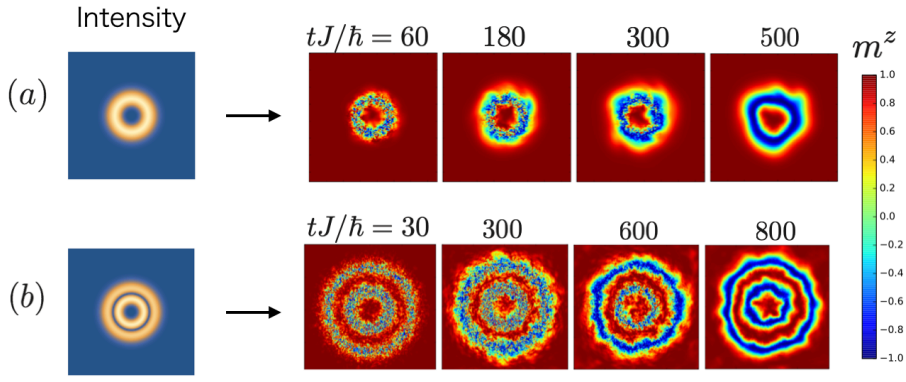

Figure 2.15: The creation of topological defects with the local heating using OVs. In the left-hand side, we show the time-averaged intensity profile (and the temperature profile assumed) of the incident beam. The right-hand side is the time-evolution of the z component of spins for each case. (a): Nucleation of a skyrmionium by the local heating with a single-ring OV ($p = 0$, $m = 5$, and $w = 12.5a$). (b): Nucleation of a 4π defect with an OV ($p = 1$, $m = 3$, and $w = 33.3a$). In each case, the initial state is taken to be the meta-stable ferromagnetic state in the z-direction. We fix the Gilbert damping constant to be $\alpha = 0.1$. For (a) we take $H^z = 0.01$, $T_0/J = 2$, and $t_0 = 500\hbar/J$ while for (b) we use $H^z = 0.011$, $T_0/J = 4$, and $t_0 = 800\hbar/J$.

When the beam waist is small, the result is essentially the same as the local heating with Gaussian beams, and the results by Koshibae et al. [103] is reproduced. On the other hand, when the beam waist is compatible with the stable size of magnetic defects, as we see in Fig. 2.15, the spatial profile of the beam is "printed" as topological defects. Depending on the radial index p, determining the number of rings in the intensity profile, we obtain $n\pi$-vortices with $n = p + 1$. As we noted previously, those $n\pi$-vortices are meta-stable once formed. Therefore, the local heating with OVs could be a systematic way of generating a family of skyrmionic defects.

However, in order the local heating to be a practical scheme of generating those defects, we have to check the reliability or stability of this approach. Since our method relies on the nucleation of defects by the thermal fluctuations induced by OVs, whether the defects are successfully generated or not is even theoretically nondeterministic. Below, we numerically study how reliable the local heating is as a nucleation scheme.

We fix the temporal profile of the heating in the annealing type as before and take the parameters: $p = 0$, $m = 5$. That is, we examine the creation of a ring-shaped defect, skyrmionium with OVs. While changing the strength of the heating, the external static magnetic field, and beam waist, we calculate the success probability of obtaining a skyrmionium after the heating procedure. We perform the numerical simulations twenty times for each set of parameters and obtain the probability of having a skyrmionium.

The result is summarized in Fig. 2.16 [in (d) we show the temporal profile of the temperature]. We see that when the heating is sufficiently strong (of the order of the exchange coupling) and the beam waist is comparable with the stable size of the target defect, we can generate a skyrmionium with high probability of success. Since the high probability is achieved in a wide parameter region, this approach is expected to be robust against slight changes in material parameters, beam parameters, temperature profiles, and so on. Therefore, the local heating with OVs would be a reliable and practical way of generating topological defects in chiral magnets.

So far we have been working on chiral FMs. However, the applicability of our method is not limited to it. Indeed, the important feature of the local heating is that it does not depend on the details of the system. It does not require the system to be insulating or metallic and not need a specific form of DM interactions. To show the wide applicability of our method, let us consider chiral antiferromagnets next.

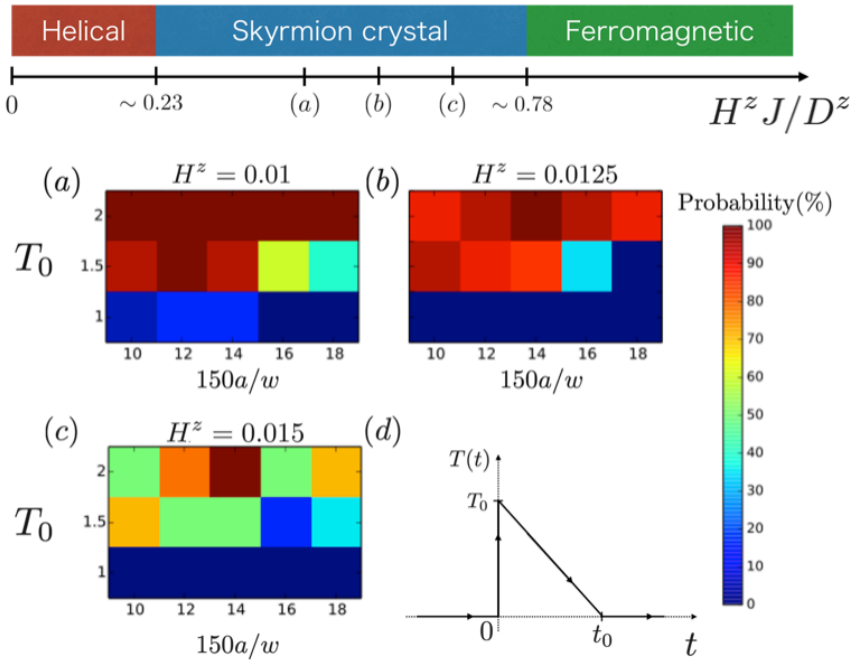

Figure 2.16: Success probability of creating skyrmioniums by vortex beams with $p = 0$ and $m = 5$, for $J = 1$, $D = 0.15$, and $\alpha = 0.1$. (a) Probability for $H^z = 0.01$, (b) $H^z = 0.0125$, and (c) $H^z = 0.015$. The local temperature $T(t, \boldsymbol{r})$ is set to be proportional to the intensity of the beam: $T(t, \boldsymbol{r}) = T(t)\left(|u^{LG}(\rho, \phi, 0)|^2 / \max(|u^{LG}(\rho, \phi, 0)|^2)\right)$. Here the temporal profile of the temperatures is given as panel (d): $T(t) = T_0\left(1 - \frac{t}{t_0}\right)\Theta(t)\Theta(t_0 - t)$ with $t_0 = 500$. The highest probability is achieved when the magnetic field is small and the beam waist satisfies $w \sim 11.5a$ for which the wavelength of the beam is comparable with the size of skyrmions. We also show where the chosen magnetic fields H^z locate in the phase diagram.

2.4.4 Chiral antiferromagnets

Chiral antiferromagnets are also expected to host skyrmion-like defects. As a simple theoretical model, we consider a square lattice antiferromagnets with a DM interaction. Unlike the ferromagnetic case, we cannot use a Zeeman field to stabilize magnetic defects so that we rely on a magnetic anisotropy:

$$H_{AF} = J \sum_{\boldsymbol{r}} \boldsymbol{m}_{\boldsymbol{r}} \cdot \left(\boldsymbol{m}_{\boldsymbol{r}+a\boldsymbol{e}_x} + \boldsymbol{m}_{\boldsymbol{r}+a\boldsymbol{e}_y} \right) + \sum_{\boldsymbol{r}} \boldsymbol{D}_i \cdot (\boldsymbol{m}_{\boldsymbol{r}} \times \boldsymbol{m}_{\boldsymbol{r}+a\boldsymbol{e}_i}) - A \sum_{\boldsymbol{r}} (m^z_{\boldsymbol{r}})^2. \tag{2.17}$$

Here the exchange coupling is antiferromagnetic $J > 0$, and A is the uniaxial magnetic anisotropy. Due to the DM interaction, for example, $\boldsymbol{D}_x = D\boldsymbol{e}_y$, $\boldsymbol{D}_y = -D\boldsymbol{e}_x$, a Néel-type antiferromagnetic skyrmion (and skyrmionium) [shown in Fig. 2.17(a, b)] is stabilized with appropriate parameters.

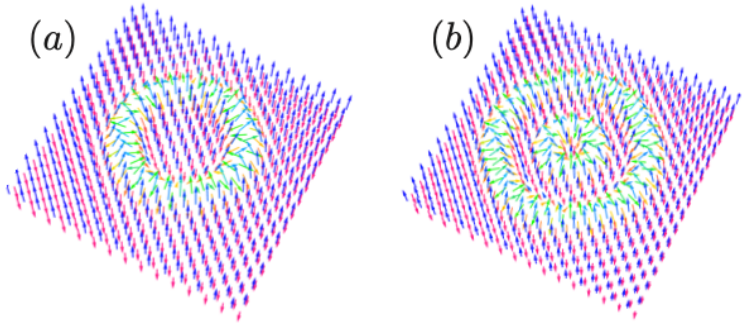

Figure 2.17: Schematics of a Néel-type antiferromagnetic (a) skyrmion and (b) skyrmionium. There are two magnetic sublattices in Néel ordered states in the square lattice, and a skyrmion and skyrmionium can be seen as bound states of their ferromagnetic counterparts living in different magnetic sublattices.

The phase diagram of this model for $A/J = 0.055$ [108] is given in Fig. 2.18. For $D/J < 0.22$, the ground state is a Néel state. However, antiferromagnetic skyrmions are (meta-)stable only if $D/J > 0.16$. Following Ref. [108], we particularly call this region as antiferromagnetic skyrmion (AFMS) region. For larger DM interaction satisfying $D/J > 0.22$, skyrmions deform (d-AFMS region) and form warm domains (WD region). In upper panels of Fig. 2.18 we show typical spin textures of AFMs and WD regions using staggered spins $m^z_{\boldsymbol{r},\pm} \equiv m^z_{\boldsymbol{r}=(i,j)} \times (-1)^{i+j}$. We note

that WDs can be regarded as a collection of strongly deformed skyrmions so that the boundary between the d-AFMS and WD regions is unclear from our LLG calculation.

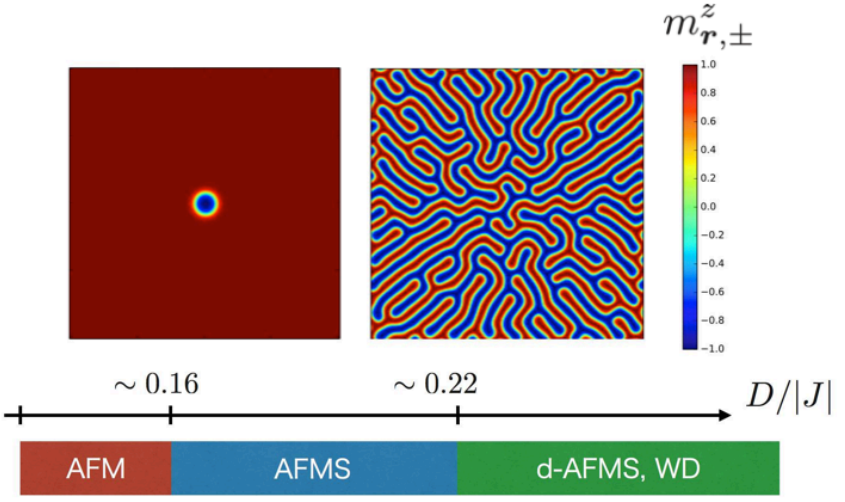

Figure 2.18: Phase diagram of the canonical model of chiral AFMs Eq. (2.17) for $A/J = 0.055$ reproduced from Ref. [108]. When DM interaction is very weak, we have an antiferromagnetic (AFM) region where we cannot have skyrmions. As we increase DM interaction D, antiferromagnetic skyrmions become energetically stable at $D/J \sim 0.16$ as isolated defects. For larger DM interaction ($D/J \geq 0.22$), skyrmions deform to lower their energy (d-AFM state) and eventually warm domains are formed (WD). The phase boundary between d-AFM and WD is unclear from our calculations. We visualize the spin textures of typical states in the AFMS and d-AFMS phases obtained from LLG calculations by using staggered spins $m^z_{\boldsymbol{r},\pm} \equiv m^z_{\boldsymbol{r}=(i,j)} \times (-1)^{i+j}$.

As in the ferromagnetic case, we model the effect of OVs as a local heating and examine the time evolution of spins with the sLLG equation. Our goal is to show that local heating with OVs offers a practical way of generating antiferromagnetic skyrmioniums. As we see from Fig. 2.17(b), the spin texture of an antiferromagnetic skyrmionium consists of two skyrmioniums living in the different sublattices.

Because the two possible Néel states are energetically degenerate, having magnetic defects costs energy proportional to the perimeter, not the area of them. This makes magnetic defects have lower energy than those in ferromagnets, allowing them to easily deform and split. Because of that, it is more difficult to control the formation of defects compared with fer-

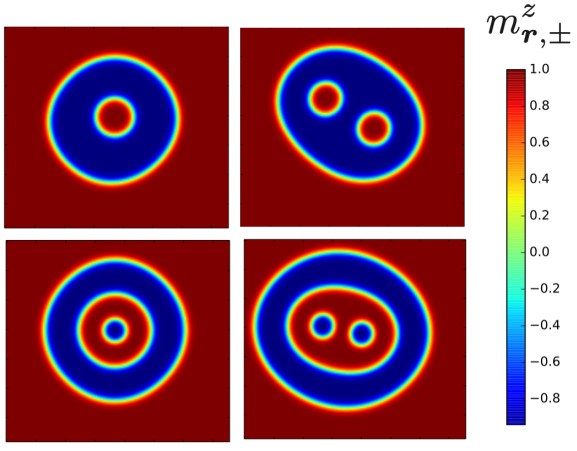

Figure 2.19: Examples of magnetic defects generated with heating by single-ring OVs. The upper-left panel is the ordinary antiferromagnetic skyrmionium, and the lower-left one corresponds to antiferromagnetic 3π vortex.

romagnets. Even if we apply a single-ring ($p = 0$) OV, heating caused by that can result in a variety of defects (see Fig. 2.4.4), though they have a ring-like structure in common. In the following, we call those ring-shaped defects as vortex defects altogether.

We will solve the sLLG equation for the antiferromagnetic Hamiltonian (2.17):

$$\frac{d\boldsymbol{M}_{\boldsymbol{r}}}{dt} = -\gamma \boldsymbol{M}_{\boldsymbol{r}} \times \left(-\frac{\partial H_{AF}}{\partial \boldsymbol{M}_{\boldsymbol{r}}} + \boldsymbol{h}_{T(\boldsymbol{r})}(t) \right) + \frac{\alpha}{M} \boldsymbol{M}_{\boldsymbol{r}} \times \frac{d\boldsymbol{M}_{\boldsymbol{r}}}{dt}, \tag{2.18}$$

where $\boldsymbol{M}_{\boldsymbol{r}} = \hbar\gamma \boldsymbol{m}_{\boldsymbol{r}}$, and $\boldsymbol{h}_{T(\boldsymbol{r})}(t)$ is again the random field satisfying Eq. (2.14) and $\sigma(\boldsymbol{r}) = 2k_B T(\boldsymbol{r})\alpha$. We take a system with 150×150 sites with periodic boundaries. The numerical time step is set to be $\Delta t = 0.03$. Hereafter we take $J = 1$ and fix $D = 0.205$ and $A = 0.055$. Those parameter values correspond to the AFMS ground state. Namely, here we are taking an actual ground state of the model as the initial state.

After some trials and errors, we noticed that to keep heating the system for a long period is advantageous. Therefore, in the following, we assume the following temporal profile of the temperature $T(t) = T_0 \Theta(t_0 - t)\Theta(t)$ with $t_0 = 3000, 5000$, and 7000. Here T_0 is proportional to the time-averaged intensity of an OV with $p = 0$ and $m = 5$. We show a typical time evolution under this temperature profile in Fig. 2.20. Under the static

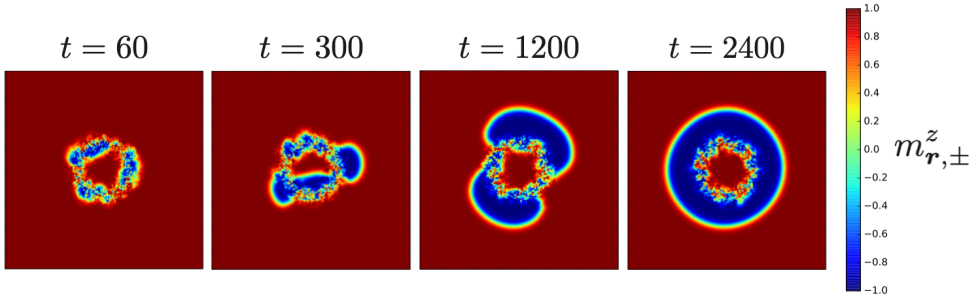

Figure 2.20: Time evolution of staggered spins in a particular trial with parameters $D/J = 0.205, A/J = 0.055, T_0/J = 1$, $w = 12.5a$, and $\alpha = 0.1$. The ring-shaped heating caused by OVs with $p = 0$ and $m = 5$ creates magnetic domains on the background Néel order.

heating, magnetic domains on the background Néel state appear and merge to form an antiferromagnetic skyrmionium.

As is done for the ferromagnetic case, let us examine the probability of success in generating defects. As we noted, in the antiferromagnetic case, we encounter various vortex defects as shown in Fig. 2.4.4. Instead of sticking to an antiferromagnetic skyrmionium, here we study the probability of getting general vortex defects. We try calculations twenty times for each set of (T_0, t_0, w) and see whether we have one of such ring-shaped defects or not.

The result is summarized in Fig. 2.21. We find that with proper beam waist and heating strength, the probability can be very high. Hence, heating with OVs can be a reliable way of nucleating vortex defects in chiral antiferromagnets. The optimal beam waist is comparable with the stable size of skyrmions which is determined by the balance among exchange coupling, DM interaction, and anisotropy.

2.4.5 Remarks

As we noted previously, OVs can be conveniently generated with the spiral phase plates, holograms, synchrotrons, and so on. In the wide range of frequencies covering the range of the typical size of skyrmions, OVs are available. Heating with OVs is a very simple scheme as a way of creating defects. Compared to other proposed methods like the spin-current injection, it is more widely applicable. We can create various types of defects just by changing beam parameters. It applies to both ferromagnets and antiferromagnets as we have shown, and does not require the target to be

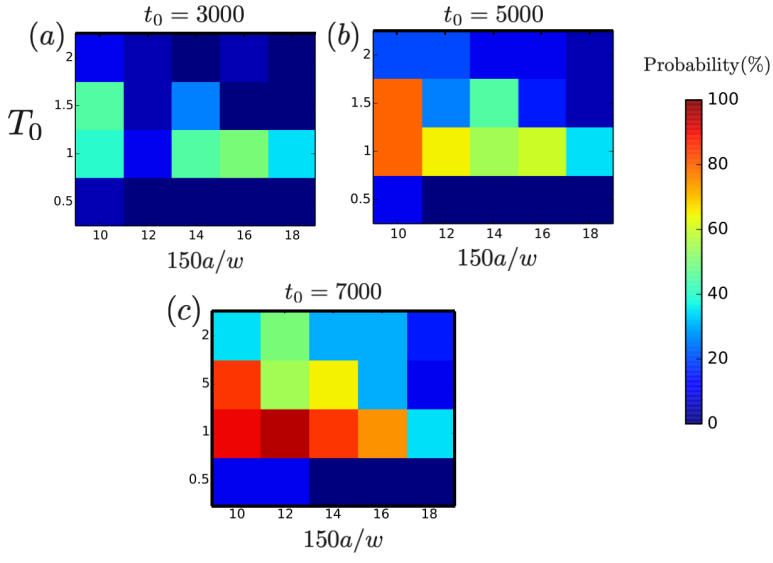

Figure 2.21: Success probability of creating antiferromagnetic vortex defects by vortex beams with $p = 0$ and $m = 5$. We fix $J = 1$, $D = 0.205$, $A = 0.055$, and $\alpha = 0.1$, with which the system is in the AFMS region (see Fig. 2.18). The initial state at $t = 0$ is a Néel ordered ground state and the temperature is varied in accord with $T(t) = T_0\Theta(t_0 - t)\Theta(t)$ for (a) $t_0 = 3000$, (b) $t_0 = 5000$, and (c) $t_0 = 7000$. The probability is high when the wavelength of OVs is of the same order of the size of antiferromagnetic skyrmions, and the period of the irradiation of vortex beams is long.

metallic unlike the injection of spin-polarized current.

Heating with OVs is unique in that it allows us to systematically generate $n\pi$ vortices in chiral magnets. In considering applications of skyrmionic defects for information processing, the increased number of possible defects has a substantial impact. In skyrmion-based memories, information will be encoded as presence/absence of a skyrmion. That is, if the number of memory units is N, the amount of information stored scales as 2^N. On the other hand, if a skyrmionium and a 4π vortex are available in addition to skyrmions, the scaling improves to 4^N. Namely, increasing the number of available magnetic defects exponentially increases the recording density of the memory.

2.5 Summary of Chapter 2

In this chapter, we discussed ultrafast magnetism with OVs. We reviewed chiral magnets and their topological magnetic defects. We pointed out the problem of the deviation in the spatio-temporal scales of lights and magnets and enumerated three possible ways to overcome it. We showed that OAM carried by OVs results in the characteristic spatial profile and chiral time evolution of electromagnetic fields, enabling us to control spin waves in an unconventional way. We found that if tight subwavelength focusing of OVs at THz frequency becomes possible, we can optically generate topological defects in chiral magnets with systematic OAM dependence. Finally, we demonstrated that heating with OVs allows us to systematically generate a family of topological defects; skyrmion, skyrmionium, 4π vortex, and so on, without relying on the materials details.

Chapter 3

Cylindrical vector beams (CVBs)

In this chapter, we discuss how to exploit the unique spatial and the focusing properties of CVBs for the use of optical physics. In the first section we propose a nonequilibrium extension of the magnetic oscillation measurements, which allows us to measure the Fermi surface profile of magnetic materials. In the next section, we discuss how to use CVBs for the spectroscopy of matters and control of their electromagnetic properties. We study how much the electric-field absorption can be suppressed by using the focused CVBs instead of Gaussian beams and give applications for magnetic-field spectroscopy. We also propose to use the azimuthal profile of the electric-field component of the azimuthal CVBs for the imaging and control of the circulating edge current in topological insulators. Moreover, we claim that CVBs can be a powerful tool of designing nonequilibrium states of driven matters through the Floquet engineering approach. This chapter is based on Refs. [63, 64].

3.1 Nonequilibrium magnetic oscillation with azimuthal CVBs

In this section, we propose a nonequilibrium extension of magnetic oscillation measurements of Fermi surfaces using CVBs. This new method enables us to probe the full three-dimensional (3D) profile of Fermi-surfaces of magnetic metals.

3.1.1 Magnetic oscillation: probe of Fermi surfaces

When electric conductors are placed under a strong magnetic field, the cyclotron motion of electrons results in the formation of Landau levels and Landau tubes in the momentum space. For a fixed Fermi energy, the change in the Landau tube structure as a function of the external magnetic field causes oscillating behaviors in various electronic properties. [109, 110]. A notable example is the de Haas-van Alfphen effect of the magnetization. There, we observe oscillations as a function of the inverse magnetic field with its frequency determined by the area surrounded by the extremal orbit of the Fermi surface cross-section perpendicular to the external field. By measuring the oscillating frequency while changing the direction of the external field, we can obtain the 3D profile of the Fermi surface.

Measuring the Fermi surface geometry with the de Haas-van Alphen effect has been developed decades ago, but is still quite important in condensed-matter physics [111, 112, 113, 114, 115, 116, 117, 118, 119, 120], being a source of new discoveries. A notable example is the recent discovery of the bulk-like quantum oscillations in the family of Kondo insulators like SmB_6 [112]. As we mentioned, following the traditional theory of the de Haas-van Alphen effect, the oscillation takes place only when there exists a clear Fermi surface. Hence, the quantum oscillation observed in the insulating systems posed a critical question on their electronic properties, and triggered studies [121, 122] searching for a novel charge-neutral Fermi surface [123, 124, 125, 126].

The magnetic oscillation is powerful without doubt. However, if we are going to apply it to magnetic materials, a problem arises. In performing the magnetic oscillation measurement, we apply a static magnetic field and change its direction and strength to probe the Fermi surface. When the target material is magnetically ordered, the external field affects both the electric and magnetic properties. In particular, when the external field is very strong (which is usually the case in the magnetic oscillation measurement), the original magnetic order is strongly modulated by the field,

changing the electronic property that we are interested in. Therefore, if we are to study the electronic properties of antiferromagnetic, ferrimagnetic, or non-collinear magnetic states, for example, what we observe would always be those of a forced ferromagnetic state [Fig. 3.1(a)].

The strong external field is problematic even for collinear magnetic states. To probe the 3D Fermi surface, we have to change the direction we apply the external field. However, under a strong external field, the magnetic moments would follow the change in the direction of the field and hence we cannot probe the full 3D profile of the Fermi surface.

To probe the Fermi surface profile of conducting magnets, therefore, the magnetic oscillation is not a suitable option. As a way of studying the electric band structure of metals, angular resolved photoemission spectroscopy (ARPES) exists but it is as well not applicable to systems with macroscopic magnetizations or those under an external field. Therefore, it has been difficult to study the field-induced phase transitions where the strength and direction of the external magnetic field play important roles. For example, pyrochlore iridates are known to show a field-induced change of their electronic structure as metals, insulators, and topological semimetals [127, 128]. Measurement of the field-induced phase transition in pyrochlore iridates relies on the change in the electric conductivity at present, but the magnetic oscillation, if properly extended to conducting magnets, will allow us to directly measure the change in the Fermi surface as a function of the external field. As we have seen in the previous chapters, a thin film of chiral magnets is also an example showing the field-induced phase transition in which we observe helical magnetic phase, skyrmion crystal phase, and ferromagnetic state [69, 72, 77] depending on the strength of the out-of-plane magnetic field.

The aim of this section is to propose a possible extension of the magnetic oscillation measurement in a way applicable to metallic magnets. We consider a system in which we have both conduction electrons and localized magnetic moments. As we see below, the use of CVBs instead of the static magnetic field would suppress the "side effect" on the magnetic structure. We mention that in this section, we do not consider magnetic metals where conduction electrons themselves are responsible to the magnetization.

The key idea is to exploit the difference in the timescale [28, 129, 130] which we also used in the previous chapter. The relaxation time of electrons is orders of magnitude shorter than that of spins. The former is typically of the order of 10-100 femtoseconds coming from the electon-electron scatterings with the energy scale of eV while the latter is longer than 1 ps because of the smaller energy scale of the magnon-magnon and

magnon-electron scatterings [Fig. 3.1(c)].

3.1.2 Magnetic oscillation with a pulse field

Let us consider a pulse of magnetic field with its duration between these two different timescales. For conduction electrons, such a pulse works as a static magnetic field and forms Landau levels while for localized moments, that is too short to follow. Therefore, by changing the amplitude of the pulse we can measure the oscillation associated to the **original** magnetic structure of localized moments [see Fig. 3.1(b)]. The proper pulse width would be 100 fs to a few ps, so that the frequency of the beam to be used is in the region of far-infrared to THz. In such a high frequency region, we cannot use equipments like coils and solenoids to produce magnetic fields and we would rely on optical means.

The side-effect problem would be avoided by using a pulsed magnetic field. However, if we use conventional Gaussian beams, heating caused by the electric-field component becomes problematic. The electron temperature after the pulse excitation will be much higher than the energy scale of Landau tubes, smearing out the oscillation in physical quantities. What we need is thus a source of a "pure magnetic field" without accompanying the electric field in the optical frequency regime[1]. Here, the CVBs takes the role.

As we introduced in Chapter 1, near the focus, a focused azimuthal CVB develops the longitudinal AC magnetic field, and its electric-field components is suppressed there. Unlike Gaussian beams, therefore, the strong heating due to the electron-hole excitations could be avoided. The important point to be kept in mind is the length scale. The longitudinal magnetic field of focused CVBs is present only around the focus. Therefore, taking into account the diffraction limit, the size of the region is most probably of the order of the wavelength. As we are considering CVBs in the far-infrared to THz region, the wavelength would be around O($10 - 100$) μm. To avoid being heated up by the electric field and measure the magnetic oscillation, the sample size should be small enough compared to that. Therefore, the typical sample size of the nonequilibrium magnetic oscillation will be O(100) nm to O(1) μm. Preparing a sample of this size is, in nowadays not so difficult by using, for example, a focused ion beam equipment.

[1]Near the focus, the longitudinal magnetic field is spatially homogeneous.

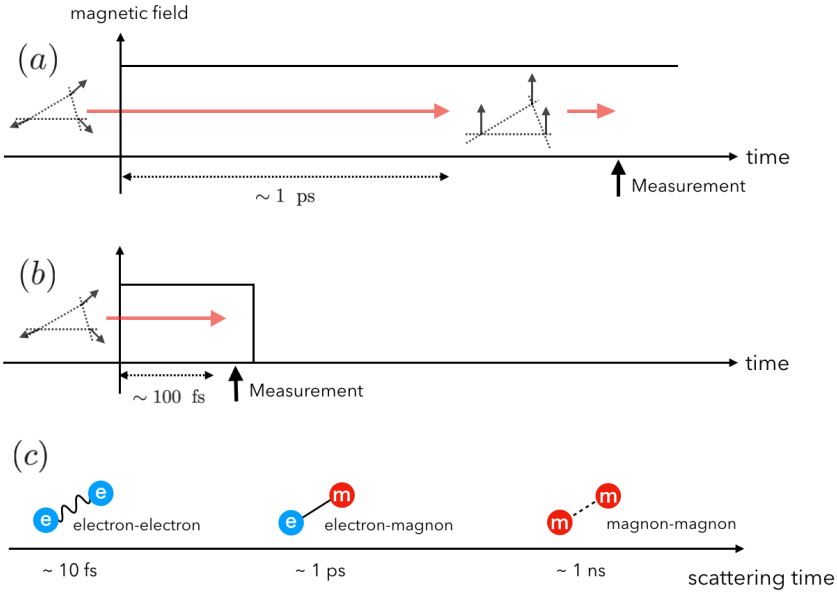

Figure 3.1: (a): Schematic illustration of the conventional magnetic oscillation measurement performed to a conducting magnet. Arrows on vertices of the lattice represent localized moments and the thick black arrows do the static magnetic field perpendicular to the lattice. Irrespective of the original spin texture, the static field makes the system to be a forced ferromagnet. (b): Schematic illustration of the laser-based nonequilibrium measurement proposed in this paper. We apply a cylindrical vector (CV) beam (explained later) pulse to form the Landau levels to which electrons relax. The latter method has the sensitivity to the magnetic structure of the initial state. Panel (c) shows the hierarchical structure of the scattering times [28, 129, 130].

3.1.3 Example: s-d coupled electrons

We take a simple model to clarify the situation and see how the oscillation signal depends on the magnetic structure of the localized moments. We consider the following Hamiltonian for a Kondo-like system; a tight-binding model on a square lattice with an s-d type coupling:

$$\begin{aligned} H = & -t \sum_{\langle \boldsymbol{r},\boldsymbol{r}'\rangle,\sigma} c^\dagger_{\boldsymbol{r},\sigma} c_{\boldsymbol{r}',\sigma} e^{-i\frac{e}{\hbar}\int_{\boldsymbol{r}}^{\boldsymbol{r}'} \boldsymbol{A}(\boldsymbol{x})\cdot d\boldsymbol{x}} \\ & - 2\mu_B B \sum_{\boldsymbol{r}} s^z_{\boldsymbol{r}} - 2J_{\mathrm{ex}} \sum_{\boldsymbol{r},\alpha,\beta} \boldsymbol{m}_{\boldsymbol{r}} \cdot \boldsymbol{s}_{\boldsymbol{r}} + H_{\boldsymbol{m}}. \end{aligned} \tag{3.1}$$

The first term is the nearest-neighbor hopping with amplitude t. We use $\boldsymbol{r}$ and $\boldsymbol{r}'$ to specify the sites on the lattice. The magnetic field B of the focused CVB is introduced by the Peierls substitution of the vector potential $\boldsymbol{A}(\boldsymbol{r}) = (By, 0, 0)$. Here, the magnetic field B is of the focused azimuthal CV beam. As we discussed before, in a limited time domain we can treat that as a static magnetic field for electrons. The second term is the Zeeman coupling of the electron spins $(\boldsymbol{s}_{\boldsymbol{r}})_{\alpha,\beta} = c^\dagger_{\boldsymbol{r},\alpha} \boldsymbol{\sigma}_{\alpha,\beta} c_{\boldsymbol{r},\beta}$ with the magnetic field of the beam. The third term is the s-d type coupling between the conduction electrons and the localized moments. Depending on the direction of the magnetic moment $\boldsymbol{m}_{\boldsymbol{r}}$, an electron at that site $\boldsymbol{r}$ feels an effective magnetic field. The last term $H_{\boldsymbol{m}}$ includes possible terms relevant for magnetic moments **except** the coupling with the external field. This is made possible by the discrepancy in the timescale we have discussed in Sec. 3.1.2. That is, for localized moments, the external field is too short in its pulse width to be affected by it.

The coupling constant of the s-d type exchange J_{ex} is typically of the order of sub eV to eV. For example, that of the f-d exchange in pyrochlore iridates $R_2Ir_2O_7$, J_{ex} is around 5 % of the hopping t [131]. If we regard the J_{ex} as the Hund coupling in transition-metal compounds like Mn oxides, its energy scale would even reach to eV [132, 133]. In the following, we take $t = -3$, $J_{\mathrm{ex}} = 2$ in the unit of electron volt and measure the magnetic field B in the unit of Tesla. The lattice constant is taken to be $a = 5$ Å. In this case, the band edge is at $E_F = -1$ for the ferrimagnetic and $E_F = -2$ for the antiferromagnetic cases.

We consider three different magnetic structures; ferromagnetic [$\boldsymbol{m}_{\boldsymbol{r}} = (0, 0, 1)$ for all $\boldsymbol{r}$], antiferromagnetic, and ferrimagnetic which are realized by the proper choices of $H_{\boldsymbol{m}}$. In the latter two cases, we divide the system into two sublattices s_1 and s_2, and then define $\boldsymbol{m}_{\boldsymbol{r}\in s_1} = (0, 0, 1)$, $\boldsymbol{m}_{\boldsymbol{r}\in s_2} = (0, 0, -1)$ for the antiferromagnetic case and $\boldsymbol{m}_{\boldsymbol{r}\in s_1} = (0, 0, 1)$, $\boldsymbol{m}_{\boldsymbol{r}\in s_2} =$

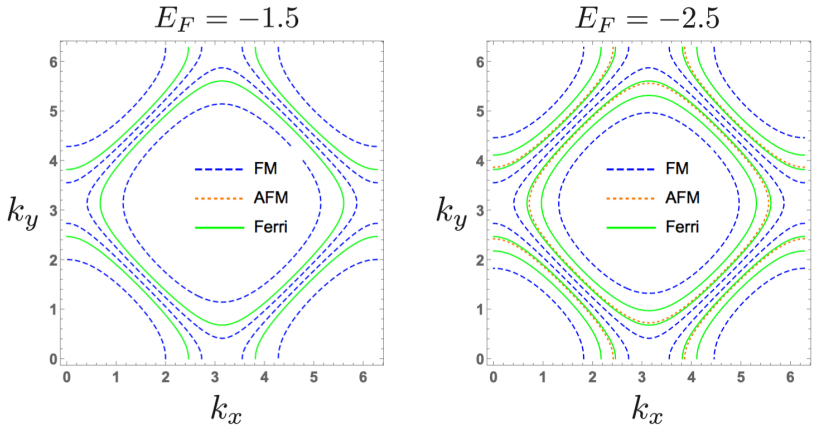

Figure 3.2: Fermi surface of the model (3.1) for ferromagnetic (FM), antiferromagnetic (AFM), and ferrimagnetic (Ferri) orders of the localized moments. We take $t = -3$ and $J_{\rm ex} = 2$ and draw the corresponding Fermi surfaces for two different Fermi energies $E_F = -1.5$ and -2.5. Since the valence-band edge of the AFM state is at $E = -2.0$, in the left panel, we see no Fermi surface in th e AFM case.

$(0, 0, -0.5)$ for the ferrimagnetic case. In Fig. 3.2, we show the Fermi surfaces of the model (3.1) for these different magnetic structures.

We calculate the spin polarization of conduction electrons with the Fermi energy E_F at zero temperature of the system with the linear dimensions $L_{x,y} = 30a$ where a is the lattice constant. We take a fixed Fermi energy E_F irrespective to the external field since the change in the chemical potential as a function of the external field does not affect the oscillation frequency at $T = 0$ [134].

The conduction-electron spin polarization of a free-electron system in the ground state is defined as

$$\langle s^z_{\rm tot} \rangle_B = \sum_{E_n < E_F} \langle E_n | s^z_{\rm tot} | E_n \rangle \,. \tag{3.2}$$

Here $s^z_{\rm tot} = \sum_{\boldsymbol{r}} s^z_{\boldsymbol{r}}$ is a sum of the z component of conducting-electron spins at each site, and $|E_n\rangle$ is the single-electron eigenstate with energy E_n. Assuming the discrepancy in the relaxation timescale, we study this electron spin polarization while changing the amplitude of the applied magnetic field coming from the CVB.

Figure 3.3 summarizes the field dependence of the conduction-electron

spin polarization. We focus on the oscillating part of the spin polarization by plotting $\langle s^z_{\rm tot}\rangle_B / B$ as a function of the inverse magnetic field. We consider two different Fermi energies $E_F = -1.5$ and $E_F = -2.5$ and show the results in the panels ($a1$-$a2$) and ($b1$-$b2$), respectively. We see clear oscillations and peaks in the Fourier space. Using the Fermi surface contour [shown in Fig. (3.2)] and the formula

$$\delta\left(\frac{1}{B}\right) = \frac{2\pi e}{\hbar S_f}, \tag{3.3}$$

we calculate the oscillating frequency and compare that with the numerical plot. The left-hand side is the period of the oscillation, and S_f is the area of the extremal orbit in the Fermi surface. The peak positions predicted from Eq. (3.3) [109, 110] are shown as vertical lines in the panels $(a2, b2)$. We see that the numerically obtained frequency perfectly matches with the formula Eq. (3.3).

As we saw above, the formula Eq. (3.3) works also for conducting magnets. By changing the pulse field amplitude of the azimuthal CVBs, we can study the Fermi surface in a way having sensitivity to the magnetic order. Moreover, using CVBs allows us to easily change the direction in which we apply the beam so that we can study the full 3D profile of the Fermi surface.

3.1.4 Discussion

Here we discuss several issues on the feasibility of the proposed method. As we mentioned, in this part we assumed that the large discrepancy in the relaxation timescale makes it possible for us to fix the magnetic structure of the localized moments. However, since the energy scale of the s-d type exchange coupling can be very high, this is in reality a subtle assumption.

If the longitudinal magnetic field of CVBs drastically changes the electron spin polarization, through the large s-d type exchange, there might appear a very large effective magnetic field for the localized moments, resulting in the fast magnetization dynamics. Fortunately, this is not the case. The field-induced change in the electron spin polarization is small. In realistic experiments, we use an external field of O(1-10) Tesla. The energy scale of the Zeeman coupling with this field is of the order of meV at most. Hence, compared to the electron-spin polarization induced by the s-d type coupling, the field-induced change in that will be quite small. This can be also confirmed from Fig. 3.3. There, we see that the change is very small: O(mμ_B) for O(10) Tesla. Hence, the change in the effective

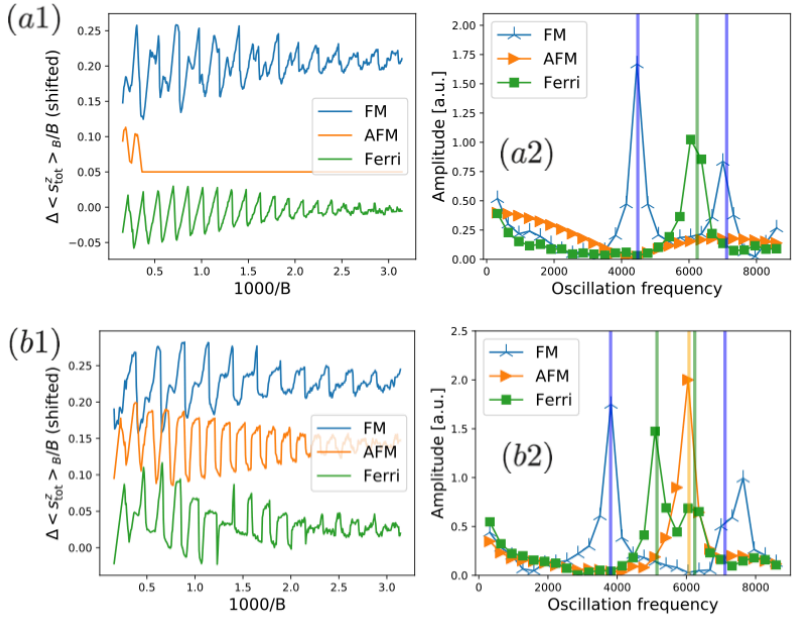

Figure 3.3: Magnetic oscillation for ($a1$,$a2$): $E_F = -1.5$ and ($b1$,$b2$): $E_F = -2.5$. We consider three (ferromagnetic, antiferromagnetic, and ferrimagnetic) different magnetic orders. $(a1, b1)$: field dependence of the electron spin polarization $\Delta \langle s^z_{\rm tot} \rangle_B = \langle s^z_{\rm tot} \rangle_B - \langle s^z_{\rm tot} \rangle_0$. The origins are shifted for visibility. These oscillations are Fourier transformed to obtain panels $(a2, b2)$. The vertical lines in these panels correspond to the oscillation frequency calculated from the area of each extremal orbit of the Fermi surface [see Eq. (3.3)].

magnetic field felt by the localized moments will be very small for the realistic value of the beam amplitude, and the original magnetic configuration will be virtually unchanged in most cases.

The frequency of the incident beam should be around THz to far-infrared. To observe the magnetic oscillations in the wide range of materials, we need a field amplitude of O(1-10) Tesla. In the THz region, this is a bit challenging, though a field of O(1) Tesla is becoming possible very recently. In the far-infrared region, it is much easier. There are a variety of molecular lasers with fairly large field amplitude. For example, we could use CO_2 lasers or lasers pumped by them.

In order to observe the oscillation, we have to measure the nonequilibrium spin polarization in the optical timescale. Hence, we would rely on the magneto-optical measurements such as Kerr or Faraday rotations for the femtosecond pulses. Since the magnetic oscillation originates form the Landau tube structure, we may use any physical quantities related to that. For example, we could use the optical conductivity to probe the oscillation as in Shubnikov-de Haas measurement.

The proposed method is advantageous for investigating metals with localized moments but is also useful in studying non-magnetic metals. The key point is the all-optical nature of that method. As an example, let us consider a magnetic oscillation of metals under ultra-high pressure of a diamond anvil cell. Diamond anvil cell [135] is a common way of pressing materials to more than a hundred gigapascal but has a weakness in the accessibility to a sample inside the cell. There, both the conventional de Haas type measurement and ARPES are hard or totally impossible so that Fermi surface of materials under ultra-high pressure is, even for simple metals, hard to probe. Unlike existing methods, our nonequilibrium magnetic oscillation method is all-optical and thus applicable to this situation because diamonds are highly transparent in the THz to far-infrared frequency.

3.2 Magnetic field spectroscopy with CVBs

In the previous section, we discussed the possibility of nonequilibrium magnetic oscillation. There, we completely ignored the electric field effect. However, in order to use CVBs for spectroscopic purposes, electric absorption could cause a severe problem.

Suppose that we are interested in magnetic properties of a target and are to measure magnetic field absorption to probe them. In particular, we work on high-frequency properties, for example, in the THz region. Magnetic-field spectroscopy at the optical frequency has two advantages over that with microwaves. Firstly, it has much better temporal resolution because it is basically determined by the pulse width of the incident oscillating field. Secondly, it has a wider range of applicability. For example, magnetic resonance frequency of antiferromagnetic materials can be at (sub-)THz due to so-called exchange enhancement. In this case, the use of THz fields is essential to probe their properties.

Unlike in the low-frequency region like GHz, at the THz frequency we have to rely on optical means to apply an oscillating magnetic field. The problem is, if we use conventional lasers, the strong electric-field absorption, which is usually dominant over the magnetic one by several orders [136], masks the magnetic field absorption in which we are interested. Therefore, optical probe of magnetic properties of matters is possible only for insulators where electromagnetic field absorption comes dominantly from magnetic dipole transitions.

In the following, we first discuss how small the electric-field absorption can be by replacing Gaussian beams by focused CVBs. Based on it, next we give several applications; time-resolved electron spin resonance (ESR) of conducting materials, measurement and control of multiferroic materials, electron paramagnetic resonance (EPR) study of dynamical properties of biomolecules in their living environment.

3.2.1 Suppressed electric-field absorption for CVBs

Let us consider the competition of electric and magnetic field absorption in conductors. The electric-field absorption is determined by the real part of the electric conductivity, and the magnetic one is by the imaginary part of the magnetic susceptibility. In order for the magnetic absorption to be detectable, it does not have to be larger than the electric-field absorption in general. The electric-field absorption of conductors is well described by the phenomenological Drude model [109]. Therefore, the true competition

appears after subtracting the Drude-type contribution.

When the magnetic-field absorption is larger than (or at least comparable with) the electric-field absorption corresponding to the deviation from the Drude model (we call this deviation as microstructures in the following), we could probe it. For example, when the target has strong spin-orbit-coupling (SOC), the electric-field absorption through the mechanism so-called electron dipole spin resonance (EDSR) takes place. EDSR absorption is an example of the microstructures of electric conductivity.

In the following, we study absorption of focused CVBs by matters assuming that the sample (radius R) is sufficiently smaller than the wavelength λ. The electromagnetic-field absorption of matters is written as[2]

$$\alpha = \sum_{i,j} \sigma'_{ij}(\omega) E_i E_j + \omega \chi''_{ij}(\omega) B_i B_j. \tag{3.4}$$

Here σ' and χ'' are the real and imaginary parts of the electric conductivity and the magnetic susceptibility, respectively. The subscripts i, j are for the spatial coordinates. Since $R \ll \lambda$, we can expand $E^{\phi}(\rho, \phi)$ in Eq. (1.19) in terms of $\rho k < R/\lambda \ll 1$:

$$E^{\phi}(\rho, \phi) = 2Ak\rho \int_0^{\alpha} \sin\theta \cos^{\frac{1}{2}}(\theta) \ell_0(\theta) \frac{\sin\theta}{2} + O(k^3\rho^3). \tag{3.5}$$

The leading order term is $O(k\rho)$, and that of absorption is, therefore, $O(k^2\rho^2)$. After integrating over the sample area, the total absorption is found to be $O(R^2/\lambda^2)$ in the leading order. In contrast, if the incident beam is of a simple Gaussian type, as it is approximately a plane wave near the focus, the leading order of the absorption is independent of the ratio R/λ. This shows that replacing Gaussian beams by focused CVBs serves to suppress the electric-field absorption by the factor of $O(R^2/\lambda^2)$.

We define "effective conductivity" $\sigma'_{\text{eff}}(\omega) = \frac{R^2}{\lambda^2}\sigma'(\omega)$ to make the contrast with Gaussian beams better. Since the lattice constant is much smaller than THz wavelength, locally electrons feel the fields as if being linearly polarized one. Hence, suppression of the electric-field absorption by the geometrical feature of the electric field is equivalent to replacing $\sigma'(\omega)$ by $\sigma'_{\text{eff}}(\omega)$. For example, when $R = 1$ μm, and the wavelength is 300 μm (1THz), σ'_{eff} becomes about 10^{-5} smaller than $\sigma'(\omega)$.

[2]In multiferroic materials, there could appear cross-terms of electric and magnetic fields. However, as we are interested in conductors here, we ignore them.

Below we use the ratio of the two contributions in Eq. (3.4),

$$P = \frac{\omega\chi''(\omega)B_{\rm CVB}^2}{\sigma'(\omega)E_{\rm CVB}^2}, \tag{3.6}$$

as a measure of the relative strength of absorption. Here $B_{\rm CVB}$ and $E_{\rm CVB}$ are field amplitudes of the incident CVB. By using the effective conductivity, we can rewrite Eq. (3.6)

$$P = \frac{\omega\chi''(\omega)B_{\rm G}^2}{\sigma'_{\rm eff}(\omega)E_{\rm G}^2} = \frac{\omega\chi''(\omega)}{\sigma_0^{\rm eff}c^2} \tag{3.7}$$

Here we define $E_{\rm G}$ and $B_{\rm G}$ as field amplitudes of the corresponding Gaussian beams and use the relation $B_{\rm G} = E_{\rm G}/c$ to reach to the final expression. We also use the DC value of the effective conductivity $\sigma_0^{\rm eff}$ since the dominant Drude-type contribution is, at THz frequency, well approximated by the DC value.

Let us consider a two-dimensional (2D) conductor placed in the $y-z$ plane under a static in-plane magnetic field B_0. This is a standard situation of ESR, where the magnetic resonance takes place at the resonance frequency $\omega = \gamma B_0$. The imaginary part of the magnetic susceptibility is, by solving Bloch equation of electron spins derived to be

$$\chi'' \simeq \frac{\chi_0}{2}\gamma B_0 T_2 \frac{1}{1+(\omega-\gamma B_0)^2 T_2^2}, \tag{3.8}$$

where T_2 is the transverse relaxation time of the total spin, and χ_0 is the real-part of magnetic susceptibility at $\omega = 0$. At the resonance $\omega = \gamma B_0 \equiv \omega_0$, we have $\chi'' = \chi_0(\omega_0 T_2)/2$. If we assume THz resonance frequency and take T_2 to be about a nanosecond (which is the typical timescale of the dynamics of a macroscopic magnetization), the peak height will be $\chi'' \simeq 10^3\chi_0/2$. Using these parameters, Eq. (3.7) leads to

$$P \sim 0.02\frac{\chi_0}{\sigma_0^{\rm eff}} = 2000\frac{\chi_0}{\sigma_0}. \tag{3.9}$$

The dimensionless factor P works as a criterion. If P is too small, absorption peaks from magnetic dipole transitions would be smeared out by electric absorption peaks (in particular, those from microsctructures of electric conductivity). The amplitude of microsctructures is strongly material dependent. In the next subsection, we take EDSR as a source of the microstructure and examine the threshold quantitatively, but here we just assume that the amplitude of the microstructure is 1% of σ_0. In this

case, the P factor has to satisfy $P > 0.01$ in order for us to detect magnetic absorption peaks. Then, the DC electric conductivity of the target material must satisfy $\sigma_0 < 2 \times 10^5 \chi_0$. If $\chi_0 \sim 4\pi \times 10^{-7}$[H/m], we obtain $\sigma_0 \leq 0.3$ [S/m]. Remember that if we use Gaussian beams in the first place, the threshold value becomes $\sim 10^{-5}$ times smaller.

The threshold value $\sigma_0 = 0.3$ [S/m] is higher than the electric conductivity of typical semiconductors like Si or GaAs at weak doping (see Fig. 3.4). Hence, though it strongly depends on the details of microstructures and the value of magnetic susceptibility, using focused CVBs instead of Gaussian beams could be quite useful for studying magnetic absorption in various semiconductors.

The magnetic absorption does not necessarily come from conduction electrons. The resonance can also originate from magnetic impurities, localized moments, and magnetic subsystems in conductors. Moreover, the dipole-transition itself can have a different origin like zero-field splitting due to magnetic anisotropy. As we will discuss in the next subsection, in antiferromagnets, the zero-field splitting is often at (sub-) THz region, so that high-frequency measurement plays an important role.

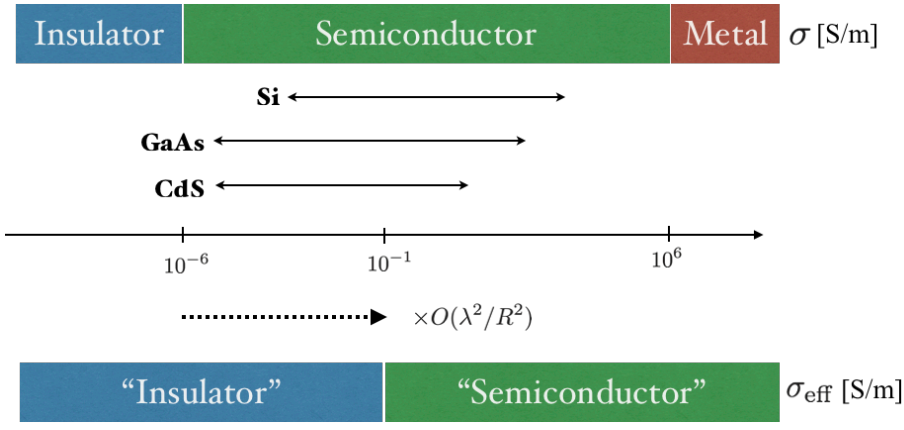

Figure 3.4: Enlarged scope of magnetic-field spectroscopy by the use of the cylindrical vector beam. We assume that the square of the ratio of the wavelength and the system size to be $(R/\lambda)^2 = 10^{-5}$. We show known values of the electric conductivity of several materials [137].

In the argument above, we have electric conductors in mind. However, electric absorption can originate also from electric dipoles, i.e. dielectric absorption, in insulating systems. In the following, we discuss spectroscopic uses of focused CVBs, discussing both conducting and dielectric systems.

3.2.2 Applications

Given the argument above, here we propose several applications of focused CVBs for magnetic-field spectroscopy of both conducting and dielectric systems.

Magnetic resonance of conducting systems

Here we discuss magnetic resonance measurements in more details. As we noted, in spin-orbit-coupled systems, one of the primary sources of the conductivity microstructures is EDSR. Hamiltonian of a Rashba-type SOC is, for example, given by

$$H_{\mathrm{RSOC}} \propto \sum_{\boldsymbol{p},\alpha,\beta} c^{\dagger}_{\boldsymbol{p},\alpha}(\boldsymbol{d}_{\boldsymbol{p}} \cdot \boldsymbol{\sigma}_{\alpha,\beta}) c_{\boldsymbol{p},\beta}, \tag{3.10}$$

where $\boldsymbol{\sigma}$ are Pauli matrices with matrix indices α and β, and $\boldsymbol{d}_{\boldsymbol{p}}$ is the SOC vector. The operators $c_{\boldsymbol{p},\alpha}$ and $c^{\dagger}_{\boldsymbol{p},\alpha}$ are the annihilation and creation operators of fermions in the second quantization form [109]. The SOC vector works as a momentum-dependent magnetic field for electrons, leading to EDSR absorption with broad and high peaks.

Let us take a simple one-dimensional tight-binding model to study the effect of EDSR quantitatively. The model that we consider is the following one:

$$\begin{aligned} H = &-t_0 \sum_{i,\alpha} c^{\dagger}_{i+1,\alpha} c_{i,\alpha} + h.c. - g\mu_B B \sum_{i,\alpha,\beta} c^{\dagger}_{i,\alpha} \sigma^{x}_{\alpha,\beta} c_{i,\beta} \\ &+ i\lambda_R \sum_{i,\alpha,\beta} c^{\dagger}_{i+1,\alpha} \sigma^{y}_{\alpha,\beta} c_{i,\beta} + h.c., \end{aligned} \tag{3.11}$$

where the second term is the Zeeman coupling with the external field, and the third one is the Rashba SOC. Here t_0 is the electron hopping, g is the g-factor, μ_B is the Bohr magneton, and λ_R is the SOC constant. This is a spacial case of the model investigated in Ref. [138]. Although this is a one-dimensional model, we can take a collection of such chains to calculate the standard, three-dimensional electric conductivity.

As parameters, we take $\lambda_R/t_0 = g\mu_B B/t_0 = 10^{-3}$. We assume the intra- and inter- chain lattice constants to be $a_{\parallel} = a_{\perp} = 0.5$ nm. Since the electron hopping t_0 is of the order of eV, the magnitudes of the SOC constant and the magnetic field are of THz. According to the calculation in Ref. [138], for these parameters, the EDSR contribution to the electric conductivity at the frequency $\omega \sim g\mu_B B$ is about 10^{-8} to 10^{-1} [S/m] de-

pending on the electron filling per lattice sites. Recalling Fig. 3.4, we notice that the EDSR contribution is in the "insulating" region of the effective conductivity σ_{eff}. Therefore, with CVBs, we may overcome the dominant EDSR contribution to the THz absorption in various semiconductors with SOC.

So far, we have considered magnetic resonance of paramagnetic or ferromagnetic conductors. In these cases, the resonance frequency is determined by the Zeeman coupling with the external field. Therefore, to lift the resonance frequency to be at the THz region, we have to apply a fairly strong magnetic field over 10 Tesla. However, magnetic resonance can also come from localized magnetic moments. In particular, when these moments are coupled antiferromagnetically, so-called the exchange enhancement takes place. Because of the strong exchange coupling J, antiferromagnetic resonance coming from a magnetic anisotropy A is lifted to the (sub-) THz region as $\omega = \sqrt{JA}$ [15, 16]. In ferromagnetic conductors, the advantage of ESR using CVBs over ESR at low-frequency using existing methods is limited to its improved temporal resolution. However, in antiferromagnetic cases, the large zero-field splitting makes low-frequency AFMR impossible. Therefore, CVBs would be a unique and natural way of studying antiferromagnetic conductors.

Electromagnons in multiferroics

The suppression of electric-field absorption is also true for dielectric losses. In this and the next subsections, we consider dielectric systems.

As we noted in the previous chapter, multiferroic materials like chiral magnets gather attention nowadays. The coupling between the local electric polarization and local magnetic moments makes spin excitations to be *electromagnons* which are active to both electric and magnetic fields.

To study the magneto-electric coupling and electromagnons in multiferroic materials, we would perform absorption measurements and/or pump-probe measurements of multiferroic materials using lasers. However, if we use Gaussian beams, as both electric and magnetic fields drive the magnetization dynamics, we cannot experimentally separate these contributions. In a limited case in which we already know the magneto-electric properties of the target beforehand [139], we could identify individual contributions to the dynamics by, for example, combining measurements using lasers with several different polarizations. However, this is not always the case. In general, we do not even know the background mechanism of multiferroicity. In particular, if the target is a newly synthesized material, separating the two contributions in that way is impossible.

Using CVBs allows us to excite the dynamics of electric and magnetic dipoles individually. As a proof of the concept, let us consider a simple toy model of multiferroic magnets: a pair of classical spins $\boldsymbol{S}_1$ and $\boldsymbol{S}_2$, and apply a linearly polarized plane wave to model the situation of measurements with Gaussian beams. We assume that due to the spin-current mechanism [85], there appears an electric polarization $\boldsymbol{p} = \lambda_c \boldsymbol{e}_{1,2} \times (\boldsymbol{S}_1 \times \boldsymbol{S}_2)$ where $\boldsymbol{e}_{1,2}$ is the unit vector in the direction connecting these spins (which we take in the x direction; $\boldsymbol{e}_{1,2} = \hat{x}$).

We apply a strong static magnetic field H_0 in the x direction and a linearly polarized beam; $\boldsymbol{B}(t) = B\hat{y}\cos(\omega t)$, $\boldsymbol{E}(t) = E\hat{z}\sin(\omega t)$. Using the instantaneous directions of the spins at each time t: $\boldsymbol{S}_1(t)$ and $\boldsymbol{S}_2(t)$, the Hamiltonian of this system is given in the following form:

$$H = -\boldsymbol{p}(t) \cdot \boldsymbol{E}(t) - g\mu_B(\boldsymbol{S}_1 + \boldsymbol{S}_2) \cdot \boldsymbol{B}(t) - g\mu_B H_0(S_1^x + S_2^x) - J\boldsymbol{S}_1 \cdot \boldsymbol{S}_2. \tag{3.12}$$

Assuming that the incident beam is weak compared with the static field, we consider the laser-induced dynamics of spins in the linear order of E and B. We expand the time-evolution of spins $\boldsymbol{S}_1(t)$ and $\boldsymbol{S}_2(t)$ as

$$\boldsymbol{S}_1(t) \simeq \hat{x} + \delta\boldsymbol{S}_1(t) + \mathrm{O}(E^2, B^2), \tag{3.13}$$

$$\boldsymbol{S}_2(t) \simeq \hat{x} + \delta\boldsymbol{S}_2(t) + \mathrm{O}(E^2, B^2), \tag{3.14}$$

where $\delta\boldsymbol{S}_1$ and $\delta\boldsymbol{S}_2$ are small-amplitude vectors linear in E and B.

In the linear order of E and B, these spins can be independently treated as the instantaneous polarization vector $\boldsymbol{p}(t)$ becomes a linear sum of each spin:

$$\begin{aligned}\boldsymbol{p}(t) &= \lambda_c \boldsymbol{e}_{1,2} \times (\boldsymbol{S}_1(t) \times \boldsymbol{S}_2(t)) \\ &= \lambda_c \left[(\delta S_1^z(t) - \delta S_2^z(t))\hat{y} + (\delta S_2^y(t) - \delta S_1^y(t))\hat{z}\right] + \mathrm{O}(E^2, B^2),\end{aligned} \tag{3.15}$$

and the exchange coupling also does as $\boldsymbol{S}_1 \cdot \boldsymbol{S}_2 = 1 + \delta S_1^x + \delta S_2^x + \mathrm{O}(E^2, B^2)$. Therefore, as long as the beam amplitude is weak and the frequency of the beam is far away from the magnetic resonance, the laser-induced dynamics of spins can be easily calculated as a solution of a single-body problem.

We focus on the time evolution of $\boldsymbol{S}_1(t)$ (see Fig. 3.5) and analytically solve the Landau-Lifshitz equation to obtain the time evolution of $\delta S_1^y(t)$ as

$$\delta S_1^y(t) = \frac{\gamma^2 \tilde{H}_0 B + \omega\lambda_c E}{\gamma^2 \tilde{H}_0^2 - \omega^2} \cos(\omega t), \tag{3.16}$$

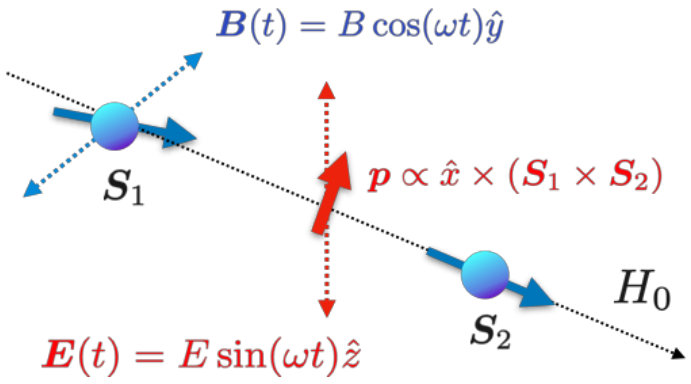

Figure 3.5: Setup of the calculation of the dynamics of $\boldsymbol{S}_1$ in the leading order of the incident fields.

where we assumed that $S_1^y(t) = 0$ if $E = B = 0$ and define $\tilde{H}_0 = H_0 + J/(g\mu_B)$. We see that the spin dynamics is driven by both Zeeman and magneto-electric couplings with the beam. As we know the functional form of the dynamics Eq. (3.16), in this case, we can read out magnetic and electric contributions by measuring the time evolution while changing parameters like ω and H_0. However, as we noted, this is not possible in general.

On the other hand, if we use CVBs instead of linearly polarized beams, we can set $E = 0$ or $B = 0$ while keeping the other finite in Eq. (3.16). Therefore, we can study the spin dynamics purely induced through magnetic or electric mechanisms without being annoyed by the contribution from the other one.

The fact that we can change the directions, amplitudes, and the relative phase of applied electric and magnetic fields by using focused CVBs enables us to obtain richer information of multiferroic materials. This approach does not require any prior knowledge of the magneto-electric coupling in the target. Hence, CVBs will largely streamline the experimental characterization of (newly-synthesized) multiferroic materials.

Electron paramagnetic resonance in absorbing media

As a primary tool for chemistry and biology, EPR [140, 141, 142] is widely accepted. In EPR, magnetic absorption spectrum works as a fingerprint of unpaired electrons (free radicals) in the target system. The free radical is not necessarily a part of the target molecule. We can use a stable radical as a "marker" and use its spectrum to probe the target indirectly. This approach is known as a spin label (or spin probe) method of EPR and is a common way of studying macromolecules like a protein and DNA.

Among variants of EPR methods, time-dependent EPR provides information of molecular dynamics like rotation on the occasion of chemical reactions. In the time-dependent EPR, we use a pulse field and measure its absorption by free radicals, and its temporal resolution is limited by the pulse width, or the frequency. This is one of the driving forces toward the very high frequency (VHF) EPR/ESR [143].

If we are interested in the dynamical properties of biological molecules in their living environment, the most natural way of studying them is to probe EPR of the target molecules in an aqueous environment. However, at high frequency like THz, strong dielectric absorption by liquid water causes large dielectric loss and makes it difficult for us to measure the magnetic-field absorption [144]. Using a pulse CVB is a way of avoiding absorption by solvent molecules like water. Since the spin-triplet-excitation energy of liquid water is of the order of eV [145], magnetic-field absorption at (sub-)THz frequency would be, if exists, by the solute molecules.

As we noted, the absorbing radical could be the target molecule itself or spin markers of the spin label/probe methods. A commonly used spin marker is a nitroxide radical or molecules with it. However, in order to perform a VHF EPR, we have to apply a strong magnetic field to lift the Zeeman energy. Although this is possible, it costs and the strong field may alter the sample property.

Another way of measuring EPR at high-frequency explored recently is to use spin markers with a sizable zero-field splitting like single-molecule magnets [146, 147, 148]. For example, recent developments in chemistry allow us to design highly anisotropic molecules [149] which have the resonance frequency of (sub-)THz. Using CVBs would make it possible for us to use variety of single-molecule magnets as spin markers for the time-dependent EPR at high frequency.

3.2.3 Discussion

In this part, we explored the possibility of selectively measuring magnetic absorption of matters with CVBs. Under the realistic assumption for the sample size, we showed that the electric absorption can be suppressed several orders of magnitude. We enumerated some applications such as magnetic resonance measurement of conductors, study of magneto-electric coupling and electromagnons in multiferroics, and VHF EPR of molecules in biological environments. Other systems to be explored may include the spin-momentum-locked states of topological insulators [150, 151], magnetic superconductors, quantum dots/wells, and so on. The proposed THz time-

domain spectroscopy with CVBs would be, in these ways, a new window to nonequilibrium physics in diverse fields.

3.3 Imaging and controlling circulating currents

So far, our focus was on the longitudinal magnetic field of azimuthal CVBs. We discussed how to utilize that to applications like nonequirlibrium magnetic oscillation and magnetic absorption spectroscopy. In these situations, the electric-field component has been just a nuisance. In this subsection, on the other hand, we consider the azimuthal electric field. As long as we are primarily interested in the azimuthal nature of the electric field, we can ignore the effect of focusing and simplify the electric field as

$$\boldsymbol{E}(\rho,\phi) = \frac{C}{\sqrt{w}}\left(\frac{\rho}{w}\right)\hat{e}_\phi e^{-i\omega t-\rho^2/w^2}. \tag{3.17}$$

Here C is a constant. Because of the weak focusing, the magnetic-field configuration can be approximated by $\boldsymbol{B} \propto \hat{e}_\rho$. As noted before, Eq. (3.17) is obtained by superimposing two OVs.

For the following arguments, the value of the beam width w is not essential, though there is a physical limitation due to the diffraction limit. In particular, we do not require a sample to be smaller than that contrary to the applications discussed in the previous parts.

What we consider is a coupling between the azimuthal electric field (3.17) and circulating currents in matters. In particular, we consider its application to visualize and control edge current in topological insulators (TIs) [150, 151].

TIs are characterized by the coexistence of their insulating bulk and metallic edges/surfaces. Notable examples of TIs in 2D is quantum Hall insulators and quantum spin Hall insulators. As a prototypical example of TIs, both have been well studied both experimentally and theoretically. The existence of their metallic edge states and their chiral/helical nature are well studied by the transport measurements [152]. Researchers are also active for directly visualizing the edge modes [153, 154, 155, 156, 157]. Here we discuss how CVBs can contribute to characterize and control the edge transport.

3.3.1 Edge visualization

We consider a disk-shaped 2D TI with helical edge modes. We apply the azimuthal field (3.17) and consider its coupling with those edge states. We model the edge conduction as an inhomogeneous electric conductivity

coming from the exponential decay of the wavefunction away from the edge:

$$\sigma(\rho) = S\Theta(R-\rho)e^{2\frac{\rho-R}{\xi}}, \tag{3.18}$$

where R is the sample radius, ξ is the localization length, S is a constant, and $\Theta(x)$ is the Heaviside theta function. The value of ξ is determined by the bulk property of the sample like the band gap and is typically of the order of nm. As the peak position of the incident electric field is around the beam width w, we can expect that when the sample size R matches with the beam width w we would observe strong absorption by the edge modes. Then, by measuring the absorption while changing the beam width (focusing strength) we can quantify where and how much the electric conduction localizes.

By using Eq. (3.4), the electric absorption (time averaged) is, if we ignore the magnetic-field contribution, given by

$$\alpha(w) = \frac{SC^2}{2}\int_0^R \frac{1}{w}e^{2\frac{\rho-R}{\xi}}\left(\frac{\rho}{w}\right)^2 e^{-2\rho^2/w^2}\rho d\rho. \tag{3.19}$$

This integration can be performed analytically, and we have

$$\begin{aligned}
\alpha(w) &\propto \int_0^R \frac{1}{w}e^{2\frac{\rho-R}{\xi}}\left(\frac{\rho}{w}\right)^2 e^{-2\rho^2/w^2}\rho d\rho \\
&= \frac{e^{-2R\left(\frac{1}{\xi}+\frac{R}{w^2}\right)}}{32\xi^3 w}(\sqrt{2\pi}w^3\left(3\xi^2+w^2\right)e^{\frac{2R^2}{w^2}+\frac{w^2}{2\xi^2}} \\
&\times\left(\mathrm{erf}\left(\frac{w}{\sqrt{2}\xi}\right)-\mathrm{erf}\left(\frac{w^2-2\xi R}{\sqrt{2}\xi w}\right)\right) \\
&+ 2\xi w^2 e^{\frac{2R^2}{w^2}}\left(2\xi^2+w^2\right) - 2\xi e^{\frac{2R}{\xi}}\left(4\xi^2R^2+2\xi w^2(\xi+R)+w^4\right)).
\end{aligned} \tag{3.20}$$

Here $\mathrm{erf}(x)$ is the error function. If the localization is sufficiently strong, and the localization length ξ is much smaller than both w and R, we can expand Eq. (3.20) in terms of ξ to obtain the lowest-order expression

$$\alpha(w) = \frac{SC^2}{2}\frac{\xi R^3 e^{-\frac{2R^2}{w^2}}}{2w^3}. \tag{3.21}$$

Figure 3.6 shows the w dependence of the absorption $\alpha(w)$. The panel (a) shows a schematic illustration of the measurement. We measure the electric-field absorption while changing the beam width w. For comparison with edge modes of TIs, we also calculate the absorption by an ordinary

metal with homogeneous conductivity $\sigma(\rho) = \text{const.} \times \Theta(R-\rho)$. The panel (b) is for the ordinary metal and the panel (c) is for the TI. The inset of the panel (c) shows the conductivity profile assumed.

When the conductivity is spatially homogeneous, the absorption is linear in w for small w. On the other hand, when the current is localized at the edge, as is also obvious from Eq. (3.21), the w dependence is strongly nonlinear in w for small w, and there appears a rising edge around $w = R/2$. Moreover, as we expected, when the beam width w is around the sample radius the absorption takes its maximum. Therefore, from the absorption intensity we can read out where the current localizes and how large the localization length is.

For the calculation, we take the localization length to be $\xi = 0.05R$, which is unrealistically large since ξ is typically order of nm in TIs. Nevertheless, as shown in Fig. 3.6(c), the lowest-oder expression (3.21) works quite well. Hence, the simplified expression (3.21) would be useful as a fitting function for experiments.

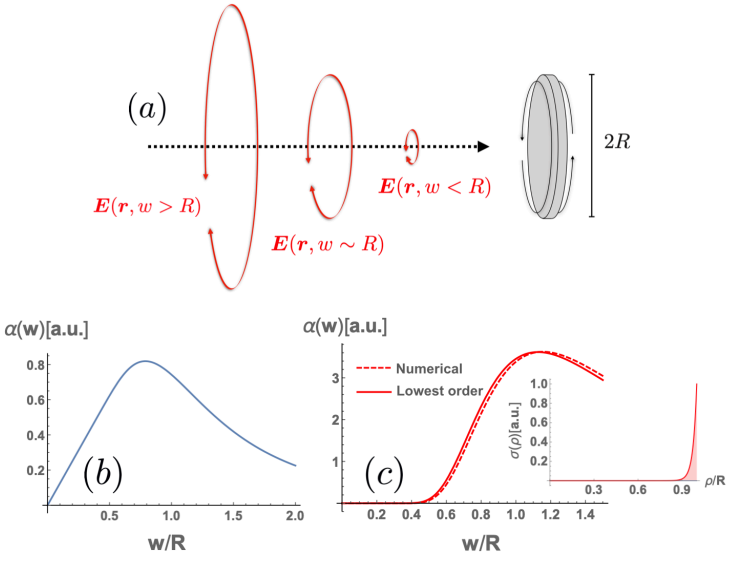

Figure 3.6: (a) Schematic illustration of the proposed measurement of the electric absorption. Beam width w dependence of the absorption by (b) an ordinary metal and (c) a topological insulator. In the inset of the panel (c), we show the spatial profile of the electric conductivity. We take the localization length $\xi = 0.05R$. The dashed and the solid curves in the panel (c) are calculations based on Eq. (3.20) and Eq. (3.21), respectively.

3.3.2 Orbital magnetization

Although the visualization of edge currents discussed above is interesting as a proof of concept, there are a number of other options for the purpose. In particular, in artificial systems like photonic and phononic crystals, their visualization is well established [153, 154]. Even in electronic systems, equipment like microscopes and SQUID offer a way of realizing is [155, 156, 157].

The advantage of using CVBs for studying edge currents is that it allows us to control them, not just to measure. Local probes like microscope and SQUID are sensitive to the local density of states but cannot drive circulating currents unlike CVBs. Since circulating currents generate an orbital magnetization[158, 159]:

$$M_{\mathrm{orb}}^{\mathrm{edge}} \propto \int_0^R 2\pi \boldsymbol{r} \times \boldsymbol{j}^{\mathrm{edge}} \rho d\rho = \int_0^R 2\pi \rho^2 \sigma(\rho) E^{\phi}(\rho) d\rho, \tag{3.22}$$

the azimuthal electric field of CVBs would be a unique way of controlling orbital magnetization within an optical timescale (see Fig. 3.7).

The total magnetization of a sample is given by the sum of the orbital and spin magnetization[3]. Therefore, changing the orbital magnetization with CVBs enables us to electrically control the magnetic properties of matters. Since we are assuming a weakly focused CVBs, the magnetic-field component can be regarded as purely radial $\vec{B} \propto \hat{e}_\rho$, so that the spin magnetization is not induced by the beam. Therefore, we can just measure the change in the total magnetization to demonstrate the electric control of the orbital magnetization.

The argument above does not require the current to have a topological origin. Rather, the induced orbital magnetization itself would be much larger for metals because of the large current density. In particular, when there exists a spin-orbit-coupling in the target, the orbital and spin magnetizations mutually affect with each other. Therefore, the laser-induced orbital magnetization may provide a new approach of optically controlling the spin degrees of freedoms.

[3]More precisely, the orbital magnetization is a sum of the surface and bulk contributions. The latter, which we ignored, comes from the microscopic circulating motions of electrons around each atom. Since these motions do not couple to the azimuthal electric field, the change in the bulk orbital magnetization would be negligible in the present case.

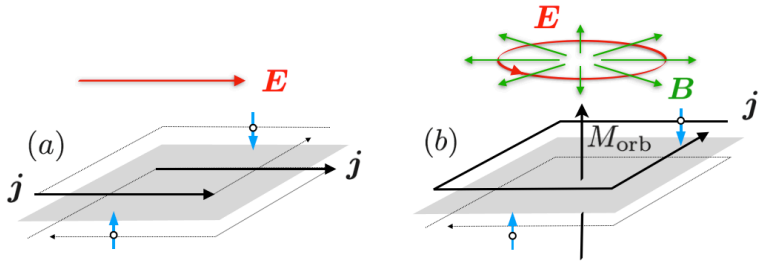

Figure 3.7: (*a*) Excitation of edge currents $\boldsymbol{j}$ with a linearly polarized laser (or a static electric field). There is no net circulating current and thus no bulk orbital magnetization. (*b*) Excitation with the cylindrical vector beam applied from the out-of-plane direction. The azimuthal electric field generates the circulating current $\boldsymbol{j}$, and thus a net orbital magnetization M_{orb} in the out-of-plane direction appears.

3.3.3 Discussion

A candidate system for the proposed measurements is a thin film of 3D topological insulators such as Bi compounds and HgTe wells [150, 151]. Although the quantum Hall insulator is the simplest topological system, the chiral nature of their edge modes may cause a complication. It is indeed interesting to see how the chiral nature of quantum Hall insulators or chiral topological superconductors affects the absorption of CVB pulses. The interplay of the azimuthal electric field and chiral modes may result in nonreciprocal response which is useful as a fingerprint of such modes.

In the above, we did not discuss the possibility of controlling metallic or superconducting rings using azimuthal CVBs, but it is definitely an interesting subject to explore. The fact that we can insert magnetic fluxes within an optical timescale with focused CVBs enables us to study the Aharonov-Bohm effect at a high-frequency region and flux-quench dynamics of superconductors.

3.4 Floquet Engineering

The highly controllable nature of CVBs would offer an ideal building block for Floquet engineering [20, 21, 22]. In Floquet engineering, we consider a system under a periodic drive with, for example, lasers. There, we are interested in the properties of such a driven system and how they can be designed at our will.

3.4.1 Floquet theory

Our concern is on the time evolution described by a time-periodic Hamiltonian $H(t) = \sum_m H_m e^{imt}$. For a time evolution over one period of the external drive $U(T,0) = \mathcal{T}_t e^{i\int_0^T H(t)dt}$, we introduce a "Floquet effective Hamiltonian" H_F as

$$U(T,0) = e^{iH_F T}, \tag{3.23}$$

Here $\mathcal{T}_t$ is the time-ordering operator, and T is the period of the external drive. When the driving frequency is sufficiently high, the Floquet-Magnus expansion of the effective Floquet Hamiltonian,

$$H_F = H_0 + \sum_{m>0} \frac{[H_{-m}, H_m]}{2m\omega} + O\left(\frac{1}{\omega^2}\right), \tag{3.24}$$

gives an approximate description for the short-time dynamics of the driven system. This effective Hamiltonian enables us to predict the nonequilibrium dynamics under the drive in an intuitive way. For example, for a Zeeman coupling between spins and a circularly polarized magnetic field, Eq. (3.24) predicts a large synthetic magnetic field which is in consistent with numerical calculations of the real-time evolution [32, 33].

The advantage of CVBs over conventional driving sources like circularly polarized beams is that we can independently control the electric and magnetic field applied to the target[4]. This is achieved by combining focused radial and azimuthal CVBs, and then we can freely vary the relative angles, phases, and amplitudes of the incident electromagnetic fields. This makes CVBs unique and powerful tools for Floquet engineering of nonequilbrium states of matters.

[4] if the target is sufficiently small compared to the wavelength

3.4.2 Floquet engineering with CVBs

Let us take a simple example, laser-induced multiferroicity [22, 36], to see this point. We consider a pair of quantum spins $\boldsymbol{S}_1$ and $\boldsymbol{S}_2$ placed along the x-axis and apply focused CVBs to them. The spins couple to magnetic fields through the Zeeman coupling:

$$H_B = -g\mu_B \cos(\omega t + \delta)(S_1^z + S_2^z)B^z, \tag{3.25}$$

where we consider a focused azimuthal CVB applied along the z-axis. We assume that spins couple to electric fields through the magneto-electric coupling of the spin current mechanism:

$$H_p = -g_{me}\boldsymbol{p} \cdot \boldsymbol{E}, \tag{3.26}$$

$$\boldsymbol{p} = \hat{x} \times (\boldsymbol{S}_1 \times \boldsymbol{S}_2). \tag{3.27}$$

We take the electric field to be in the following form: $\boldsymbol{E} = E(\cos\theta\hat{z} + \sin\theta\hat{y})\cos(\omega t)$. This is equivalent to apply a focused radial CVB in the direction $(0, \sin\theta, \cos\theta)$. We show the setup of the calculation in Fig. (3.8).

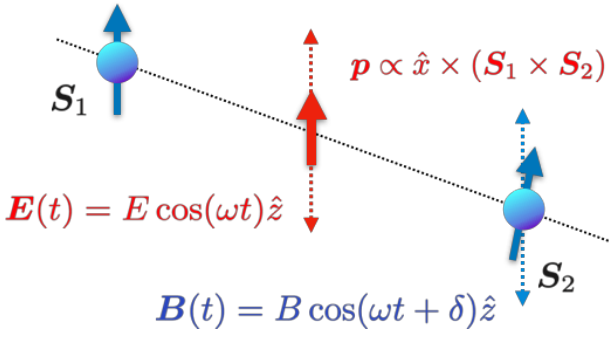

Figure 3.8: Setup of the calculation: a pair of quantum spins driven by focused radial and azimuthal CVBs.

From Eq. (3.24), the Floquet effective Hamiltonian is obtained as

$$H_F = H_0 + \frac{\sin\delta}{2\omega} g g_{me}\mu_B EB\cos\theta\,[S_1^z S_2^y - S_1^y S_2^z] + O\left(\frac{1}{\omega^2}\right). \tag{3.28}$$

We see that the periodic drive by the focused CVBs results in the synthetic DM type interaction between the spins. There is no other O$(1/\omega)$ term in the synthetic Hamiltonian, in stark contrast to the previous work [36] dealing with the same model but using circularly polarized lasers along the z axis instead. In that case, we inevitably have a synthetic Zeeman field in

addition to the DM interaction. The absence of such an additional term is advantageous from the viewpoint of Floquet engineering.

3.4.3 Numerical validation

To check whether the effective description (3.28) is consistent with the actual time evolution, below we compare Eq. (3.28) and a numerical calculation. We take a pair of $s = 1/2$ spins; $\boldsymbol{S}_1$ and $\boldsymbol{S}_2$. For simplicity, we fix $\boldsymbol{S}_1$ to $+z$ direction and ignore the time-independent terms (namely, we take $H_0 = 0$). In this case, Eq. (3.28) is reduced to be

$$H_F = \frac{\sin\delta}{4\omega} g g_{me} \mu_B E B \cos\theta S_1^y + O\left(\frac{1}{\omega^2}\right). \tag{3.29}$$

As we are not taking any dissipation into account, the time evolution would be a spin precession around the $-y$ direction if $\theta = 0$ and $\delta = \pi/2$. In this case, classically this effective Hamiltonian corresponds to an effective magnetic field in the $-y$ direction.

We take $\theta = 0$ and solve the Schrödinger equation for the time-periodic Hamiltonian

$$H(t) = -\tilde{B}\cos(\omega t + \delta) S_2^z - \tilde{E}\cos(\omega t) S_2^x. \tag{3.30}$$

Figure 3.9 presents the real-time evolution of S_2^x for $\tilde{E} = \tilde{B} = 0.1$ and $\omega = 1$. The result is consistent with the argument above. For $\delta = \pm\pi/2$, the spin precesses around $\mp y$ axis while for $\delta = 0$ it does not.

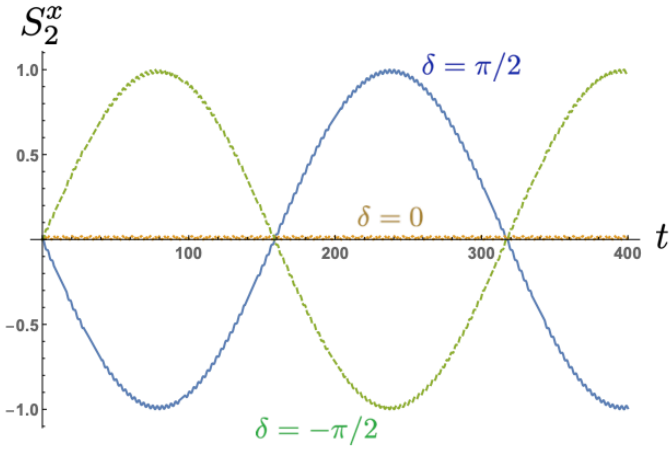

Figure 3.9: Spin precession induced by the synthetic DM term for three different values of the relative phase δ. We take $\tilde{E} = \tilde{B} = 0.1$ and $\omega = 1$.

3.5 Summary of Chapter 3

In this chapter, we considered applications of CVBs for various condensed-matter purposes. By using the longitudinal electromagnetic fields of focused CVBs, we can independently control electric and magnetic fields applied to a target. We proposed a nonequilibrium extension of magnetic oscillation measurements in a way applicable to magnetic metals or metals in a diamond anvil cell. We quantitatively discussed how small the electric-field absorption will be by using focused azimuthal CVBs and argued potential usefulness of CVBs for spectroscopic purposes. We pointed out that the azimuthal electric field offers a mean of characterizing and controlling circulating currents in topological materials which may have applications in spintronics. In the final part, we claimed that focused radial and azimuthal CVBs will be a building block of Floquet engineering of magnets.

Chapter 4

Conclusion

Lasers are becoming more and more important both scientifically and industrially. As the realization of intense ultra-short pulse lights has been an engine of the enormous success of modern science in the past decades, new technologies like teraherz optics and plasmonics will keep reinforcing our ability to understand and control matters. Optical physics, a study of light-matter interaction, will thus remain important in modern science.

In this thesis, we pushed optical physics forward by building its connection with singular (structured light) optics. In chapter 2, we showed how optical vortices could be useful for ultrafast magnetism. By using the chiral nature of optical vortices, we can excite spin waves with an unusual wave-front. Combined with the existing approach relying on designed apertures, optical excitation of spin waves with optical vortices will extend our ability to control spin waves and may lead to new functionalities of magnetic materials. As we showed, the anisotropic wave-front of spin waves hosts net scalar spin chirality. It may be an interesting future study to explore the outcome of this laser-induced spin chirality on electric transport.

The optical generation of topological defects discussed in Sec. 2.3 is also interesting. Although it would take long time before the tight subwavelength focusing of terahertz optical vortices becomes available, its realization will have a substantial impact on terahertz optical physics; we will be able to exploit the orbital angular momentum degrees of freedom for various purposes, as our result suggests. Exploring potential outcomes of the subwavelength focusing of optical vortices in the future will stimulate and propel its technological advance.

In terms of the immediate experimental feasibility, the thermal generation of topological defects discussed in Sec. 2.4 seems to have no problem at present. As we showed, heating with optical vortices allows us to nucleate general $n\pi$ vortices within an optical timescale in a systematic and

reliable manner. Since the number of available topological defects directly determines the possible recording density of information storages based on the magnetic defects, our result largely strengthens the prospect of the skyrmion-based memories as an alternative to the existing ones.

In chapter 3, we focused on cylindrical vector beams and propose their applications for characterizing and controlling electromagnetic properties of matters. The unique focusing property of azimuthal cylindrical vector beam, namely the appearance of the longitudinal magnetic field, leads to the suppression of electric-field absorptions. The drastic reduction of the heating and the electric dipole excitations will bear chances of nonequilibrium magnetic oscillation measurements applicable to (magnetic) metals (Sec. 3.1) and novel magnetic-field spectroscopy of conductors and dielectrics (Sec. 3.2). They have been difficult or totally impossible by existing methods so that experimental realizations of our proposals will have a drastic impact on the study of magnetic properties of matters in diverse fields.

We also showed that, with the azimuthal electric-field component of the beam, we may optically access circulating currents in (topological) materials (Sec. 3.3). Unlike existing methods, cylindrical vector beams can actually drive the currents and induce a net orbital magnetization to the system relying solely on the electric-field component. It is worth studying how the laser-induced orbital magnetization affects the spin degrees of freedom through a spin-orbit coupling and whether it has any spintronics applications.

The fact that we can independently control the relative amplitude, phase, and angle of electric and magnetic fields is unique to focused cylindrical vector beams. In Sec. 3.4, we argued that, due to this property, combining focused radial and azimuthal cylindrical vector beams will provide a building block of Floquet engineering of magnets. Cylindrical vector beams will thus enable us to achieve a detailed design of nonequilibrium states of matters at a level impossible with conventional light-sources.

From condensed-matter physics to biochemistry, topological lightwaves would make significant contributions by "shedding a new light" on optical properties of atoms, molecules, and solids. In this thesis, we only focused on the simplest kinds of topological lightwaves. The applications proposed in this thesis must be just the tip of the iceberg. We are at the intersection of optical physics and singular optics. This emerging field of *singular optical physics* would provide a new way of looking at both lights and matters.

Publication list

1. Accessing electromagnetic properties of matters with cylindrical vector beams, Hiroyuki Fujita, Yasuhiro Tada, Masahiro Sato, arXiv: 1811.10617

2. Floquet engineering of classical systems, Sho Higashikawa, Hiroyuki Fujita, Masahiro Sato, arXiv:1810.01103

3. Page Curves for General Interacting Systems, Hiroyuki Fujita, Yuya O. Nakagawa, Sho Sugiura, Masataka Watanabe arXiv:1805.11610

4. Universal transport and resonant current from chiral magnetic effect, Hiroyuki Fujita, Masaki Oshikawa, arXiv:1602.00687

5. Nonequilibrium Magnetic Oscillation with Cylindrical Vector Beams, Hiroyuki Fujita and Masahiro Sato, Scientific Reports **8**, 15738 (2018)

6. Construction of Hamiltonians by supervised learning of energy and entanglement spectra, Hiroyuki Fujita, Yuya. O. Nakagawa, Sho Sugiura, Masaki Oshikawa, Physical Review B **97**, 075114 (2018)

7. Universality in volume law entanglement of pure quantum states, Yuya. O. Nakagawa, Masataka Watanabe, Hiroyuki Fujita, Sho Sugiura, Nature communications **9**, 1635 (2018)

8. Field-free, spin-current control of magnetization in non-collinear chiral antiferromagnets, Hiroyuki Fujita, physica status solidi (RRL)-Rapid Research Letters **11**, No. 4, 1600360 (2017)

9. Encoding Orbital Angular Momentum of Lights in Magnets, Hiroyuki Fujita, Masahiro Sato, Physical Review B **96**, 060407 (R) (2017)

10. Ultrafast generation of skyrmionic defects with vortex beams: Printing laser profiles on magnets, Hiroyuki Fujita, Masahiro Sato, Physical Review B **95**, 054421 (2017)

11. Fractional quantum Hall states of dipolar fermions in a strained optical lattice, Hiroyuki Fujita, Yuya O. Nakagawa, Yuto Ashida, Shunsuke Furukawa, Physical Review A **94**, 043641 (2017)

12. Designing Kitaev spin liquids in metal-organic frameworks, Masahiko G. Yamada, Hiroyuki Fujita, Masaki Oshikawa, Physical Review Letters **119**, 057202 (2017)

13. Light-induced collective pseudospin precession resonating with Higgs mode in a superconductor, Ryusuke Matsunaga, Naoto Tsuji, Hiroyuki Fujita, Arata Sugioka, Kazumasa Makise, Yoshinori Uzawa, Hirotaka Terai, Zhen Wang, Hideo Aoki, Ryo Shimano, Science **345**, 1145-1149 (2014)

Bibliography

[1] A Einstein. Zur quantentheorie der strahlung. *Physikalische Zeitschrift*, 18:121–128, 1917.

[2] D. Leibfried, R. Blatt, C. Monroe, and D. Wineland. Quantum dynamics of single trapped ions. *Rev. Mod. Phys.*, 75:281–324, Mar 2003.

[3] Immanuel Bloch, Jean Dalibard, and Wilhelm Zwerger. Many-body physics with ultracold gases. *Rev. Mod. Phys.*, 80:885–964, Jul 2008.

[4] Christian Gross and Immanuel Bloch. Quantum simulations with ultracold atoms in optical lattices. *Science*, 357(6355):995–1001, 2017.

[5] M. Gring, M. Kuhnert, T. Langen, T. Kitagawa, B. Rauer, M. Schreitl, I. Mazets, D. Adu Smith, E. Demler, and J. Schmiedmayer. Relaxation and prethermalization in an isolated quantum system. *Science*, 2012.

[6] Jeff Steinhauer. Observation of quantum hawking radiation and its entanglement in an analogue black hole. *Nature Physics*, 12:959 EP –, 08 2016.

[7] Donna Strickland and Gerard Mourou. Compression of amplified chirped optical pulses. *Optics Communications*, 56(3):219 – 221, 1985.

[8] R. Stoian, D. Ashkenasi, A. Rosenfeld, and E. E. B. Campbell. Coulomb explosion in ultrashort pulsed laser ablation of Al_2O_3. *Phys. Rev. B*, 62:13167–13173, Nov 2000.

[9] Mauro Nisoli, Piero Decleva, Francesca Calegari, Alicia Palacios, and Fernando Martín. Attosecond electron dynamics in molecules. *Chemical Reviews*, 117(16):10760–10825, 2017. PMID: 28488433.

[10] M. Uiberacker, Th. Uphues, M. Schultze, A. J. Verhoef, V. Yakovlev, M. F. Kling, J. Rauschenberger, N. M. Kabachnik, H. Schröder, M. Lezius, K. L. Kompa, H. G. Muller, M. J. J. Vrakking, S. Hendel, U. Kleineberg, U. Heinzmann, M. Drescher, and F. Krausz. Attosecond real-time observation of electron tunnelling in atoms. *Nature*, 446:627 EP –, 04 2007.

[11] Masayoshi Tonouchi. Cutting-edge terahertz technology. *Nature Photonics*, 1:97 EP –, 02 2007.

[12] S S Dhillon, M S Vitiello, E H Linfield, A G Davies, Matthias C Hoffmann, John Booske, Claudio Paoloni, M Gensch, P Weightman, G P Williams, E Castro-Camus, D R S Cumming, F Simoens, I Escorcia-Carranza, J Grant, Stepan Lucyszyn, Makoto Kuwata-Gonokami, Kuniaki Konishi, Martin Koch, Charles A Schmuttenmaer, Tyler L Cocker, Rupert Huber, A G Markelz, Z D Taylor, Vincent P Wallace, J Axel Zeitler, Juraj Sibik, Timothy M Korter, B Ellison, S Rea, P Goldsmith, Ken B Cooper, Roger Appleby, D Pardo, P G Huggard, V Krozer, Haymen Shams, Martyn Fice, Cyril Renaud, Alwyn Seeds, Andreas Stöhr, Mira Naftaly, Nick Ridler, Roland Clarke, John E Cunningham, and Michael B Johnston. The 2017 terahertz science and technology roadmap. *Journal of Physics D: Applied Physics*, 50(4):043001, 2017.

[13] Koichi Katsumata. High-frequency electron spin resonance in magnetic systems. *Journal of Physics: Condensed Matter*, 12(47):R589, 2000.

[14] Y Mukai, H Hirori, T Yamamoto, H Kageyama, and K Tanaka. Nonlinear magnetization dynamics of antiferromagnetic spin resonance induced by intense terahertz magnetic field. *New J. Phys.*, 18(1):013045, 2016.

[15] Tobias Kampfrath, Alexander Sell, Gregor Klatt, Alexej Pashkin, Sebastian Mahrlein, Thomas Dekorsy, Martin Wolf, Manfred Fiebig, Alfred Leitenstorfer, and Rupert Huber. Coherent terahertz control of antiferromagnetic spin waves. *Nat. Photon.*, 5(1):31–34, 01 2011.

[16] Zuanming Jin, Zoltán Mics, Guohong Ma, Zhenxiang Cheng, Mischa Bonn, and Dmitry Turchinovich. Single-pulse terahertz coherent control of spin resonance in the canted antiferromagnet $YFeO_3$, mediated by dielectric anisotropy. *Phys. Rev. B*, 87:094422, Mar 2013.

[17] Ryusuke Matsunaga, Naoto Tsuji, Hiroyuki Fujita, Arata Sugioka, Kazumasa Makise, Yoshinori Uzawa, Hirotaka Terai, Zhen Wang, Hideo Aoki, and Ryo Shimano. Light-induced collective pseudospin precession resonating with Higgs mode in a superconductor. *Science*, 345(6201):1145–1149, 2014.

[18] Ryusuke Matsunaga, Yuki I. Hamada, Kazumasa Makise, Yoshinori Uzawa, Hirotaka Terai, Zhen Wang, and Ryo Shimano. Higgs Amplitude Mode in the BCS Superconductors $Nb_{1-x}Ti_xN$ Induced by Terahertz Pulse Excitation. *Phys. Rev. Lett.*, 111:057002, Jul 2013.

[19] Ryogo Kubo and Kazuhisa Tomita. A General Theory of Magnetic Resonance Absorption. *Journal of the Physical Society of Japan*, 9(6):888–919, 2018/05/17 1954.

[20] Marin Bukov, Luca D'Alessio, and Anatoli Polkovnikov. Universal high-frequency behavior of periodically driven systems: from dynamical stabilization to floquet engineering. *Advances in Physics*, 64(2):139–226, 2015.

[21] Takashi Oka and Sota Kitamura. Floquet engineering of quantum materials. *arXiv:1804.03212*, 2018.

[22] Sho Higashikawa, Hiroyuki Fujita, and Masahiro Sato. Floquet engineering of classical systems. *arXiv:1810.01103*, 2018.

[23] A J Daley, C Kollath, U Schollwöck, and G Vidal. Time-dependent density-matrix renormalization-group using adaptive effective hilbert spaces. *Journal of Statistical Mechanics: Theory and Experiment*, 2004(04):P04005, 2004.

[24] Takashi Oka and Hideo Aoki. Photovoltaic hall effect in graphene. *Phys. Rev. B*, 79:081406, Feb 2009.

[25] Takahiro Mikami, Sota Kitamura, Kenji Yasuda, Naoto Tsuji, Takashi Oka, and Hideo Aoki. Brillouin-wigner theory for high-frequency expansion in periodically driven systems: Application to floquet topological insulators. *Phys. Rev. B*, 93:144307, Apr 2016.

[26] Satoru Sugano and Norimichi Kojima, editors. *Magneto-Optics*. Springer, 2000.

[27] E. Beaurepaire, J.-C. Merle, A. Daunois, and J.-Y. Bigot. Ultrafast spin dynamics in ferromagnetic nickel. *Phys. Rev. Lett.*, 76:4250–4253, May 1996.

[28] Andrei Kirilyuk, Alexey V. Kimel, and Theo Rasing. Ultrafast optical manipulation of magnetic order. *Rev. Mod. Phys.*, 82:2731–2784, Sep 2010.

[29] Tian-Min Liu, Tianhan Wang, Alexander H. Reid, Matteo Savoini, Xiaofei Wu, Benny Koene, Patrick Granitzka, Catherine E. Graves, Daniel J. Higley, Zhao Chen, Gary Razinskas, Markus Hantschmann, Andreas Scherz, Joachim Stöhr, Arata Tsukamoto, Bert Hecht, Alexey V. Kimel, Andrei Kirilyuk, Theo Rasing, and Hermann A. Dürr. Nanoscale Confinement of All-Optical Magnetic Switching in TbFeCo - Competition with Nanoscale Heterogeneity. *Nano Lett.*, 15(10):6862–6868, 2015. PMID: 26312732.

[30] S. Mangin, M. Gottwald, C-H. Lambert, D. Steil, V. Uhlíř, L. Pang, M. Hehn, S. Alebrand, M. Cinchetti, G. Malinowski, Y. Fainman, M. Aeschlimann, and E. E. Fullerton. Engineered materials for all-optical helicity-dependent magnetic switching. *Nat. Mater.*, 13(3):286–292, 03 2014.

[31] C. D. Stanciu, F. Hansteen, A. V. Kimel, A. Kirilyuk, A. Tsukamoto, A. Itoh, and Th. Rasing. All-optical magnetic recording with circularly polarized light. *Phys. Rev. Lett.*, 99:047601, Jul 2007.

[32] Shintaro Takayoshi, Hideo Aoki, and Takashi Oka. Magnetization and phase transition induced by circularly polarized laser in quantum magnets. *Phys. Rev. B*, 90(085150):085150, Aug 2014.

[33] Shintaro Takayoshi, Masahiro Sato, and Takashi Oka. Laser-induced magnetization curve. *Phys. Rev. B*, 90:214413, Dec 2014.

[34] Jérôme Hurst, Paul-Antoine Hervieux, and Giovanni Manfredi. Spin current generation by ultrafast laser pulses in ferromagnetic nickel films. *Phys. Rev. B*, 97:014424, Jan 2018.

[35] A Fognini, T U Michlmayr, A Vaterlaus, and Y Acremann. Laser-induced ultrafast spin current pulses: a thermodynamic approach. *Journal of Physics: Condensed Matter*, 29(21):214002, 2017.

[36] Masahiro Sato, Shintaro Takayoshi, and Takashi Oka. Laser-Driven Multiferroics and Ultrafast Spin Current Generation. *Phys. Rev. Lett.*, 117:147202, 2016.

[37] Yoshinori Tokura, Shinichiro Seki, and Naoto Nagaosa. Multiferroics of spin origin. *Rep. Prog. Phys.*, 77(7):076501, 2014.

[38] Sang-Wook Cheong and Maxim Mostovoy. Multiferroics: a magnetic twist for ferroelectricity. *Nat. Mater.*, 6(1):13–20, 01 2007.

[39] Masahito Mochizuki and Naoto Nagaosa. Theoretically Predicted Picosecond Optical Switching of Spin Chirality in Multiferroics. *Phys. Rev. Lett.*, 105:147202, Sep 2010.

[40] Kazuaki Takasan, Akito Daido, Norio Kawakami, and Youichi Yanase. Laser-induced topological superconductivity in cuprate thin films. *Phys. Rev. B*, 95:134508, Apr 2017.

[41] Masahiro Sato, Yuki Sasaki, and Takashi Oka. Floquet Majorana Edge Mode and Non-Abelian Anyons in a Driven Kitaev Model. *arXiv:1404.2010*, 2014.

[42] David L. Andrews and Mohamed Babiker, editors. *The Angular Momentum of Light*. Cambridge University Press, 2012. Cambridge Books Online.

[43] L. Allen, M. W. Beijersbergen, R. J. C. Spreeuw, and J. P. Woerdman. Orbital angular momentum of light and the transformation of Laguerre-Gaussian laser modes. *Phys. Rev. A*, 45:8185–8189, Jun 1992.

[44] J. Courtial, K. Dholakia, L. Allen, and M. J. Padgett. Gaussian beams with very high orbital angular momentum. *Opt. Communications*, 144(4):210–213, 1997.

[45] A. T. O'Neil, I. MacVicar, L. Allen, and M. J. Padgett. Intrinsic and Extrinsic Nature of the Orbital Angular Momentum of a Light Beam. *Phys. Rev. Lett.*, 88:053601, Jan 2002.

[46] J. Bahrdt, K. Holldack, P. Kuske, R. Müller, M. Scheer, and P. Schmid. First observation of photons carrying orbital angular momentum in undulator radiation. *Phys. Rev. Lett.*, 111:034801, Jul 2013.

[47] Ebrahim Karimi, Sebastian A Schulz, Israel De Leon, Hammam Qassim, Jeremy Upham, and Robert W Boyd. Generating optical orbital angular momentum at visible wavelengths using a plasmonic metasurface. *Light: Science &Amp; Applications*, 3:e167 EP –, 05 2014.

[48] L Paterson, M P MacDonald, Jochen Arlt, W Sibbett, P E Bryant, and K Dholakia. Controlled rotation of optically trapped microscopic particles. *Science*, 292(5518):912–914, 2001.

[49] M. F. Andersen, C. Ryu, Pierre Cladé, Vasant Natarajan, A. Vaziri, K. Helmerson, and W. D. Phillips. Quantized Rotation of Atoms from Photons with Orbital Angular Momentum. *Phys. Rev. Lett.*, 97:170406, Oct 2006.

[50] Stefan Bretschneider, Christian Eggeling, and Stefan W. Hell. Breaking the Diffraction Barrier in Fluorescence Microscopy by Optical Shelving. *Phys. Rev. Lett.*, 98:218103, May 2007.

[51] Junichi Hamazaki, Ryuji Morita, Keisuke Chujo, Yusuke Kobayashi, Satoshi Tanda, and Takashige Omatsu. Optical-vortex laser ablation. *Opt. Express*, 18(3):2144–2151, Feb 2010.

[52] Takashige Omatsu, Keisuke Chujo, Katsuhiko Miyamoto, Masahito Okida, Kazuki Nakamura, Nobuyuki Aoki, and Ryuji Morita. Metal microneedle fabrication using twisted light with spin. *Opt. Express*, 18(17):17967–17973, Aug 2010.

[53] Fuyuto Takahashi, Kohei Toyoda, Shun Takizawa, Katsuhiko Miyamoto, Ryuji Morita, and Takashige Omatsu. Chiral structure control of metal nano-needles fabrictaed by optical vortex laser ablation. In *CLEO: 2013*, page CM3H.6. Optical Society of America, 2013.

[54] Stefan W. Hell. Nobel lecture: Nanoscopy with freely propagating light. *Rev. Mod. Phys.*, 87:1169–1181, Oct 2015.

[55] Nenad Bozinovic, Yang Yue, Yongxiong Ren, Moshe Tur, Poul Kristensen, Hao Huang, Alan E. Willner, and Siddharth Ramachandran. Terabit-scale orbital angular momentum mode division multiplexing in fibers. *Science*, 340(6140):1545–1548, 2013.

[56] Kohei Toyoda, Katsuhiko Miyamoto, Nobuyuki Aoki, Ryuji Morita, and Takashige Omatsu. Using Optical Vortex To Control the Chirality of Twisted Metal Nanostructures. *Nano Lett.*, 12(7):3645–3649, 07 2012.

[57] Qiwen Zhan. Cylindrical vector beams: from mathematical concepts to applications. *Adv. Opt. Photon.*, 1(1):1–57, Jan 2009.

[58] K. S. Youngworth and T. G Brown. Focusing of high numerical aperture cylindrical-vector beams. *Opt. Express*, 7(2):77–87, Jul 2000.

[59] Qiwen Zhan and James R. Leger. Focus shaping using cylindrical vector beams. *Opt. Express*, 10(7):324–331, Apr 2002.

[60] B. Richards, E. Wolf, and Dennis Gabor. Electromagnetic diffraction in optical systems, ii. structure of the image field in an aplanatic system. *Proceedings of the Royal Society of London A: Mathematical, Physical and Engineering Sciences*, 253(1274):358–379, 1959.

[61] Hiroyuki Fujita and Masahiro Sato. Ultrafast generation of skyrmionic defects with vortex beams: Printing laser profiles on magnets. *Phys. Rev. B*, 95:054421, Feb 2017.

[62] Hiroyuki Fujita and Masahiro Sato. Encoding orbital angular momentum of light in magnets. *Phys. Rev. B*, 96:060407, Aug 2017.

[63] Hiroyuki Fujita and Masahiro Sato. Nonequilibrium magnetic oscillation with cylindrical vector beams. *Scientific Reports*, 8(1):15738, 2018.

[64] Hiroyuki Fujita, Yasuhiro Tada, and Masahiro Sato. Accessing electromagnetic properties of matter with cylindrical vector beams. *arXiv: 1811.10617*, 2018.

[65] I. Dzyaloshinsky. A thermodynamic theory of "weak" ferromagnetism of antiferromagnetics. *J. Phys. Chem. Solids*, 4(4):241 – 255, 1958.

[66] Tôru Moriya. Anisotropic Superexchange Interaction and Weak Ferromagnetism. *Phys. Rev.*, 120:91–98, Oct 1960.

[67] Masahito Mochizuki. Spin-Wave Modes and Their Intense Excitation Effects in Skyrmion Crystals. *Phys. Rev. Lett.*, 108:017601, Jan 2012.

[68] T. Jeong and W. E. Pickett. Implications of the B20 crystal structure for the magnetoelectronic structure of MnSi. *Phys. Rev. B*, 70:075114, Aug 2004.

[69] S. Mühlbauer, B. Binz, F. Jonietz, C. Pfleiderer, A. Rosch, A. Neubauer, R. Georgii, and P. Böni. Skyrmion Lattice in a Chiral Magnet. *Science*, 323(5916):915–919, 02 2009.

[70] A. Neubauer, C. Pfleiderer, B. Binz, A. Rosch, R. Ritz, P. G. Niklowitz, and P. Böni. Topological Hall Effect in the *A* Phase of MnSi. *Phys. Rev. Lett.*, 102:186602, May 2009.

[71] C. Pappas, E. Lelièvre-Berna, P. Falus, P. M. Bentley, E. Moskvin, S. Grigoriev, P. Fouquet, and B. Farago. Chiral Paramagnetic Skyrmion-like Phase in MnSi. *Phys. Rev. Lett.*, 102:197202, May 2009.

[72] X. Z. Yu, Y. Onose, N. Kanazawa, J. H. Park, J. H. Han, Y. Matsui, N. Nagaosa, and Y. Tokura. Real-space observation of a two-dimensional skyrmion crystal. *Nature*, 465(7300):901–904, 06 2010.

[73] W. Münzer, A. Neubauer, T. Adams, S. Mühlbauer, C. Franz, F. Jonietz, R. Georgii, P. Böni, B. Pedersen, M. Schmidt, A. Rosch, and C. Pfleiderer. Skyrmion lattice in the doped semiconductor $Fe_{1-x}Co_xSi$. *Phys. Rev. B*, 81:041203, Jan 2010.

[74] X. Z. Yu, N. Kanazawa, Y. Onose, K. Kimoto, W. Z. Zhang, S. Ishiwata, Y. Matsui, and Y. Tokura. Near room-temperature formation of a skyrmion crystal in thin-films of the helimagnet FeGe. *Nat. Mater.*, 10(2):106–109, 02 2011.

[75] S. X. Huang and C. L. Chien. Extended Skyrmion Phase in Epitaxial FeGe(111) Thin Films. *Phys. Rev. Lett.*, 108:267201, Jun 2012.

[76] Seonghoon Woo, Kai Litzius, Benjamin Kruger, Mi-Young Im, Lucas Caretta, Kornel Richter, Maxwell Mann, Andrea Krone, Robert M. Reeve, Markus Weigand, Parnika Agrawal, Ivan Lemesh, Mohamad-Assaad Mawass, Peter Fischer, Mathias Klaui, and Geoffrey S. D. Beach. Observation of room-temperature magnetic skyrmions and their current-driven dynamics in ultrathin metallic ferromagnets. *Nat. Mater.*, 15(5):501–506, 05 2016.

[77] S. Seki and M. Mochizuki. *Skyrmions in Magnetic Materials*. Springer, 2016.

[78] A Bogdanov and A Hubert. Thermodynamically stable magnetic vortex states in magnetic crystals. *J. Magn. Magn. Mater.*, 138:255–269, 1994.

[79] A Bogdanov and A Hubert. The stability of vortex-like structures in uniaxial ferromagnets. *J. Magn. Magn. Mater.*, 195(1):182–192, 1999.

[80] M. Finazzi, M. Savoini, A. R. Khorsand, A. Tsukamoto, A. Itoh, L. Duò, A. Kirilyuk, Th. Rasing, and M. Ezawa. Laser-Induced

Magnetic Nanostructures with Tunable Topological Properties. *Phys. Rev. Lett.*, 110:177205, Apr 2013.

[81] Stavros Komineas and Nikos Papanicolaou. Skyrmion dynamics in chiral ferromagnets. *Phys. Rev. B*, 92:064412, Aug 2015.

[82] Xichao Zhang, Jing Xia, Yan Zhou, Daowei Wang, Xiaoxi Liu, Weisheng Zhao, and Motohiko Ezawa. Control and manipulation of a magnetic skyrmionium in nanostructures. *Phys. Rev. B*, 94:094420, Sep 2016.

[83] Shilei Zhang, Florian Kronast, Gerrit van der Laan, and Thorsten Hesjedal. Real-space observation of skyrmionium in a ferromagnet-magnetic topological insulator heterostructure. *Nano Letters*, 18(2):1057–1063, 2018. PMID: 29363315.

[84] T. Arima. Ferroelectricity induced by proper-screw type magnetic order. *J. Phys. Soc. Jpn.*, 76(7):073702, 2016/11/23 2007.

[85] Hosho Katsura, Naoto Nagaosa, and Alexander V. Balatsky. Spin Current and Magnetoelectric Effect in Noncollinear Magnets. *Phys. Rev. Lett.*, 95:057205, Jul 2005.

[86] Chenglong Jia, Shigeki Onoda, Naoto Nagaosa, and Jung Hoon Han. Microscopic theory of spin-polarization coupling in multiferroic transition metal oxides. *Phys. Rev. B*, 76:144424, Oct 2007.

[87] Masahito Mochizuki, Nobuo Furukawa, and Naoto Nagaosa. Theory of Electromagnons in the Multiferroic Mn Perovskites: The Vital Role of Higher Harmonic Components of the Spiral Spin Order. *Phys. Rev. Lett.*, 104:177206, Apr 2010.

[88] S. Seki, S. Ishiwata, and Y. Tokura. Magnetoelectric nature of skyrmions in a chiral magnetic insulator Cu_2OSeO_3. *Phys. Rev. B*, 86:060403, Aug 2012.

[89] Bernd Terhalle, Andreas Langner, Birgit Päivänranta, Vitaliy A. Guzenko, Christian David, and Yasin Ekinci. Generation of extreme ultraviolet vortex beams using computer generated holograms. *Opt. Lett.*, 36(21):4143–4145, Nov 2011.

[90] Carlos Hernández-García, Antonio Picón, Julio San Román, and Luis Plaja. Attosecond Extreme Ultraviolet Vortices from High-Order Harmonic Generation. *Phys. Rev. Lett.*, 111:083602, Aug 2013.

[91] G. Alexander Gurevich and A. Gennadii Melkov. *Magnetization Oscillations and Waves*. CRC Press, 1996.

[92] D. Daniel Stancil and Anil Prabhankar. *Spin Waves*. Springer US, 2009.

[93] Wanjun Jiang, Xichao Zhang, Guoqiang Yu, Wei Zhang, Xiao Wang, M. Benjamin Jungfleisch, John E. Pearson, Xuemei Cheng, Olle Heinonen, Kang L. Wang, Yan Zhou, Axel Hoffmann, and Suzanne G. E. te Velthuis. Direct observation of the skyrmion hall effect. *Nature Phys.*, 13(2):162—169, 09 2017.

[94] Yuki Shiomi. *Topological Hall Effect in Itinerant Helimagnets*. Springer Japan, Tokyo, 2013.

[95] Takuya Satoh, Yuki Terui, Rai Moriya, Boris A. Ivanov, Kazuya Ando, Eiji Saitoh, Tsutomu Shimura, and Kazuo Kuroda. Directional control of spin-wave emission by spatially shaped light. *Nat. Photon.*, 6(10):662–666, 10 2012.

[96] Yusuke Hashimoto, Shunsuke Daimon, Ryo Iguchi, Yasuyuki Oikawa, Ka Shen, Koji Sato, Davide Bossini, Yutaka Tabuchi, Takuya Satoh, Burkard Hillebrands, Gerrit E. W. Bauer, Tom H. Johansen, Andrei Kirilyuk, Theo Rasing, and Eiji Saitoh. All-optical observation and reconstruction of spin wave dispersion. *Nat. Commun.*, 8:15859, 06 2017.

[97] Reinier W. Heeres and Valery Zwiller. Subwavelength focusing of light with orbital angular momentum. *Nano Lett.*, 14(8):4598–4601, 08 2014.

[98] Dmitri K. Gramotnev and Sergey I. Bozhevolnyi. Plasmonics beyond the diffraction limit. *Nat. Photon.*, 4(2):83–91, 02 2010.

[99] Prabhat Verma. Tip-enhanced raman spectroscopy: Technique and recent advances. *Chemical Reviews*, 117(9):6447–6466, 2017. PMID: 28459149.

[100] Willie J. Padilla, Dimitri N. Basov, and David R. Smith. Negative refractive index metamaterials. *Materials Today*, 9(7):28 – 35, 2006.

[101] Takashi Arikawa, Shohei Morimoto, and Koichiro Tanaka. Focusing light with orbital angular momentum by circular array antenna. *Opt. Express*, 25(12):13728–13735, Jun 2017.

[102] Masahito Mochizuki. Creation of Skyrmions by Electric Field on Chiral-Lattice Magnetic Insulators. *Advanced Electronic Materials*, 2(1), 2016. 1500180.

[103] Wataru Koshibae and Naoto Nagaosa. Creation of skyrmions and antiskyrmions by local heating. *Nat. Commun.*, 5(5148):5148, 10 2014.

[104] Agustín Salazar. On thermal diffusivity. *European Journal of Physics*, 24(4):351, 2003.

[105] José Luis García-Palacios and Francisco J. Lázaro. Langevin-dynamics study of the dynamical properties of small magnetic particles. *Phys. Rev. B*, 58:14937–14958, Dec 1998.

[106] Masamichi Nishino and Seiji Miyashita. Realization of the thermal equilibrium in inhomogeneous magnetic systems by the Landau-Lifshitz-Gilbert equation with stochastic noise, and its dynamical aspects. *Phys. Rev. B*, 91:134411, Apr 2015.

[107] M. Mochizuki, X. Z. Yu, S. Seki, N. Kanazawa, W. Koshibae, J. Zang, M. Mostovoy, Y. Tokura, and N. Nagaosa. Thermally driven ratchet motion of a skyrmion microcrystal and topological magnon Hall effect. *Nat. Mater.*, 13(3):241–246, 03 2014.

[108] Xichao Zhang, Yan Zhou, and Motohiko Ezawa. Antiferromagnetic Skyrmion: Stability, Creation and Manipulation. *Sci. Rep.*, 6, 04 2016.

[109] N.W. Ashcroft and N.D. Mermin. *Solid State Physics*. Saunders College, Philadelphia, 1976.

[110] C. Kittel. *Introduction to Solid State Physics*. Wiley, 2004.

[111] G. Li, Z. Xiang, F. Yu, T. Asaba, B. Lawson, P. Cai, C. Tinsman, A. Berkley, S. Wolgast, Y. S. Eo, Dae-Jeong Kim, C. Kurdak, J. W. Allen, K. Sun, X. H. Chen, Y. Y. Wang, Z. Fisk, and Lu Li. Two-dimensional Fermi surfaces in Kondo insulator SmB6. *Science*, 346(6214):1208–1212, 2014.

[112] B. S. Tan, Y.-T. Hsu, B. Zeng, M. Ciomaga Hatnean, N. Harrison, Z. Zhu, M. Hartstein, M. Kiourlappou, A. Srivastava, M. D. Johannes, T. P. Murphy, J.-H. Park, L. Balicas, G. G. Lonzarich, G. Balakrishnan, and Suchitra E. Sebastian. Unconventional fermi surface in an insulating state. *Science*, 349(6245):287–290, 2015.

[113] Zengwei Zhu, Xiao Lin, Juan Liu, Benoît Fauqué, Qian Tao, Chongli Yang, Youguo Shi, and Kamran Behnia. Quantum Oscillations, Thermoelectric Coefficients, and the Fermi Surface of Semimetallic WTe_2. *Phys. Rev. Lett.*, 114:176601, Apr 2015.

[114] Likai Li, Guo Jun Ye, Vy Tran, Ruixiang Fei, Guorui Chen, Huichao Wang, Jian Wang, Kenji Watanabe, Takashi Taniguchi, Li Yang, Xian Hui Chen, and Yuanbo Zhang. Quantum oscillations in a two-dimensional electron gas in black phosphorus thin films. *Nat. Nanotechnol.*, 10:608 EP –, 05 2015.

[115] Xiaolong Chen, Yingying Wu, Zefei Wu, Yu Han, Shuigang Xu, Lin Wang, Weiguang Ye, Tianyi Han, Yuheng He, Yuan Cai, and Ning Wang. High-quality sandwiched black phosphorus heterostructure and its quantum oscillations. *Nat. Commun.*, 6:7315 EP –, 06 2015.

[116] P. L. Cai, J. Hu, L. P. He, J. Pan, X. C. Hong, Z. Zhang, J. Zhang, J. Wei, Z. Q. Mao, and S. Y. Li. Drastic Pressure Effect on the Extremely Large Magnetoresistance in WTe_2: Quantum Oscillation Study. *Phys. Rev. Lett.*, 115:057202, Jul 2015.

[117] M. Ben Shalom, M. J. Zhu, V. I. Fal'ko, A. Mishchenko, A. V. Kretinin, K. S. Novoselov, C. R. Woods, K. Watanabe, T. Taniguchi, A. K. Geim, and J. R. Prance. Quantum oscillations of the critical current and high-field superconducting proximity in ballistic graphene. *Nat. Phys.*, 12:318 EP –, 12 2015.

[118] Onur Erten, Pouyan Ghaemi, and Piers Coleman. Kondo Breakdown and Quantum Oscillations in SmB_6. *Phys. Rev. Lett.*, 116:046403, Jan 2016.

[119] Nicholas P. Breznay, Ian M. Hayes, B. J. Ramshaw, Ross D. McDonald, Yoshiharu Krockenberger, Ai Ikeda, Hiroshi Irie, Hideki Yamamoto, and James G. Analytis. Shubnikov-de Haas quantum oscillations reveal a reconstructed Fermi surface near optimal doping in a thin film of the cuprate superconductor $Pr_{1.86}Ce_{0.14}CuO_{4\pm\delta}$. *Phys. Rev. B*, 94:104514, Sep 2016.

[120] Jinxiong Wu, Hongtao Yuan, Mengmeng Meng, Cheng Chen, Yan Sun, Zhuoyu Chen, Wenhui Dang, Congwei Tan, Yujing Liu, Jianbo Yin, Yubing Zhou, Shaoyun Huang, H. Q. Xu, Yi Cui, Harold Y. Hwang, Zhongfan Liu, Yulin Chen, Binghai Yan, and Hailin Peng. High electron mobility and quantum oscillations in non-encapsulated

ultrathin semiconducting bi2o2se. *Nat. Nanotechnol.*, 12:530 EP –, 04 2017.

[121] Wan Kyu Park, Lunan Sun, Alexander Noddings, Dae-Jeong Kim, Zachary Fisk, and Laura H. Greene. Topological surface states interacting with bulk excitations in the kondo insulator smb6 revealed via planar tunneling spectroscopy. *Proc. Natl. Acad. Sci. USA*, 113(24):6599–6604, 2016.

[122] Y. Xu, S. Cui, J. K. Dong, D. Zhao, T. Wu, X. H. Chen, Kai Sun, Hong Yao, and S. Y. Li. Bulk Fermi Surface of Charge-Neutral Excitations in SmB_6 or Not: A Heat-Transport Study. *Phys. Rev. Lett.*, 116:246403, Jun 2016.

[123] P. Coleman, E. Miranda, and A. Tsvelik. Are Kondo insulators gapless? *Physica B: Condensed Matter*, 186-188:362–364, 1993.

[124] Debanjan Chowdhury, Inti Sodemann, and T. Senthil. Mixed-valence insulators with neutral fermi-surfaces. *arXiv:1706.00418*, 2017.

[125] Johannes Knolle and Nigel R. Cooper. Excitons in topological Kondo insulators: Theory of thermodynamic and transport anomalies in SmB_6. *Phys. Rev. Lett.*, 118:096604, Mar 2017.

[126] Onur Erten, Po-Yao Chang, Piers Coleman, and Alexei M. Tsvelik. Skyrme Insulators: Insulators at the Brink of Superconductivity. *Phys. Rev. Lett.*, 119:057603, Aug 2017.

[127] Zhaoming Tian, Yoshimitsu Kohama, Takahiro Tomita, Hiroaki Ishizuka, Timothy H. Hsieh, Jun J. Ishikawa, Koichi Kindo, Leon Balents, and Satoru Nakatsuji. Field-induced quantum metal–insulator transition in the pyrochlore iridate nd2ir2o7. *Nat. Phys.*, 12:134 EP –, 11 2015.

[128] Kentaro Ueda, Taekoo Oh, Bohm-Jung Yang, Ryoma Kaneko, Jun Fujioka, Naoto Nagaosa, and Yoshinori Tokura. Magnetic-field induced multiple topological phases in pyrochlore iridates with mott criticality. *Nat. Commun.*, 8:15515 EP –, 05 2017.

[129] R. Meservey and P. M. Tedrow. Surface Relaxation Times of Conduction-Electron Spins in Superconductors and Normal Metals. *Phys. Rev. Lett.*, 41:805–808, Sep 1978.

[130] K. Lenz, H. Wende, W. Kuch, K. Baberschke, K. Nagy, and A. Jánossy. Two-magnon scattering and viscous gilbert damping in ultrathin ferromagnets. *Phys. Rev. B*, 73:144424, Apr 2006.

[131] Gang Chen and Michael Hermele. Magnetic orders and topological phases from f-d exchange in pyrochlore iridates. *Phys. Rev. B*, 86:235129, Dec 2012.

[132] Clarence Zener. Interaction between the d-shells in the transition metals. ii. ferromagnetic compounds of manganese with perovskite structure. *Phys. Rev.*, 82:403–405, May 1951.

[133] P. W. Anderson and H. Hasegawa. Considerations on double exchange. *Phys. Rev.*, 100:675–681, Oct 1955.

[134] Keita Kishigi and Yasumasa Hasegawa. de haas–van alphen effect in two-dimensional and quasi-two-dimensional systems. *Phys. Rev. B*, 65:205405, May 2002.

[135] A. Jayaraman. Diamond anvil cell and high-pressure physical investigations. *Rev. Mod. Phys.*, 55:65–108, Jan 1983.

[136] Nicholas R. Brewer, Zachary N. Buckholtz, Zachary J. Simmons, Eli A. Mueller, and Deniz D. Yavuz. Coherent magnetic response at optical frequencies using atomic transitions. *Phys. Rev. X*, 7:011005, Jan 2017.

[137] The Editors of Encyclopædia Britannica, editor. *Semiconductor*. Encyclopædia Britannica, inc., 2018.

[138] Adrien Bolens, Hosho Katsura, Masao Ogata, and Seiji Miyashita. Synergetic effect of spin-orbit coupling and Zeeman splitting on the optical conductivity in the one-dimensional Hubbard model. *Phys. Rev. B*, 95:235115, Jun 2017.

[139] Youtarou Takahashi, Ryo Shimano, Yoshio Kaneko, Hiroshi Murakawa, and Yoshinori Tokura. Magnetoelectric resonance with electromagnons in a perovskite helimagnet. *Nature Phys.*, 8(2):121–125, 02 2012.

[140] Jeschke Gunnar. Determination of the Nanostructure of Polymer Materials by Electron Paramagnetic Resonance Spectroscopy. *Macromolecular Rapid Communications*, 23(4):227–246, 2002.

[141] J.A. Weil and J.R. Bolton. *Electron Paramagnetic Resonance: Elementary Theory and Practical Applications*. Wiley, 2007.

[142] B. Halliwell and J. M. C. Gutteridge. *Free Radicals in Biology and Medicine*. Oxford University Press, 2015.

[143] O. Grinberg and L.J. Berliner. *Very High Frequency (VHF) ESR/EPR*. Biological Magnetic Resonance. Springer US, 2013.

[144] Kálmán L. Nagy, Dario Quintavalle, Titusz Fehér, and András Jánossy. Multipurpose High-Frequency ESR Spectrometer for Condensed Matter Research. *Applied Magnetic Resonance*, 40(1):47–63, 2011.

[145] Daniel M. Chipman. Excited electronic states of small water clusters. *The Journal of Chemical Physics*, 122(044111), 2005.

[146] Anne Laure Barra, Dante Gatteschi, and Roberta Sessoli. High-frequency EPR spectra of a molecular nanomagnet: Understanding quantum tunneling of the magnetization. *Phys. Rev. B*, 56:8192–8198, Oct 1997.

[147] R. S. Edwards, S. Maccagnano, E. C. Yang, S. Hill, W. Wernsdorfer, D. Hendrickson, and G. Christou. High-frequency electron paramagnetic resonance investigations of tetranuclear nickel-based single-molecule magnets. *Journal of Applied Physics*, 93(10):7807–7809, 2018/08/31 2003.

[148] En-Che Yang, Cem Kirman, Jon Lawrence, Lev N. Zakharov, Arnold L. Rheingold, Stephen Hill, and David N. Hendrickson. Single-Molecule Magnets: High-Field Electron Paramagnetic Resonance Evaluation of the Single-Ion Zero-Field Interaction in a ZnII3NiII Complex. *Inorganic Chemistry*, 44(11):3827–3836, 05 2005.

[149] Katie E. R. Marriott, Lakshmi Bhaskaran, Claire Wilson, Marisa Medarde, Stefan T. Ochsenbein, Stephen Hill, and Mark Murrie. Pushing the limits of magnetic anisotropy in trigonal bipyramidal ni(ii). *Chem. Sci.*, 6:6823–6828, 2015.

[150] Xiao-Liang Qi and Shou-Cheng Zhang. Topological insulators and superconductors. *Rev. Mod. Phys.*, 83:1057–1110, Oct 2011.

[151] M. Z. Hasan and C. L. Kane. Colloquium: Topological insulators. *Rev. Mod. Phys.*, 82:3045–3067, Nov 2010.

[152] Andreas Roth, Christoph Brüne, Hartmut Buhmann, Laurens W. Molenkamp, Joseph Maciejko, Xiao-Liang Qi, and Shou-Cheng Zhang. Nonlocal transport in the quantum spin hall state. *Science*, 325(5938):294–297, 2009.

[153] Wen-Jie Chen, Shao-Ji Jiang, Xiao-Dong Chen, Baocheng Zhu, Lei Zhou, Jian-Wen Dong, and C. T. Chan. Experimental realization of photonic topological insulator in a uniaxial metacrystal waveguide. *Nature Communications*, 5:5782 EP –, 12 2014.

[154] Roman Süsstrunk and Sebastian D. Huber. Observation of phononic helical edge states in a mechanical topological insulator. *Science*, 349(6243):47, 07 2015.

[155] H. Ito, K. Furuya, Y. Shibata, S. Kashiwaya, M. Yamaguchi, T. Akazaki, H. Tamura, Y. Ootuka, and S. Nomura. Near-Field Optical Mapping of Quantum Hall Edge States. *Phys. Rev. Lett.*, 107:256803, Dec 2011.

[156] Keji Lai, Worasom Kundhikanjana, Michael A. Kelly, Zhi-Xun Shen, Javad Shabani, and Mansour Shayegan. Imaging of Coulomb-Driven Quantum Hall Edge States. *Phys. Rev. Lett.*, 107:176809, Oct 2011.

[157] Katja C. Nowack, Eric M. Spanton, Matthias Baenninger, Markus König, John R. Kirtley, Beena Kalisky, C. Ames, Philipp Leubner, Christoph Brüne, Hartmut Buhmann, Laurens W. Molenkamp, David Goldhaber-Gordon, and Kathryn A. Moler. Imaging currents in HgTe quantum wells in the quantum spin Hall regime. *Nature Materials*, 12:787 EP –, 06 2013.

[158] Raffaele Resta. Electrical polarization and orbital magnetization: the modern theories. *Journal of Physics: Condensed Matter*, 22(12):123201, 2010.

[159] T. Thonhauser. Theory of orbital magnetization in solids. *International Journal of Modern Physics B*, 25(11):1429–1458, 2011.